NTNU – Trondheim
Norwegian University of
Science and Technology

Photoluminescence Study of Enhanced Light Emission from HgCdTe Thin Films due to a Surface Pattern

Espen Tunhøvd Haugan

Nanotechnology
Submission date: June 2015
Supervisor: Johannes Skaar, IET
Co-supervisor: Randi Haakenaasen, Forsvarets forskningsinstitutt (FFI)

Norwegian University of Science and Technology
Department of Electronics and Telecommunications

Preface

This thesis constitutes the 10th and last semester of my master degree study in nanotechnology at the Norwegian University of Science and Technology (NTNU). The study itself is a continuation of my project assignment [1] "Enhanced light emission from HgCdTe thin films with a surface pattern", which was performed in the autumn of 2014.

The work has been carried out at the Norwegian Defence Research Establishment (FFI) under the supervision of Prof. Randi Haakenaasen (FFI) and Prof. Johannes Skaar (NTNU).

I would like to thank everybody at FFI and University Graduate Center Kjeller (UNIK) who have helped me in this project assignment. Especially, Randi Haakenaasen, who has allowed me to perform this work at FFI, read through the report, guided me throughout the whole semester and discussed the work and results with me for many hours. Johannes Skaar also deserves a big thanks for being my NTNU supervisor, reading through the report and for discussions regarding different aspects of the work.

In addition, I would also like to thank Aasmund S. Sudbø at UNIK for fruitful discussions on the FDTD simulations, Espen Selvig for growing the samples by MBE, and for hours of discussions regarding the experimental results, Laila Trosdahl-Iversen for helping me with the photolithography and etching, and Torgeir Lorentzen for obtaining the AFM-images.

Kjeller, June 3rd 2015

Espen Tunhøvd Haugan

Abstract

HgCdTe thin film samples with a CdTe passivation layer have been grown by molecular beam epitaxy, and photolithography has been used to etch a triangular pattern of holes into the passivation layer. The enhancement in light emission from the samples due to their surface pattern has been measured by means of photoluminescence spectroscopy (PL), giving values ranging from 31 % to 163 %.

PL-measurements and simulations with both the transfer matrix method and the 3D finite-difference time-domain (FDTD)-method have been used to investigate how the enhancement in light emission due to the surface pattern and the light extraction efficiency varies due to the sample parameters.

Different grating periods of the surface pattern, with a lattice constant to the wavelength ratio from 0.8-1.6, have been tested, where the enhancement in light emission for a grating period of 0.8-1.4 seems to be sample dependent, but fairly constant, while a larger grating period gives a lower enhancement.

It has also been studied how the light extraction efficiency of the samples depends on the depth of the holes, showing that for an emitted vacuum wavelength of about 4.6 μm, the holes should be at least 600 nm deep and etched all the way through the passivation layer of the structure.

PL-measurements also showed that there was no difference in the enhancement in light emission when the sample holder was tilted 21°, so that the detector covered a solid angle centered around 21° relative to the surface normal of the sample.

As both samples with and without a backside distributed Bragg reflector (DBR) were studied, the PL-measurements and simulations showed the effects of adding a DBR to the structure. It appears to increase the enhancement in light emission, but samples with a DBR also emit a broader range of wavelengths. When it comes to the absolute intensity emitted, the experiments and simulations give ambiguous results regarding the effect of the

DBR.

Sammendrag

HgCdTe-tynnfilmprøver med et passiveringslag av CdTe har blitt grodd ved hjelp av molekylstråleepitaksi, og fotolitografi har blitt brukt til å etse et triangulært hullmønster i passiveringslaget. Økningen i lysemisjonen fra HgCdTe-tynnfilmene på grunn av overflatemønsteret har blitt målt til 31 % - 163 % ved hjelp av fotoluminesens spektroskopi (PL).

PL-målinger og simuleringer med både transfermatrisemetoden og 3D finite-difference time-domain (FDTD)-metoden har blitt brukt til å undersøke hvordan økningen i lysemisjonen varierer som følge av forskjellige prøveparametere, der både den absolutte økningen i lysemisjon, og forskjellen i lysemisjon mellom en mønstret og umønstret overflate har blitt undersøkt.

Ulike gitterperioder har blitt testet for overflatemønsteret, der forholdet mellom gitterkonstanten og bølgelengden har variert mellom 0.8 og 1.6. Økningen i lysemisjon ser ut til å være avhengig av den individuelle prøven, men den er relativt konstant, når forholdet mellom de to parameterne er mellom 0.8 og 1.4, mens for større verdier av forholdet minker lysemisjonsøkningen.

Det har også blitt undersøkt hvordan andelen av det genererte lyset som emitteres ut av prøven avhenger av dybden på hullene i overflatemønsteret. PL-målingene og simuleringene tilsier at for en emittert bølgelengde på 4.6 μm bør hullene være minst 600 nm dype, og etset gjennom hele strukturens passiveringslag.

PL-målinger viste også at økningen i lysemisjon ikke endret seg hvis to forskjellige prøveholdere ble brukt, der den ene var tiltet 21 grader i forhold til den andre.

Da både prøver med og uten et Bragg-speil (DBR) har blitt undersøkt, har effekter av å tilføre en DBR til strukturen blitt funnet ved hjelp av både PL-målinger og simuleringer. Dette ser ut til å gi en større økning i lysemisjonen enn for strukturer uten en DBR, men emitterer samtidig et bredere spekter av bølgelengder. Når det gjelder den absolutt emitterte intensiteten gir PL-målingene og simuleringsresultatene tvetydige resultater.

Contents

Acronyms

AFM Atomic Force Microscope.

DBR Distributed Bragg Reflector.

FDTD Finite-Difference Time-Domain.

LED Light-Emitting Diode.

LEE Light Extraction Efficiency.

MBE Molecular Beam Epitaxy.

MCT $Hg_{1-x}Cd_xTe$.

MQW Multiple Quantum Wells.

PL Photoluminescence (spectroscopy).

Chapter 1

Introduction

Light-emitting diodes (LEDs) in the infrared (IR) domain have been of growing interest during the last decades [2–4]. This is mainly because the IR domain has two unique features, which is several atmospheric transmission windows, which can be used for free space communication, and molecular absorption lines, which can for instance be exploited in trace gas monitoring [5]. To create LEDs with emission in the mid wavelength (3-5 μm) and long wavelength (8-13 μm) IR regions, narrow band gap semiconductors are used. These materials often suffer from non-radiative loss mechanisms, such as Auger recombination [3], and the devices therefore have to be operated at a low temperature.

$Hg_{1-x}Cd_xTe$ (MCT) is a semiconductor with a narrow direct band gap, and the band gap can be tuned by changing the value of x, which is the Cd mole fraction. At 77 K, the direct band gap can be tuned from 0 eV (x=0) for HgTe to 1.6 eV (x=1) for CdTe [2], covering the entire IR range of the electromagnetic spectrum. Furthermore, over the whole range of x-values the lattice parameter only changes by 0.3 %, which facilitates growing heterostructures [6]. Today, MCT is the material of choice for IR detectors, but the described properties also make MCT a good choice of material for IR LEDs.

However, MCT LEDs will suffer from the same problem as other semiconductors with a high refractive index ($\approx$ 3.4 for MCT), which is that a large fraction of the generated light will be index guided, or totally internally reflected. Because of this, only about 2 % of the generated light in MCT will be transmitted out of a planar surface of the structure to the surrounding

air, leaving the light extraction efficiency (LEE), which is the fraction of generated light being extracted out of the structure, low.

As this is a common problem for materials typically used in LEDs, solutions that partly cope with this problem are being used. One solution has been to cover the LED surface with a dome of lower refractive index. This dome is then shaped in order to make the emitted radiation propagate normal to its surface, which will increase the LEE [7]. Another method is to introduce a random roughness in the LED surface, in order to obtain an angular randomisation of the incident waves on the surface [8, 9]. In combination with a reflective backside, the photons will then get multiple chances of being transmitted, and incident waves outside the escape cone, constituted by the incidence angles less than the critical angle for total internal reflection, will be reflected back and forth inside the LED until they either fall within the escape cone or are reabsorbed. A similar method, and the one investigated in this study, is to create a regular pattern on the surface. The surface pattern, with a period on the same order of magnitude as the wavelength of the incident light, can in this case be considered a photonic crystal slab, but it mainly serves as a diffraction grating. While light with a large tangential component of the wave vector $\boldsymbol{k}$ along the interface between the LED and the surrounding medium will suffer from total internal reflection, the grating can scatter the light and change the tangential component of $\boldsymbol{k}$ by a grating reciprocal lattice vector [10,11], and thereby scatter the light from outside to inside the escape cone. This principle is illustrated in Figure 1.1. The effect of a triangular surface pattern has been studied for other LED structures [10, 12–14], showing 30-170 % enhancement in the light emission depending on the material, grating used, and whether the sample had a reflective backside. A similar study was also performed for MCT without a reflective backside at the Norwegian Defence Research Establishment (FFI) [2], and in this study, an enhancement of 26-35 % was achieved.

In my project assignment [1], simulations of the MCT structure and its surface pattern were carried out in order to achieve a larger enhancement in light emission than 26-35 %. The simulations had two parts; adding a distributed Bragg reflector (DBR) to create a reflective backside and optimising the surface pattern. For this, two methods were used: transfer matrices and 2D finite-difference time-domain (FDTD), and the results were used to design new MCT samples. The goal of this study is to grow the new structures, process the surface patterns, and measure the enhancement in light emission with photoluminescence spectroscopy (PL). In addition, 3D FDTD simula-

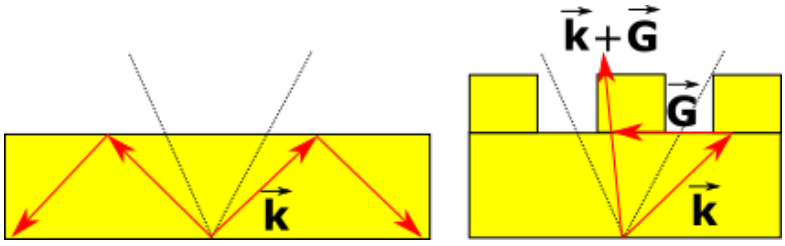

Figure 1.1: The structure to the left suffers from total internal reflection, while the one to the right illustrates the effect of the regular surface pattern. The tangential component of $\boldsymbol{k}$ can be changed by an integer number of the grating reciprocal lattice vector $\boldsymbol{G}$, which will scatter the light from outside to inside the escape cone. The escape cone is shown with dotted lines.

tions will be performed for each sample to find a better simulated qualitative result for the enhancement, as the 2D simulations used previously had some limitations [1]. The combination of PL-measurements and simulations, where also new transfer matrix method simulations are included, will also be used to discuss how the LEE depends on the different parameters of the structure and surface pattern. As the goal of this work was to investigate the principle of enhancement in light emission, a diode will not be processed. The active layer will rather be a thin film where the light is generated by photoluminescence, as this makes the experimental setup easier. The results can then easily be transferred from a thin-film structure to an LED.

This report is organised as follows: In Chapter 2, the necessary theory about photonic crystals, Bragg mirrors, MCT, and recombination mechanisms is presented. Chapter 3 gives an overview of the experimental methods together with the experimental setup, while Chapter 4 contains an explanation of the simulation methods and how they were used. Chapter 5 will present the results of the experiments described in Chapter 3, before discussing the results together with a general discussion about how the enhancement in light emission depends on the different sample parameters. In Chapter 6, conclusions are drawn, and further work is suggested.

Chapter 2

Theory

This chapter will first present general theory about photonic crystals in relation to this study, before distributed Bragg reflectors are explained. Then, the relevant aspects about MCT and recombination mechanisms for this study are discussed.

2.1 Photonic crystals

A photonic crystal can be regarded as an optical analogy to the crystals used in solid state physics. In solid state physics, the periodic electronic potential of the crystals is used to explain how electrons of a certain energy can propagate without being scattered in a conducting crystal. For the photonic crystals, the atoms or molecules are replaced by a periodic arrangement of materials with different dielectric constants, and instead of electrons, it is studied how photons of certain frequencies are allowed to propagate in the crystal while other frequencies are not able to propagate in some or all directions in the crystal. The photonic crystal is considered either as one, two or three dimensional, depending on in how many dimensions it is periodic. This is illustrated in Figure 2.1.

In this theoretical section, the materials of the photonic crystal are considered linear, lossless dielectric materials. Although this is a simplification from the physical situation, many interesting properties of the photonic crystals can still be described quite accurately.

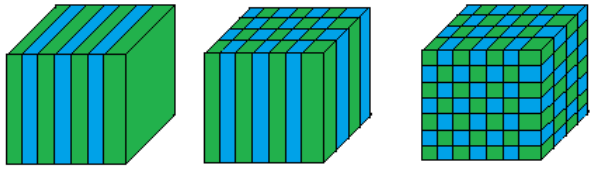

Figure 2.1: Illustration of photonic crystals of different dimensions. The different colours show materials with different dielectric constant. The crystal to the left is considered a one-dimensional photonic crystal, the one in the middle a two-dimensional, while the photonic crystal to the right is three-dimensional.

For the upcoming two subsections, "Light propagation in a photonic crystal" and "Band structures in a photonic crystal", the book "Photonic crystals: Molding the flow of Light" 2nd edition by Joannopoulos et.al [15] has been used, and the theory given here is a dense summary of the important parts described that are necessary for this study.

2.1.1 Light propagation in a photonic crystal

The starting point for investigating the propagation of electromagnetic waves in a photonic crystal is Maxwell's equations, given for a macroscopic medium as:

$$\begin{aligned} \nabla \cdot \boldsymbol{B} &= 0 \\ \nabla \cdot \boldsymbol{D} &= 0 \\ \nabla \times \boldsymbol{E} &= -\frac{\partial \boldsymbol{B}}{\partial t} \\ \nabla \times \boldsymbol{H} &= \frac{\partial \boldsymbol{D}}{\partial t} \end{aligned} \tag{2.1}$$

Here, it is assumed to be no free charges or currents in the material. In these equations, $\boldsymbol{E}$ is the electric field, $\boldsymbol{D}$ is the displacement field, $\boldsymbol{B}$ is the magnetic flux density, while $\boldsymbol{H}$ is the magnetic field strength.

By assuming that the field strengths are small, the properties can be treated in the linear regime, which relates $\boldsymbol{D}$ and $\boldsymbol{E}$ by $\boldsymbol{D}(\boldsymbol{r}) = \epsilon_0 \epsilon_\mathrm{r}(\boldsymbol{r}) \boldsymbol{E}(\boldsymbol{r})$. Here, ϵ_0 is the vacuum permittivity ($8.85 \cdot 10^{-12}$ F/m) and ϵ_r is the relative permittivity of the material at position $\boldsymbol{r}$. For the simplest theoretical approach for photonic crystals, the materials are seen as transparent, and the permittivity is then purely real and positive. The frequency dependence of the permit-

tivity is also ignored. The magnetic properties can be related in a similar fashion, by $\boldsymbol{B}(\boldsymbol{r}) = \mu_0\mu_\mathrm{r}(\boldsymbol{r})\boldsymbol{H}(\boldsymbol{r})$, where μ_0 and μ_r are the vacuum magnetic permeability ($4\pi \cdot 10^{-7}$ Vs/Am) and the relative permeability. As the linear and lossless dielectric materials are mostly non-magnetic, μ_r is set to 1. With these definitions, and time dependence also included, the Maxwell's equations can be written as:

$$\begin{aligned} \nabla \cdot \boldsymbol{H}(\boldsymbol{r},t) &= 0 \\ \nabla \cdot \Big(\epsilon_\mathrm{r}(\boldsymbol{r})\boldsymbol{E}(\boldsymbol{r},t)\Big) &= 0 \\ \nabla \times \boldsymbol{E}(\boldsymbol{r},t) &= -\mu_0 \frac{\partial \boldsymbol{H}(\boldsymbol{r},t)}{\partial t} \\ \nabla \times \boldsymbol{H}(\boldsymbol{r},t) &= \epsilon_0\epsilon_\mathrm{r}(\boldsymbol{r}) \frac{\partial \boldsymbol{E}(\boldsymbol{r},t)}{\partial t} \end{aligned} \tag{2.2}$$

Because the Maxwell equations are linear, it can be useful to further expand the fields into a set of harmonic modes, where the time and spatial dependence are separated. Not only is the separation of variables an advantage when solving the equations, but any solution can then also be represented by a combination of the harmonic modes. The magnetic field strength and electric field is then written as:

$$\begin{aligned} \boldsymbol{H}(\boldsymbol{r},t) &= \boldsymbol{H}(\boldsymbol{r})e^{-i\omega t} \\ \boldsymbol{E}(\boldsymbol{r},t) &= \boldsymbol{E}(\boldsymbol{r})e^{-i\omega t} \end{aligned} \tag{2.3}$$

This representation of the fields can be used to rewrite the curl equations from (2.2):

$$\begin{aligned} \nabla \times \boldsymbol{E}(\boldsymbol{r}) &= i\omega\mu_0 \boldsymbol{H}(\boldsymbol{r}) \\ \nabla \times \boldsymbol{H}(\boldsymbol{r}) &= -i\omega\epsilon_0\epsilon_\mathrm{r}(\boldsymbol{r}) \boldsymbol{E}(\boldsymbol{r}) \end{aligned} \tag{2.4}$$

By combining the two curl equations of (2.4) and perform simple manipulations, while using that $c = \frac{1}{\sqrt{\epsilon_0\mu_0}}$, where c is the speed of light in vacuum, one can obtain what is known as the master equation:

$$\nabla \times \left(\frac{1}{\epsilon_\mathrm{r}(\boldsymbol{r})} \nabla \times \boldsymbol{H}(\boldsymbol{r})\right) = (\frac{\omega}{c})^2 \boldsymbol{H}(\boldsymbol{r}) \tag{2.5}$$

For a given $\epsilon(\boldsymbol{r})$, it is then possible to obtain the modes of $\boldsymbol{H}(\boldsymbol{r})$ and their corresponding frequencies (ω). Using again (2.4), the electric field modes of the system can also easily be found.

2.1.2 Band gaps in a photonic crystal

The most important feature of the photonic crystal is its band structure, which determines in which directions the light can and can not propagate for given frequencies. The background for this band structure will be explained in this section, and also a few words on the band diagram will be given.

Due to the periodicity of the photonic crystals, and its discrete translational symmetry, the modes described in the previous subsection can be written as Bloch waves:

$$\boldsymbol{H_k}(\boldsymbol{r}) = \boldsymbol{u_k}(\boldsymbol{r})e^{i\boldsymbol{kr}} \tag{2.6}$$

In this representation $\boldsymbol{k}$ is the Bloch wave vector of the mode, which will be further explained soon, and $\boldsymbol{u_k}(\boldsymbol{r})$ is a periodic function with the same periodicty as the photonic crystal itself. If the lattice of the photonic crystal has a lattice vector $\boldsymbol{R} = l\boldsymbol{a_1} + m\boldsymbol{a_2} + n\boldsymbol{a_3}$, where $(\boldsymbol{a_1}, \boldsymbol{a_2}, \boldsymbol{a_3})$ are the primitive lattice vectors of the unit cell of the photonic crystal, and l, m and n are integers, $\boldsymbol{u_k}(\boldsymbol{r})$ is then equal to $\boldsymbol{u_k}(\boldsymbol{r} + \boldsymbol{R})$.

The three primitive lattice vectors $(\boldsymbol{a_1}, \boldsymbol{a_2}, \boldsymbol{a_3})$ give rise to three primitive reciprocal lattice vectors $(\boldsymbol{b_1}, \boldsymbol{b_2}, \boldsymbol{b_3})$. The details about this and the reciprocal space will not be explained here, and for further details, it is referred to the appendix of the book "Photonic Crystals" 2nd edition by Joannopoulos et.al [15]. However, it is still of importance to know that the primitive reciprocal lattice vectors are designed so that $\boldsymbol{a_i} \cdot \boldsymbol{b_j} = 2\pi\delta_{ij}$, where δ_{ij} is equal to 1 if $i = j$ and 0 else. From these reciprocal vectors, the earlier mentioned Bloch wave vector is created, so that $\boldsymbol{k} = k_1\boldsymbol{b_1} + k_2\boldsymbol{b_2} + k_3\boldsymbol{b_3}$. What can now be seen is that by using (2.6), if the Bloch wave vector is changed by an integer number of a reciprocal lattice vector, the new Bloch state will remain unchanged, and is not different from the original Bloch state from a physical point of view. This makes it possible to only consider a few Bloch wave vectors when analyzing the behavior of the photonic crystal. If k_i is the i-component of the Bloch wave vector, then it is sufficient to investigate the interval $\frac{-\pi}{a_i} < k_i < \frac{\pi}{a_i}$, where a_i is the lattice constant in the direction of the k_i-component. This region then defines what is known as the first Brilloiun zone.

By using the representation of $\boldsymbol{H_k}(\boldsymbol{r})$ given in (2.6) in the master equation, the periodic function $\boldsymbol{u_k}$ can be determined, and from this the mode profiles

are found. Due to the periodicity of the crystal, (2.5) can be regarded as restricted to a single unit cell. As the master equation then is restricted to a finite volume, this will leave us with a discrete spectrum of possible frequencies ω for each value of $\boldsymbol{k}$. From this, it is then possible to find the full band structure of the photonic crystal. If we label a given band n, then ω_n will vary continously as a function of $\boldsymbol{k}$. By plotting this, a band structure for band n can be seen. If the plots for all values of n is included in the same plot, the full band diagram is obtained. An example of a band structure with the three lowest bands is shown in Figure 2.2, where the waves are propagating in the direction of periodicity. This band structure is from a 1D photonic crystal, which also can be seen as a multilayer film. Details about this particular plot is given in the figure caption.

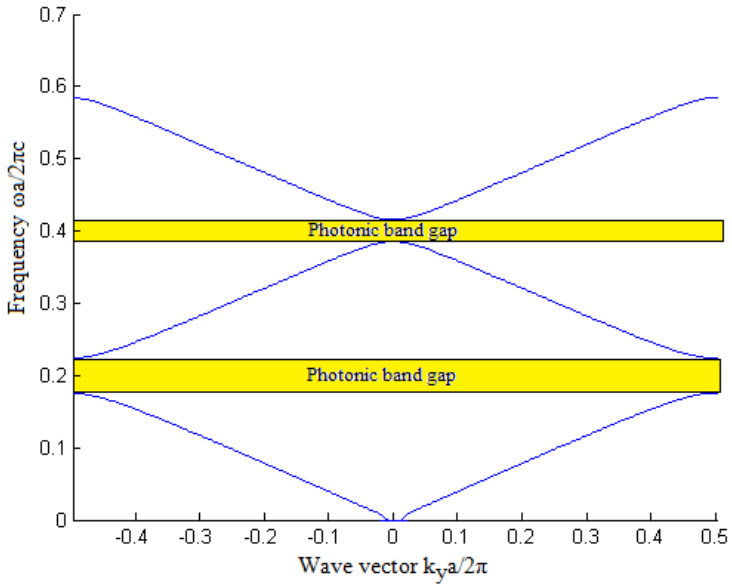

Figure 2.2: Band structure of a 1D photonic crystal. The x-axis shows wave vector component in the direction of periodicity, while the y-axis shows the frequency. Both the x and y-axis are normalized. This band structure shows the three lowest bands in the first Brillouin zone. This plot is obtained from a periodic multilayer film with a period a, where the thickness of the two alternating films are $\frac{a}{2}$ in the direction of periodicity. The refractive indices of the two films are 1 and 1.5. The details around how the bands are obtained is given in an exercise in the course "Photonic Crystals" at the University of Oslo [16].

From the example of a band structure given in Figure 2.2, the optical proper-

ties of the photonic crystal can be investigated. The bands show the allowed states in the crystal, and give for which frequencies light can propagate in the direction of periodicity (y-direction). More importantly, it also shows for which frequencies light can not propagate, when propagating in this direction. When this is limited to some values of k_y it is called an incomplete band gap. However, as is shown in Figure 2.2, for a frequency about 0.2 $\frac{\omega a}{2\pi c}$, there are no allowed valus of k_y where the light can propagate. This is known as a complete band gap, as light within this band gap can not propagate in the structure, independent of its value of k_y. It should be mentioned that Figure 2.2 only shows the band structure for propagation in one direction, and the complete band gap would in this case disappear if the waves were allowed to propagate in other directions. For a complete band gap in all directions, a 3D photonic crystal is necessary.

2.1.3 Photonic crystal slabs

In this thesis, what is known as a photonic crystal slab is being investigated. These are similar to 2D photonic crystals, but the important difference is that where the 2D photonic crystal is extended infinitely in the direction where it is not periodic, the 2D photonic crystal slab has a finite thickness. This is shown in Figure 2.3. Although these two structures are physically different, the photonic crystal slab still displays many of the same properties as the photonic crystal [17]. The reason why a photonic crystal slab is often fabricated instead of a 2D photonic crystal is related to easiness and low cost of fabrication. Stricly speaking, a true 2D photonic crystal requires an infinite thickness, which would be impossible to fabricate.

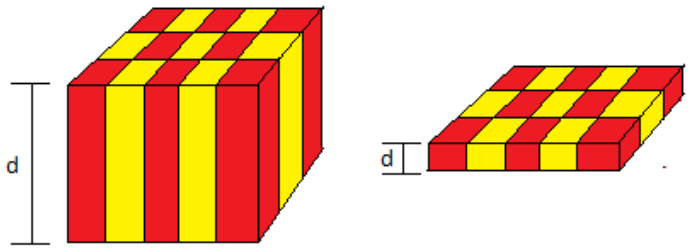

Figure 2.3: Illustration of a 2D photonic crystal (left) and a photonic crystal slab (right). The thickness, d, is infinite for a 2D photonic crystal while finite for a photonic crystal slab.

When considering photonic crystal slabs, the calculations for a 2D photonic crystal with the similar periodicity and materials can not be applied directly. The band structure calculations are only valid if the wave vector is in the plane of the periodicity, and when this is not the case, the surrounding medium will have to be introduced somehow. The general effect is that the surrounding medium will introduce a continuum of possible states, and thereby destroy the potential band gaps present [17]. This is shown in Figure 2.4, where the band structure from both the photonic crystal and the photonic crystal slab are shown. It can be seen that there are still incomplete band gaps in the region with discrete states, but a potential complete band gap will not be possible due to the introduced continuum of states.

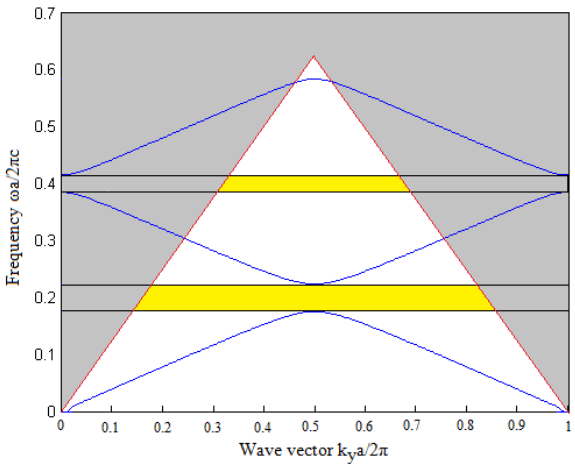

Figure 2.4: Illustration of the difference in the band structure between a photonic crystal and a photonic crystal slab. The band structure itself is just an illustration, but shows that with a photonic crystal slab, a light cone is introduced, where the grey areas are extended modes. The complete band gaps are then destroyed, and if the symmetry of the photonic crystal in the periodic direction(s) is destroyed, the k-values are not conserved, and localized modes in the band gap can couple to extended modes.

2.2 Diffraction gratings

In this study, a structure similar to the 2D photonic crystal slab shown in Figure 2.3 is used on top of an active material generating photons. The goal is to use this slab to extract some of the light which without the slab would have suffered from total internal reflection. From Snell's law, incident light

with a larger incidence angle than the critical angle will be totally reflected, where the critical angle is given as:

$$\theta_c = \sin^{-1}\left(\frac{n_2}{n_1}\right) \tag{2.7}$$

Here n_1 is the refractive index of the material where the photon is incident from, and n_2 is the refractive index of the surrounding material. For MCT ($x = 0.29$), this critical angle is 17.1°.

2.2.1 Effect of the diffraction grating

For a 2D photonic crystal slab, Pudis et.al [14] describe different ways the photonic crystal slab can enhance light emission. For a structure with a grating period of the same order as the wavelength of the incident light, the band gap of the photonic crystal can be used to increase the light emission. As the light enters the photonic crystal slab, it will either couple to the guided modes or to modes than can radiate out of the slab. If the frequency and wave vector of the trapped light within the structure is matched to the band gap between the guided modes, the trapped light will couple to free space modes (grey area of Figure 2.4) and radiate out of the sample [18]. However, as there is no complete photonic band gap in a 2D photonic crystal when the light is not propagating in the plane of the periodicity [15], this effect is difficult to realise in practice [19].

An easier approach is to use the slab as a diffraction grating, where the regular pattern scatters light from outside to inside the escape cone [2]. The critical angle from (2.7) arises from the fact that the vector component of $\boldsymbol{k}$ parallel to the interface has to be continous across the interface. When the layer where the photons are generated has a larger refractive index than the surrounding layer, total internal reflection appears when the length of the wave vector component in the medium of the originating photons parallel to the interface is larger than the total length of the wave vector in the surrounding layer. The 2D grating can then prevent total internal reflection by changing this parallel component by a reciprocal lattice vector of the photonic crystal slab. From this, the angle of the diffraction order m, θ_m, for a given incidence angle θ_i for a 1D diffraction grating is given as:

$$\sin(\theta_m) = \sin(\theta_i) + \frac{m\lambda}{n\Lambda} \tag{2.8}$$

Here λ is the vacuum wavelength of the photons, n the refractive index of the material, and Λ is the grating period. For this one dimensional case, this is illustrated in Figure 2.5. In 2D, the equation is more complicated:

$$\begin{aligned} \sin(\theta_{m_x m_y})\cos(\theta_{m_x m_y}) &= \frac{m_x \lambda}{n\Lambda_x} \\ \sin(\theta_{m_x m_y})\sin(\theta_{m_x m_y}) &= \frac{m_y \lambda}{n\Lambda_y} \end{aligned} \tag{2.9}$$

The structure is assumed periodic in the x and y-direction.

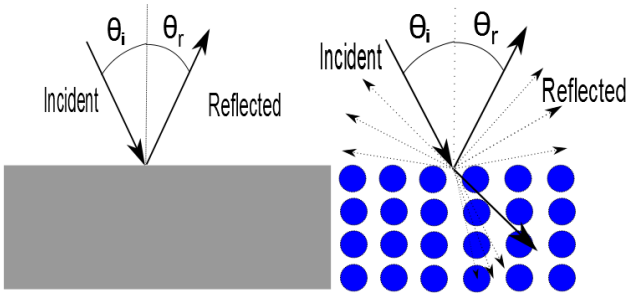

Figure 2.5: Left: Total internal reflection. Right: Scattering of the incident light due to the photonic crystal. The dotted lines represent different diffraction orders. In this figure, the light is incident from a medium with higher refractive index to a medium with a lower refractive index.

As can be seen from (2.8), when $\Lambda < \frac{\lambda}{n}$, only the zeroth order, which is the directly reflected/refracted wave, will have a real solution. Therefore, in order to have real solutions for higher diffraction orders, the period of the diffraction grating should be fabricated in order to have $\Lambda > \frac{\lambda}{n}$, as higher diffraction orders are then allowed. It can also be seen that large grating periods will lead to smaller angular spread between the different diffraction orders. For large incidence angles, this will lead to a small angular change for the lowest diffraction orders. In order to enhance light emission, the grating period should therefore not be fabricated too large.

To find the optimum grating period for enhancement in light emission, it is evident from (2.8) and (2.9) that Λ has to be optimised. The exact value is hard to find analytically, as it is challenging to find the relative scattered power of the different diffraction orders. To optimise the grating period, numerical computations are therefore usually used. It is also not possible to adapt optimised grating structures from other material systems, as the

relative scattered power in the different diffraction orders depends heavily on the material and the geometry of the structure itself.

2.3 Distributed Bragg reflector

To obtain high reflection, a mirror of a metallic film such as silver, aluminum or gold is often used [20]. However, for some structural designs, these mirrors cannot be used, for instance if it is desirable that some wavelenghts can transmit through the mirror, while others are reflected. An alternative is then to use dielectrics with almost no absorption, to create a so called Bragg mirror, also known as distributed Bragg reflector (DBR). The DBR has an alternating sequence of layers of two materials with different refractive index, as shown in Figure 2.6. The idea is then that the reflected waves from the various interfaces will experience constructive interference, which will result in a strong total reflection.

To simplify the explanation of how the DBR works, the principle is shown for waves with normal incidence in Figure 2.6. The reflection at each interface is given by the Fresnel equation, which for normal incidence and regardless of the waves' polarisation is:

$$r = \frac{n_1 - n_2}{n_1 + n_2} \tag{2.10}$$

Here n_1 is the refractive index of the medium where the wave is incident, while n_2 is the refractive index of the medium to which the wave is transmitted. The coefficient r is the ratio of the electric field amplitude of the reflected to the incident wave. As this equation shows, a large refractive index contrast is important in order to get a large reflection. At the same time, the waves will pick up a phase shift of π when reflecting from a medium with higher refractive index. This phase shift is important, as it will be helpful in designing the DBR to obtain constructive interference of the reflected waves.

Due to the mentioned phase shift, the most popular design for DBRs is the quarter-wave mirror [21]. By giving the layers a thickness of a quarter of the wavelength in the material, the difference in optical path length between reflections from subsequent interfaces is half of the wavelength, giving a phase shift of π. As only one of these two subsequent reflections will have a phase

shift of π due to (2.10), they will then be in phase. This will be the case for all of the reflections at the different interfaces, and the reflections will therefore interfere constructively, and a strong reflection is obtained. This principle is also shown in Figure 2.6.

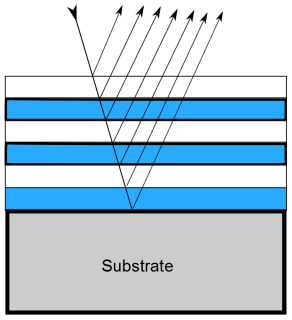

Figure 2.6: Figure to illustrate the principles of the DBR. The arrows symbolise waves that are reflected from different interfaces and interferes constructively. The normally incident waves are for illustrational purposes shown with a different incidence angle.

The total reflectivity of the DBR structure will be determined by the number of layers, and also by the refractive index contrast between the two different materials. In addition, it should also be mentioned that for waves with an incidence angle different from zero, the reflectivity will be lower, as the path difference between the different reflections in the structure will not be of half a wavelength. It will therefore only be possible to tune the structure perfectly for a single angle and λ, which has to be taken into considerations when designing DBRs in structures where the incidence angle of the light is changing.

2.4 $Hg_{1-x}Cd_xTe$

$Hg_{1-x}Cd_xTe$ (MCT) is a group II-VI semiconductor with a direct bandgap which can be tuned by changing the Cd mole fraction x. The lower limit is found when x is equal to zero, which is the semimetal HgTe with a direct bandgap of 0 eV, while the upper limit is 1.6 eV for CdTe, which is obtained when x is equal to 1 [2]. The bandgap also varies with temperature. One of the most commonly used empirical formulas for the bandgap energy E_g was suggested by Brice [22]:

$$E_g(x,T) = -0.313+1.787x+0.444x^2-1.237x^3+0.932x^4+T(0.667-1.714x+0.76x^2)\cdot 10^{-3} \tag{2.11}$$

Here E_g is the bandgap energy in eV, given with an uncertainty of ± 0.01 eV, and T is the temperature in Kelvin. Equation (2.11) is plotted against the x-value at 11 K in Figure 2.7.

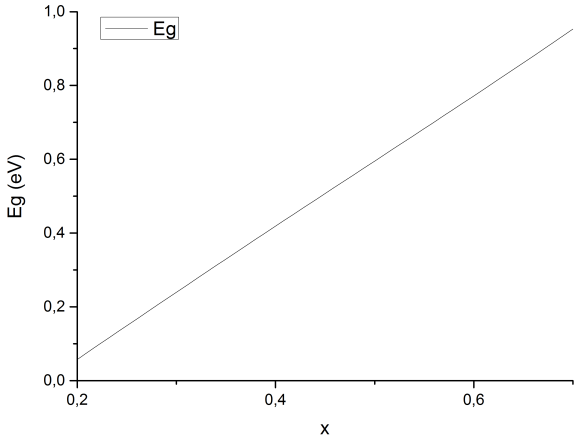

Figure 2.7: The bandgap energy, E_g plotted against the Cd mole fraction, x, at a temperature of 11 K, using (2.11)

The electric permittivity, and thereby the refractive index, are also functions of the Cd mole fraction and temperature. As the bandgap energy has a positive temperature coefficient, the refractive index has a negative temperature coefficient, and is therefore increasing when the temperature is lowered. Liu et.al proposed the following empirical expression for the wavelength-dependent refractive index:

$$n^2(\lambda,T) = A + \frac{B}{1-(\frac{C}{\lambda})^2} + D\lambda^2 \tag{2.12}$$

The composition and temperature are included in the fitting parameters, A, B, C and D, given as:

$$\begin{aligned} A =& 13.173 - 9.852x + 2.909x^2 + 10^{-3} \cdot (300 - T) \\ B =& 0.83 - 0.246x - 0.0961x^2 + 8 \cdot 10^{-4} \cdot (300 - T) \\ C =& 6.706 - 14.437x + 8.531x^2 + 7 \cdot 10^{-4} \cdot (300 - T) \\ D =& 1.953 \cdot 10^{-4} - 0.00128x + 1.853 \cdot 10^{-4}x^2 \end{aligned} \tag{2.13}$$

For the three different temperatures used in this study, (2.12) is shown in Figure 2.8 for a wavelength range of 1 to 15 μm. For all of the different temperatures, an x-value of 0.289 was used, which is typical for the samples in this study, when x is found by PL-measurements. By investigating the refractive index for the three different temperatures in Figure 2.8, it can be seen that the variations are small between the three choices of temperature.

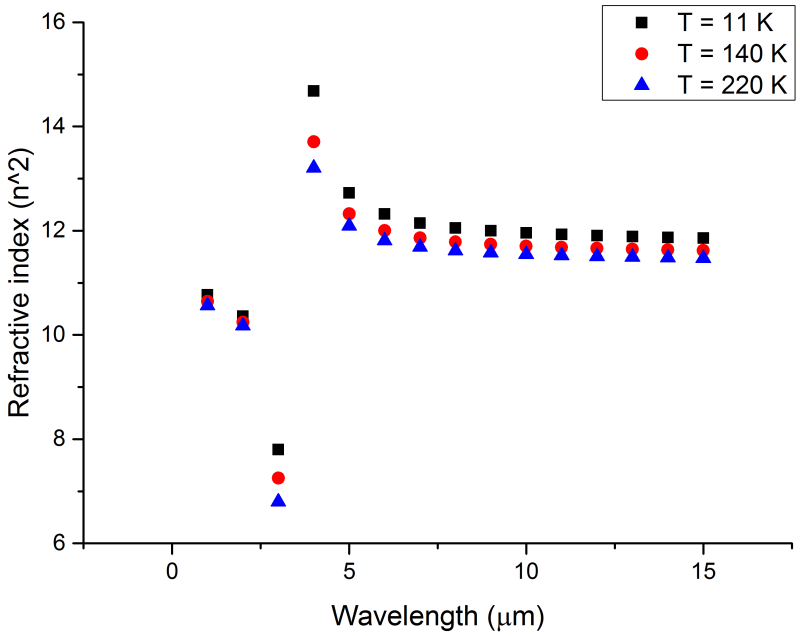

Figure 2.8: The square of the refractive index for three different temperatures when x is equal to 0.289. The parameters are explained in the text.

2.5 Recombination mechanisms

After the electron-hole pairs (EHP) are formed, they can recombine via different mechanisms. For some of the mechanisms, the released energy will be

carried away as a photon, and the mechanism is said to be radiative, while for other mechanisms, no photon is emitted, and the mechanism is non-radiative. Which recombination mechanism that will dominate depends on their lifetime, τ, which is the average time before an electron and a hole recombines by the given mechanism. The mechanism with the shortest lifetime will then be the one that dominates. However, a deeper theoretical study of these lifetimes is outside the scope of this study.

For a pure crystal, band-to-band-, exciton- and Auger recombination mechanisms are usually taking place. For less pure crystals, impurities will usually contribute to the recombination process, by introducing energy states in the band gap of the material. Recombination mechanisms where impurity states are contributing are collectively called Shockley-Read-Hall (SRH) recombination mechanisms, and can be both radiative and non-radiative, depending on the specific process.

2.5.1 Radiative and SRH recombinations

As the radiative recombinations lead to an emitted photon, they are the origin of luminescence. If the EHP is created by a photon, it is referred to as photoluminescence (PL). PL spectroscopy will be explained in a detailed manner in the next chapter, but in order to discuss the results from PL measurements, the different possible radiative recombination mechanisms have to be explained. These are shown in Figure 2.9

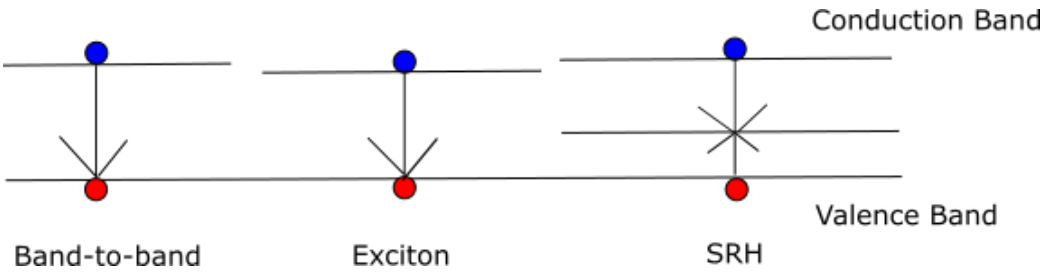

Figure 2.9: Simplified illustration of the three possible radiative recombination mechanisms described in the text. For the band to band transition, an electron in the conduction band fills a hole in the valence band, for an exciton, the same process happens, but the transition energy is smaller due to a Coulombic potential between the electron and the hole, and for the SRH, the electron and hole recombine through an energy state in the band gap.

Band-to-band transitions are dominant in MCT at higher temperatures [23]. A free electron in the conduction band and a free hole in the valence band recombine directly, and as no levels within the band gap are included, the transition energy is the highest possible within a bulk semiconductor.

A similar process is the exciton recombination. An exciton is an electrically neutral quasi-particle bound by the Coulombic attraction between the electron and a hole. When the electron and hole then recombine, the transition energy will be slightly lower than the band-to-band transition energy due to this Coulombic attraction. For MCT, the binding energy for an exciton is in the order of a few meV [24].

As impurity atoms or structural defects introduce energy states within the band gap, a recombination process can also include these states. This is known as trap-assisted recombination, or SRH recombination. The electron and hole then recombine through a two-step process, where the electron falls from the conduction band and into the impurity introduced state in the band gap, before the electron and the hole recombine. The transition energy will then depend on where within the band gap the impurity introduced energy state lies, as shown in Figure 2.9. This recombination mechanism can be both radiative and non-radiative, depending on its nature.

2.5.2 Non-radiative recombinations

Although the non-radiative recombinations cannot be detected by PL spectroscopy, they can still be used to explain the lack of PL. The most common non-radiative recombination mechanisms are the Auger recombinations, where two possible outcomes are shown in Figure 2.10.

Unlike the radiative recombinations, the Auger recombination is a three-particle process. The energy released when the electron-hole pair recombines is transferred to another electron or hole. For MCT, there are ten different phononless Auger processes [25], where Figure 2.10 shows the predominant ones. The lifetime of the Auger process generally decreases for an increasing temperature, making them more dominant at higher temperatues [25].

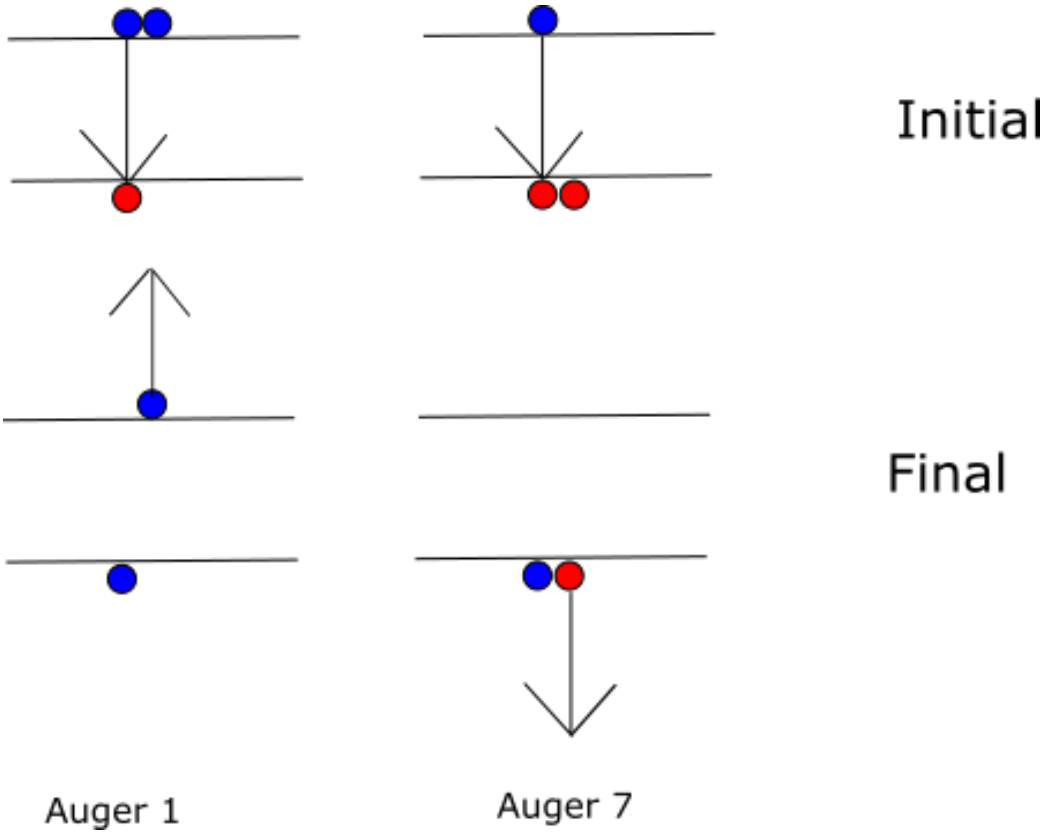

Figure 2.10: Simplified illustration of two possible Auger mechanisms. In Auger 1, the energy released from the recombination of the electron and the hole is transferred to an electron in the conduction band. For Auger 7, the released energy is transferred to an electron in the valence band with a lower energy than the recombined electron. This can also be seen as a process where the energy is transferred to the hole, as the figure illustrates. Auger 1 is most typical in semiconductors where electrons are the majority charge carriers, while Auger 7 is typical when holes are the majority charge carriers [6].

Chapter 3

Experimental

In this study, both simulations and experiments are performed. This chapter presents the physical experiments, while the procedures for the simulations can be found in the next chapter. Before the different experimental procedures are presented, an overview of the structure investigated is shown.

3.1 Overview of the structure

Before the details about the experimental procedures and simulation setups are described, a short overview of the structure is given. It is a structure with a surface pattern of approximately cylindrical holes etched into the CdTe passivation layer on about one half of the sample. The laser source used in the PL process has an intensity profile with a full width at half maximum (FWHM) of about 1 mm, and will be incident on the backside of the structure, through the substrate, and into the active MCT layer, where the electron-hole pairs are generated. The photons from radiative recombinations of these electron-hole pairs are measured by the spectrometer when exiting through the CdTe-layer. To easier follow the trajection of the laser source and emitted photons, a schematic drawing of the position of the different layers are shown in Figure 3.1. Here, CdZnTe is the substrate, the reflective layer is a distributed Bragg reflector (DBR) containing alternating CdTe and MCT ($x \approx 0.6$) layers, MCT ($x \approx 0.3$) is the active layer where photons are generated, and CdTe is a passivation layer where a surface pattern with a grating period, a, is etched in order to increase the LEE from the structure. Not all of the studied samples contain a DBR, and the laser beam then propagates directly from the substrate into the active layer. The passivation

Figure 3.1: Illustration of a cross section of the structure used in the PL spectroscopy experiments. The thickness and width of the different layers are not to scale.

layer is added because CdTe, unlike MCT, does not get damaged by etching. Addtionally, it should be mentioned that using MBE to grow the samples gives in general layers of high purity, and abrupt interfaces [6]. This leads to high quality heterostructure samples. The samples being studied are denoted PCC793-3, PCC793-4, PCC794-1, PCC794-3, PCC794-4 and PCC752-3. If the first three digits of the name are equal, the samples come from the same MBE-grow layer, but the structure has been sawed into several pieces, which have been processed differently. PCC794 contains a DBR, while PCC793 and PCC752 do not.

PCC752-3 differs from what is seen in Figure 3.1. There is no DBR, and in addition, the active thin film layer is substituted with 4 quantum wells, and there is an additional absorption layer between the multiple quantum wells (MQW) and the passivation layer. The PL-light will be emitted from the MQWs, and the absorption layer is designed to absorb most of the laser light to prevent it from being reflected at the surface and interact multiple times with the MQWs. A schematic drawing of this structure is shown in Figure 3.2.

The reason for patterning only a part of the surface area is that the laser can be scanned across the sample, and the enhancement in light emission can be found directly by comparing the LEE of the patterned and unpatterned area. This is the only way of having the same crystal quality and layer parameters for the two areas, ensuring that the enhancement will be exclusively due to the surface pattern.

In the simulations, the patterned and unpatterned parts of the structure were simulated individually. The reasons behind this are that the problem of a changing crystal quality for different samples is not faced when simulations

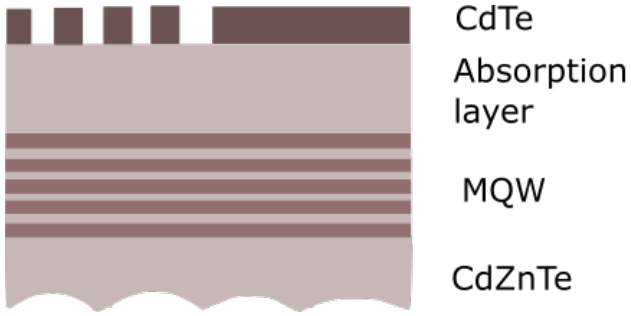

Figure 3.2: Cross section of the structure of PCC752-3. The thickness and width of the different layers are not to scale.

are done, and the size of the simulation domain. As the size of the samples is greatly reduced when the simulations are performed, the simulation domain is not large enough to separate the light transmitted from the patterned and unpatterned area, if only half of the sample is patterned. An enhancement in light emission can therefore not be accurately calculated, and in order to separate the two, individual simulations have to be performed.

An example of the regular surface pattern is shown in Figure 3.3. The pattern consist of a triangular lattice of air holes etched into the CdTe-layer. The shape of the holes is a mixture between cylindrical and conical due to the etching technique used.

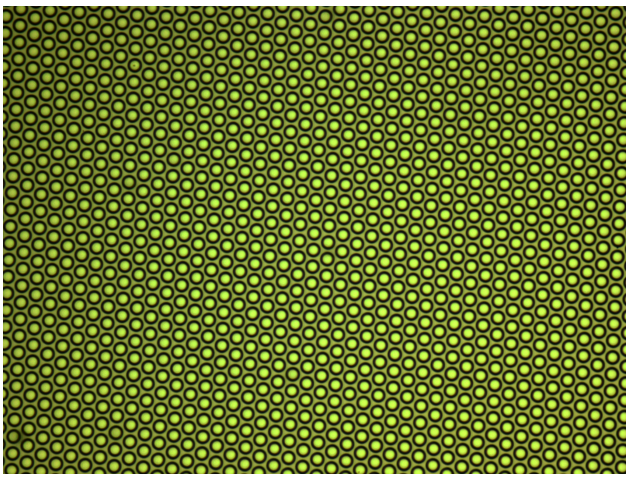

Figure 3.3: The surface pattern with a triangular lattice of air holes. The lattice parameter is 6 μm, while the fill factor (fraction of CdTe) is approximately 0.37.

3.2 Molecular beam epitaxy

3.2.1 General

Molecular beam epitaxy (MBE) is a growth technique suitable for growing materials epitaxially in ultra high vacuum. As the growth takes place in ultra high vacuum, there is an absence of carrier gas, which is typically present in vapor deposition methods. This makes it possible to obtain high-purity layers. A layout of the main chamber in the MBE system can be seen in Figure 3.4, where the main components are shown. The substrate is situated on a holder with a heating element to control the growth temperature. The constituent elements are situated in individual Knudsen effusion cells, which all have a shutter that can be opened or closed in a fraction of a second. When heating these effusion cells, the elements or molecules are evaporated, which makes them able to escape through the small orifice of the cell when the shutter is open. This creates a well-colimated beam, that will strike the substrate, where the elements will condense and the crystal is formed. The flux of elements from each source will then be given by the source temperature and whether the shutter is open or not. The short response time of the shutters of the effusion cells makes it possible to obtain abrupt interfaces between the different layers of the materials. While this process is taking place, the substrate is also rotating slowly, in order to obtain lateral homogeneity.

Due to the slow growth rate of the MBE, which is only about 50 nanometers per minute, the thickness of the sample can be controlled precisely. In addition, most MBE systems also contain a system for monitoring the growth process by the means of Reflection High Energy Electron Diffraction (RHEED). This technique is based on electron diffraction at the surface of the growing sample, and the detected diffraction pattern gives information about the surface layer of the sample during the growth.

3.2.2 Samples

The samples were grown in a Riber 32P MBE system. One Hg, Te and CdTe-source were used during the growth, as indicated in Figure 3.4, while the dopant source shown, however, was not used. As there is a certain drift in the effusion cell fluxes over time, a calibration sample was grown before the samples themselves, in order to adjust the growth parameters to the desired values, so that the wanted thicknesses and compositions of the layers

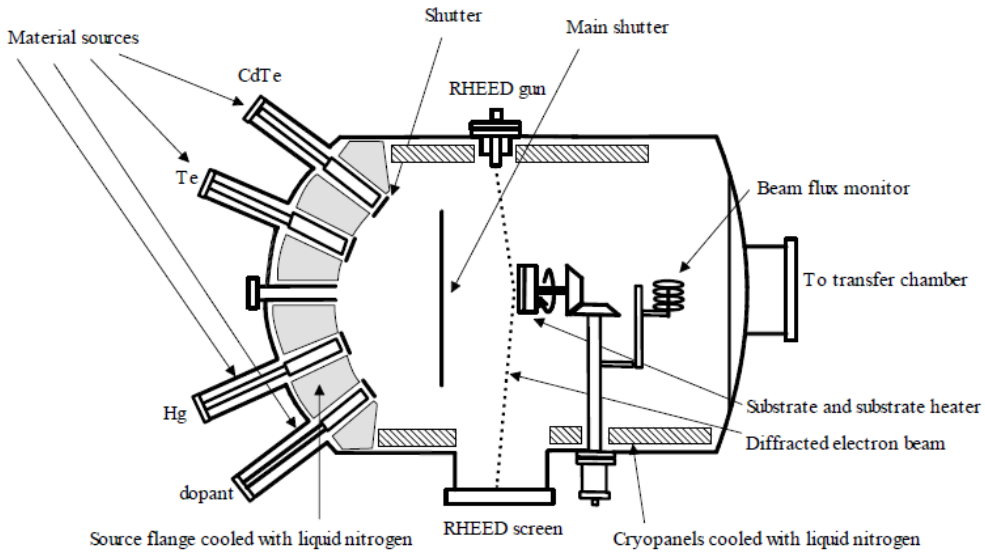

Figure 3.4: A sketch showing the main components of the growth chamber in the MBE system. The illustration is obtained from [26].

could be obtained. Unfortunately, the machine did not allow the shutter of the Hg-source to be closed, and the CdTe-layers are therefore grown in a Hg-flux. This will make the x-value of CdTe-layers slightly lower than 1.

All of the samples were grown on 15x15 mm^2 $Cd_{0.96}Zn_{0.04}Te$ substrates with the (211)B orientation, where the orientation is chosen to reduce the twin content in the epilayer [27]. The substrates also have a low in-plane lattice mismatch compared to MCT. During growth, the cell and substrate temperatures were adjusted in order to obtain the desired composition and thickness of the different layers.

3.3 Photolithography

Photolithography is a technique used in microfabrication to pattern the surface of a thin film, or if repeatedly performed together with etching and deposition of materials, to pattern also the bulk of a structure. The idea is to deposit a UV-light sensitive chemical on top of the sample, a so-called photoresist, and expose it to light through a patterned mask. When in a later step, known as developing, the photoresist is chemically treated, it is removed

depending on if it was exposed to light or not. The pattern of the mask is then transferred to the photoresist. Depending on what type of photoresist is used, the transferred pattern is either the same as the metal pattern of the mask (positive photoresist) or the opposite (negative photoresist). The patterned photoresist can then in further steps be used as a mask for for example deposition of new material, or for etching a pattern into the sample itself. These simple steps are shown in Figure 3.5.

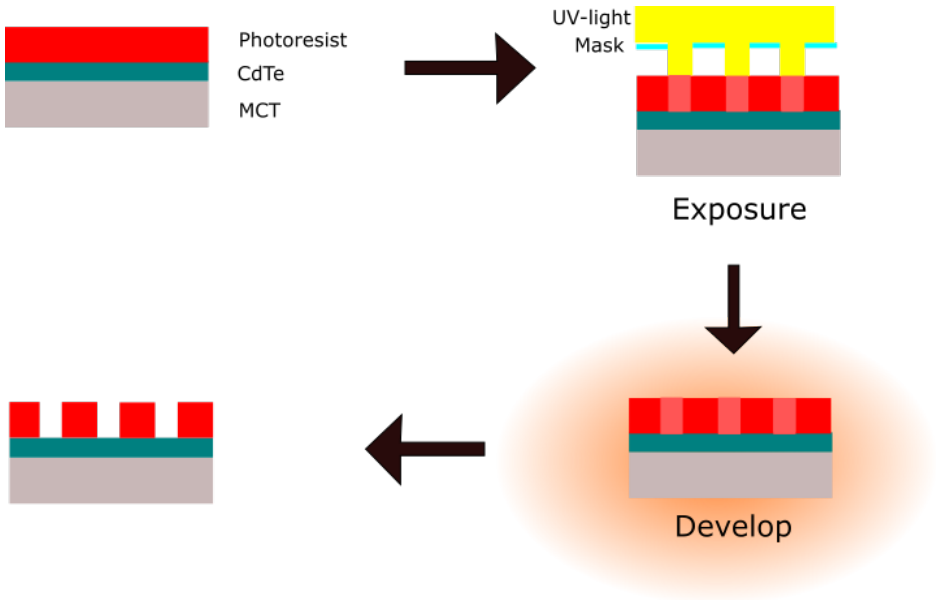

Figure 3.5: Illustration of a photolithography process, where the pattern of the mask is transferred to the photoresist. As the metal pattern of the mask and the developed photoresist is the same, the photoresist is positive.

Although Figure 3.5 gives an overview of a photolithography process, it still lacks important steps necessary to obtain a successfull result. The photolithography process is usually divided into ten steps, where all of them are of importance. The first 3 are sometimes considered as one step, but in this overview, they are presented individually. In the next subsection, the experimental procedure performed will be presented, and related to these ten steps.

3.3.1 The ten steps of photolithography

The general description of these ten steps is obtained from the book "Semiconductor Manufacture Technology" by Quirk and Serda [28].

Step 1: Clean

The purpose of the first step is to remove any type of contamination on the surface. The detailed procedure of what needs to be done in this step therefore depends on the history of the sample, but all samples should at least be cleaned with aceton and methanol to remove grease from its surface.

Step 2: Dehydration

To get better adhesion between the sample and the photoresist, a dehydration process is usually performed. This is done by heating the sample on a hotplate in order to remove any water present on the surface.

Step 3: Priming

If needed, a priming step is performed. This step has in general the same goal as the previous one, which is to increase the adhesion between the resist and the sample. These two steps are often performed simultaneously, or directly after each other. Unlike step 2, a chemical is deposited on the sample in this step, which will adhere both to the sample and the resist. A typical example is hexametyldisilizane (HDMS), and it is most commonly applied as vapor.

Step 4: Spin coat

Now that the sample has been prepared properly, the photoresist is deposited by spin coating. The amount of photoresist used depends on many factors, such as the size of the sample and the viscosity of the resist. When being spun, the centrifugal force will drag the resist away from the axis of rotation, and due to their lower viscosity, a large fraction of the solvent in the photoresist will be lost. The thickness of the resist will be relatively uniform across the sample, and the final thickness will depend on the spin rate and viscosity of the resist, where the dependence on the spin rate in revolutions per minute (RPM) in general be approximated as $\propto \frac{1}{\sqrt{\text{RPM}}}$.

Step 5: Soft bake

The next step is to decrease stress and tension in the resist by doing what is known as a soft bake process. The sample is then heated on a hotplate

for typically a few minutes. This process will also enhance the light absorption, increase the adhesion between the resist and the sample and reduce the fraction of solvent in the resist.

Step 6: Alignment and exposure

The sixth step is the first part of the pattern transfer from the mask to the sample. In this step, the sample with photoresist is aligned to the desired mask. The alignment can be done in three ways, which will introduce different features to the pattern transfer due to the exposure conditions. The mask and the sample can either be aligned and then put in contact mode, which is the one used in this work, or the exposure can happen with the mask and sample in proximity of each other, or so-called projection printing, where lenses are introduced to demagnify the mask pattern. There won't be a lot of emphasis on the different methods, but it is good to know that contact mode eliminates reflections of the UV-light from the back of the mask, which would had led to exposure of areas which should be covered by the mask.

After the alignment is successfully performed, the exposure has to be done. This is done with a single wavelength UV-light source, and the UV-light then catalyses a chemical reaction in the photoresist. This chemical reaction will for a positive resist make the exposed areas soluble, and the unexposed areas unsoluble, while a negative resist will have it the other way around.

Step 7: Post-exposure bake

After the exposure, a new baking step is performed. The sample is once again transported to the hot plate or a heating cabinet, where the heating process reduces the solvent content of the resist even further. This step is usually not mandatory for all photolithography processes, but necessary for resists that is exposed by deep UV wavelengths (typically 248, 193 or 157 nm). As for the other baking steps, this step will also increase the adhesion between the sample and the resist, and in addition reduce standing waves from the exposure.

Step 8: Develop

The pattern of the resist is now developed, by either removing the unexposed areas (negative resist) or exposed areas (positive resist) through a chemical

process. The samples are typically dipped in a diluted solution of the chemicals removing the desired areas of photoresist, and afterwards cleaned in water to remove any left-over developer. The water is then removed either by spinning or by blowing nitrogen (N_2) on the sample.

Step 9: Hard bake

The last baking step will also reduce the solvent content of the remaining resist and increase the adhesion. In this step, the leftover water and chemicals from the developing step are also removed.

Step 10: Develop inspect

The final step of the photolithography process is to inspect the sample and the pattern of the resist. This can be done in a light microscope, and if the process has been succesfull, the sample can be processed further. If the process was unsuccessfull, on the other hand, the resist is stripped off, and the process starts again from step 1.

Further treatment

The further treatment depends on what type of samples should be processed. One examples is shown in Figure 3.6, which illustrates how the patterned photoresist can be used as a mask for etching. Another possibility would be to use the patterned photoresist as a mask for depositing a new layer of material.

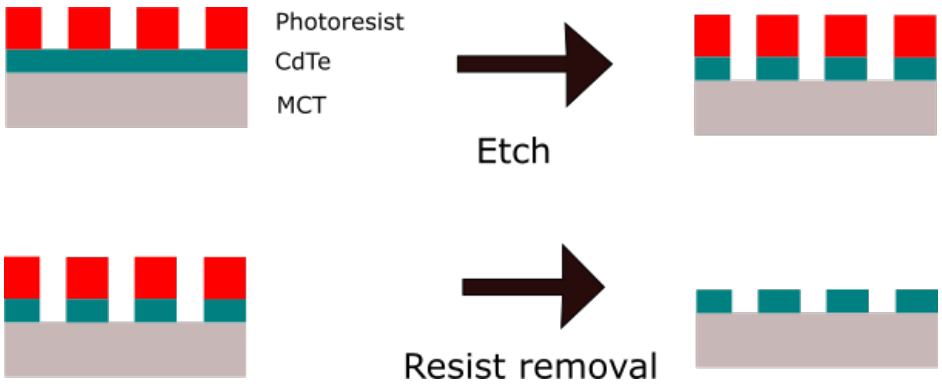

Figure 3.6: Illustration of the etching process, where the pattern is transferred from the photoresist to the sample surface.

3.3.2 Experimental procedure

In order to process the desired surface pattern for the different samples, different processing parameters were tried. The exposure and developing time were of high importance, and had to be fine tuned. If not, the surface pattern would either not be developed, and the bottoms of the holes would be covered in photoresist, making it impossible to transfer the pattern to the surface by etching, or the resist would be overdeveloped, making the holes too large. Additionally, the etching rate also had to be found in order to obtain the desired hole depths for the different samples. The final parameters for the ten steps of the photolithography process and the etching process are given below.

For the first three steps of the photolithography process, the samples were only cleaned using methanol, and then blown dry by nitrogen (N_2). A primer was not applied, as the adhesion between the sample and the photoresist was sufficient for the processing performed.

The photoresist used was the negative photoresist, Micro Resist Technology ma-N 440. This was applied by spin coating, and spun for 15 seconds, where the rpm increased from 0 to 6600 in 10 seconds, before the sample was spun at 6600 rpm for the last five seconds. This was followed by a soft baking step at 35°C for 40 seconds and 90°C for 130 seconds.

The exposure was done with UV-light from a mercury arc lamp, having a wavelength of 365 nm. This was done in contact mode, and the exposure time was 37 seconds. As deep-UV was not used for exposure, a post-exposure bake was not necessary, and the photoresist was developed for about 75 seconds directly after exposure. During this time, the samples were continously moved, in order to avoid a stagnant solution around the sample surface.

Then, the pattern in the photoresist was visually inspected in a light microscope to see if the exposure and development were successful, and in order to see if there was any photoresist left in the bottom of the developed holes. If the pattern was of sufficient quality, the samples were then hard baked at 70 °C for 15 minutes. This temperature is lower than the typical temperatures for the hard bake step, due to the fact that the MCT material does not withstand the high temperatures usually used.

With the photolithography process being successful, the samples were then etched, in order to transfer the pattern to the sample surface. This was done by spin etching, with a Laurell EDC2-100-8NPP Spin Processor. The etch solution was 50 mL 1 % Br:HBr diluted in 500 mL of water. From testing procedures, it was found that the etch rate for the hole depth was about 35 nm/s. However, the holes were also etched horisontally, but with a lower etching rate. This made the lateral size of the holes dependent on the depth of the holes.

3.4 Photoluminescence spectroscopy

Photoluminescence (PL) is a process where light is emitted from matter after photon excitation. In PL spectroscopy, this physical effect is used to probe the electronic structure of materials, and for a semiconductor, the spectral distribution of PL can be analyzed to determine the electronic bandgap energy of the material.

Typically, a laser with higher energy than the bandgap energy of the investigated material is used as a light-source to excite electrons from their ground state. An electron-hole pair is then created, and if the relaxation of this electron-hole pair is radiative, a photon is emitted. The energy of the emitted photon will then reflect the transition energy of the electron-hole pair. The physical process itself is of the order of microseconds to nanoseconds after excitation, and the spectra obtained will consist of peaks at specific energies which are all related to specific radiative recombinations in the material. From these spectra, it is then possible to determine bandgap energies, impurity levels, defects and different quantum well properties, depending on the material being investigated.

The technique is non-destructive and contactless. This gives the advantage of a low possibility of damaging the sample, the same sample can be analyzed multiple times, and the samples can also be used for other purposes after being investigated.

3.4.1 FTIR

To obtain a spectrum from the emitted IR light, Fourier-Transform infrared spectroscopy (FTIR) can be used. As the name implies, a Fourier transform

is used to convert the collected data into a spectrum, which makes it possible to collect spectral data in a wide spectral range simultaneously. This makes the FTIR much more time efficient, as all frequencies can be measured simultaneously, compared to dispersive infrared spectrometers, which can only measure the intensity over a small interval of frequencies during one measurement.

The IR-spectrum is obtained by means of a Michelson interferometer, which is illustrated in Figure 3.7. The incoming IR-light is split by a beamsplitter (BS), and the reflected light is directed towards the moving mirror (M2), while the transmitted light continues toward the stationary mirror (M1). As the light is reflected in M1 and M2, it will once again be split by the BS. The transmitted light coming from M2 and the reflected light coming from M1 will then interfere. The phase difference, given by the path length difference, Δ, between the two beams, will then depend on the position of M2. The interference of the beams will give an intensity depending on Δ, which will create an interferogram, giving the intensity as a function of Δ. The interferometer is typically scanned for a given time, for instance 3 minutes, and the signal at a given point in the interferogram is then the average value of the signal at the corresponding position of M2 for each scan. The spectral data can then be obtained by taking the Fourier transform of this interferogram. For a given path length difference, the interferogram, $I(\Delta)$, is given by [29]:

$$I(\Delta) = \frac{I(0)}{2} + \int_{-\infty}^{\infty} S(k)\cos(2\pi k\Delta)dk \tag{3.1}$$

Here $S(k)$ is the intensity of a wavenumber k, and $I(0)$ is the intensiy when the path difference is zero, which is when M1 and M2 are situated at the same distance from BS, and gives the mean intensity. To obtain the spectrum, a Fourier transform then has to be performed:

$$S(k) = \int_{-\infty}^{\infty} \left(I(\Delta) - \frac{I(0)}{2}\right)\cos(2\pi k\Delta)d\Delta \tag{3.2}$$

When FTIR spectroscopy is performed, there will also be radiation from the background present. To obtain a spectrum only containing radiation from the investigated sample, it is therefore also necessary to record an interferogram of the background, and substract the background from the measurements of the sample. It is then important to do this substraction in the correct way

to avoid errors. As the interferogram from the total spectrum (emitted light from the sample and background radiation) will contain background radiation entering from the detector side, having constructive and destructive interferences at other mirror positions than the signal from the sample, a Fourier transform of this will create a false wavenumber spectrum [30]. The right way to obtain the final spectrum is therefore to substract the two interferograms before the Fourier transform is done, and not simply substract the two spectra obtained.

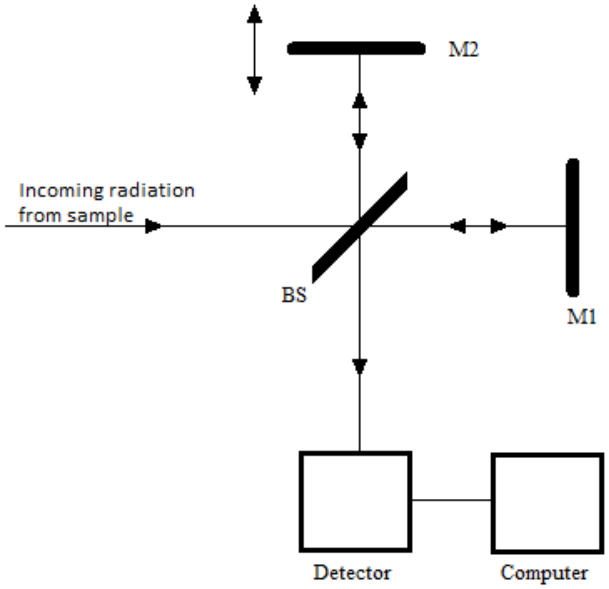

Figure 3.7: Illustration of the Michelson interferometer, where BS is the beam splitter. M2 is the moving mirror, which is mobile in the beam direction, while M1 is stationary. The detector is AC coupled to an audio frequency amplifier, digitized and stored by a computer [30]. As M2 has a constant velocity, the optical path difference, and thereby the phase difference varies linearly with time.

When performing FTIR, one also has to be aware of atmospheric absorption. Both H_2O and CO_2 have absorption lines in the infrared parts of the electromagnetic spectrum [31]. To avoid including these absorption lines in the spectra, it is necessary to flush the beam path between the sample and detector with nitrogen gas (N_2).

3.4.2 Experimental procedure

The PL spectroscopy measurements were done by using a Bruker IFS 66 FTIR spectrometer. This spectrometer has a resolution of 4 cm^{-1}. The detector in the spectrometer was cooled by liquid nitrogen and could detect radiation with a wavelength within the interval of ≈ 1 μm to ≈ 8 μm. For these experiments, several samples with different normalised grating periods ($\frac{a}{\lambda}$), layer thicknesses in the strucure, and emission wavelengths were studied. The samples were studied with two different sample holders, one that was flat (sample holder A), and one that had an inclination of 21° relative to the normal of the plane of the beam propagation (sample holder B).

The samples were glued to a molybdenum plate with a 9.4 x 2.8 mm^2 hole in the middle. The choice of molybdenum is due to its thermal expansion coefficient close to the one of MCT, which prevents stresses to build up during the heating and cooling. The molybdenum plate was afterwards screwed onto a sample holder of aluminum, and an indium foil was situated between the sample holder and the molybdenum plate, in order to give good thermal contact between them.

The sample holder was then mounted on a coldfinger. This coldfinger was used to control the temperature of the samples, by using a He(g) closed-cycle cryostat. In combination with a heating element, the temperature could then be controlled between 10 and 300 K. The cryostat was also connected to a turbomolecular pump, in order to perform the experiments under vacuum conditions. When performing the measurement, the temperature should be as low as possible, as the PL-intensity in general increases with decreasing temperatures for MCT samples [6, 25]. However, for some of the samples in this study, the PL-intensity decreased at the lowest temperatures, and the measurements therefore had to be performed at higher temperatures in order to get a higher intensity and thereby better statistics. PL-measurements were therefore performed at a few different temperatures.

The laser source used to generate electron-hole pairs in MCT was an IR-laser with a wavelength of 2.01 μm. This corresponds to an energy of 0.62 eV, and it can therefore generate electron-hole pairs in MCT with an x-value up to $\approx$ 0.52 at 11 K. By aligning the beam trajectory correctly, the laser light enters the sample from the substrate side, while the emitted photons exiting through the CdTe-layer are measured by the FTIR spectrometer. An illustration of this is shown in Figure 3.8. In addition, the entire path between the sample

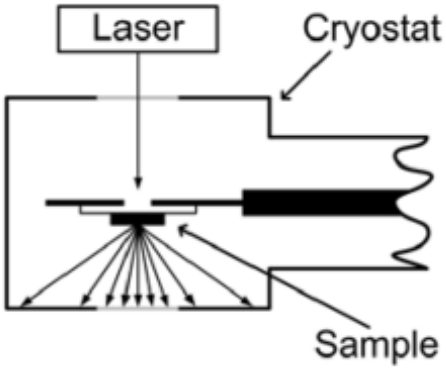

Figure 3.8: Illustration of the cryostat in the plane of the laser beam propagation [2].

and detector was flushed with nitrogen to avoid atmospheric absorption, and a filter was placed in front of the FTIR spectrometer in order to block the laser light from reaching the detector.

When doing the measurements, the optics and detector were held stationary, while the cryostat was moved. This made it possible to scan the laser beam across the sample, which is illustrated in Figure 3.9, and thereby obtain spectra from both the patterned and unpatterned areas, which were analyzed to find the integrated intensity of the PL peaks. The optics put certain limitations on the measurements, as the collection mirror only covers an angle of $\pm 18.6^\circ$ around the surface normal, which limits the amount of PL light that can be detected.

It should also be said that the units of the intensity measured are somewhat arbitratry, as many mechanisms can reduce the PL-intensity to a large extent, both in the light-generating material itself, and the experimental setup. For the latter, small adjustments in the laser intensity, the sample not being completely in focus, and small changes in the position of the mirrors guiding the radiation from the sample to the detector are examples causing relatively large changes in the measured intensity. As for instance the two first have to be adjusted for each sample, it is hard to guarantee that the experimental setup is completely the same for all measurements. In addition, the quality of the material may also vary from sample to sample, causing differences in the absolute measured intensity, due to different fraction of the recombinations being radiative in each sample. As small changes in the experimental setup and the material might cause relatively large changes in the measured

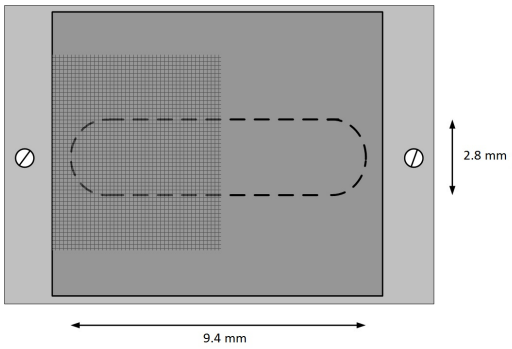

Figure 3.9: Illustration of the molybdenum plate to which the sample is glued [2]. The figure illustrates that about half of the opening where the laser can go through the sample holder and interact with the sample is covered by the surface pattern of the sample, while the other half is covered by the unpatterned area.

intensity, the different samples should therefore be compared by the ratio between the patterned and unpatterned area of the sample, and not by the absolute value of the measured intensity.

When the spectra were obtained, the integrated intensity of the PL peaks were found by using peak fit in the commercial software PeakFit [32]. This procedure also made it possible to distinguish different subpeaks from one another, saying something about the material properties themselves.

Chapter 4

Simulations

4.1 Finite-difference time-domain

The finite-difference time-domain (FDTD) method solves the time-dependent Maxwell equations by discretizing them, using the central-difference approximation, to the space and time partial derivatives. Yee's mesh [33] is then used, and the electric (E) and magnetic field (H) components are solved at each mesh point based on the spatial E and H field components of previous time steps. An illustration of a typical 3D Yee grid, being the building block of the mesh, is shown in Figure 4.1. As the field components and time has to be discretized, it is important to choose Δx, Δy, Δz and Δt to be small enough for the numerical solution to be valid. As a rule of thumb, the grid size should be a maximum of one tenth of the wavelength of light in the medium with highest refractive index, and not larger than the smallest feature of the simulated structure [34].

A disadvantage of the FDTD method is that it requires extensive use of time and computer memory. Due to this resource demand, it is not unusual to do 2D and 3D simulations in combination [35]. The initial optimisation of the different structural parameters can be done in 2D, while the simulations of the optimised system can be done in 3D for better quantitative results. When simulating the structure, it is also common to do simplifications, such as simulating only a section of the structure. However, it is important that the truncations are done so that the underlying physics involved in the structure is not changed to a large extent.

When using the FDTD method, a software designed for this purpose is often

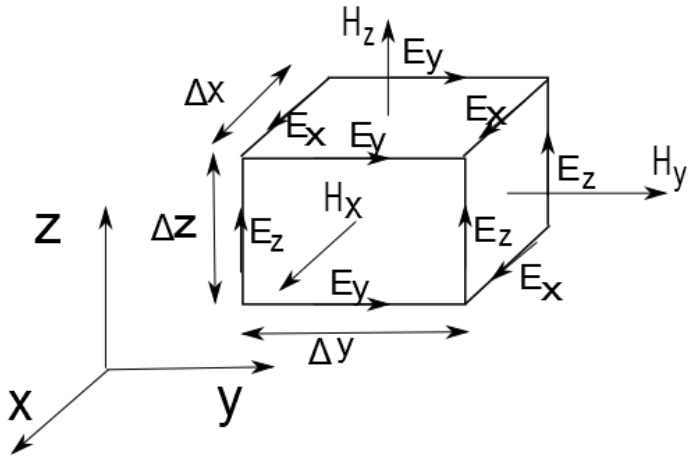

Figure 4.1: Illustration of the 3D Yee grid and the discretization of the E and H field components.

used. Two commonly used examples are Meep [36] and OptiFDTD [37]. In this study, OptiFDTD is used, and the emphasis will therefore be on this software. For details regarding this software and its features, it is referred to the online manual [37]. In short, the program allows you to design a structure in both 2D and 3D with user-defined materials, and define the position and properties of the input wave, which can be a plane wave or a point source. The radiated power at a given line or area in space can also be calculated by integrating the normal component of the Poynting vector over this observation line or area, in order to find the light extracton efficiency of a structure. An example of a simulation design in shown in Figure 4.2.

When simulating only a section of the structure, it is important to consider which boundary conditions should be used to deal with both the reduced size of the simulation and the finite size effects. In OptiFDTD, there are four possibilities. These are perfectly matched layers (PML), a perfect electrical conductor (PEC), a perfect magnetic conductor (PMC) and periodic boundary conditions (PBC). Using PML, the sides of the structure are attached to a numerically absorbing boundary which suppresses the reflections. In practice, the radiation will then disappear when propagating through the boundary. For PBC, the boundaries are periodic, so that if the structure has a width p in the x-direction, $H(x+p)$ is equal to $H(x)$. PMC/PEC are special cases of the PBC condition.

Simulations of the samples

In my project assignment [1], the parameters of the surface pattern were optimised by performing 2D simulations with the free 32 bit version of the software OptiFDTD by Optiwave [37]. These simulation led to four different sample designs with 2D optimised grating period (a), fill factor (ff) and thickness of the CdTe-layer (h). Here, the fill factor is the fraction of CdTe in one unit cell of the surface pattern. The next step, which is performed in this study, is to do 3D simulations for the 2D optimised structures, to calculate more accuratly the expected enhancement in light emission due to the surface pattern.

This was performed with the OptiFDTD 12.0 software. The simulation design can be seen in Figure 4.2, and the material properties for each of the layers are summarized in Table 4.1. The PL-measurements were performed at several temperatures for the samples, due to the different temperature-dependence of the PL-intensity of the individual samples. As PL-measurements were performed at 140 K for all samples except one, the simulations are also done at this temperature. Figure 4.2 shows that the 3D simulations made it possible to simulate a triangular surface pattern of air holes, which was not possible in the 2D simulations performed for optimisation of the surface pattern parameters. The simulation design itself is similar to what has been done by Cui and Park [38], Zhang et. al [39], Zhu et. al [40] and Park et. al [41], only modified to fit the structures used in this study.

Table 4.1: The material properties used in the FDTD-simulations. The refractive indices are given for 140 K.

Layer	Refractive index	Thickness [μm]
CdTe	2.65 [42] [43]	0.4-1
MCT	3.4 [42] [2]	1-4.5
CdTe (Bragg)	2.65 [42] [43]	0-0.71
MCT (Bragg)	3.4 [42] [2]	0-0.63
CdZnTe	2.65 [44]	1

The input wave source is as in [38–41] a single point source. In the experimental setup, a laser source with a wavelength of 2 μm is used to generate electron-hole pairs, which will quickly relax down to the bottom/top of the conduction/valence band and recombine radiatively. As MCT with the x-value used in the simulations (x=0.29) has an absorbtion coefficient of about

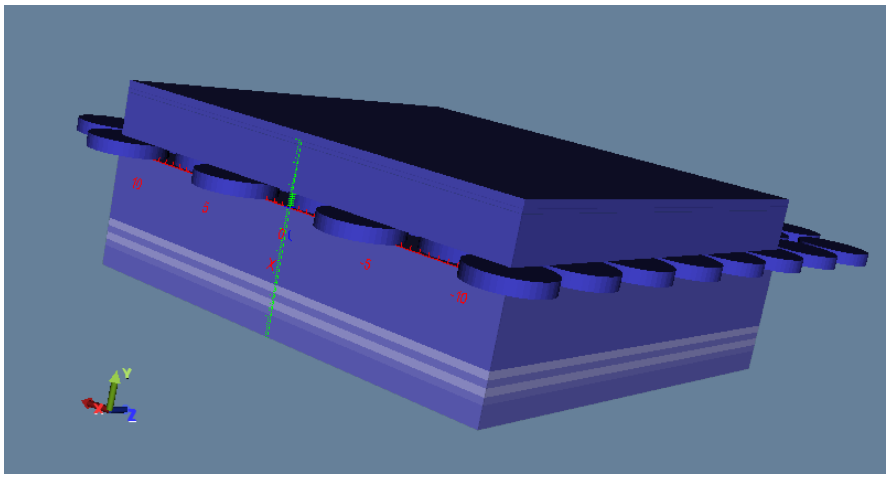

Figure 4.2: An example of a design being simulated by the FDTD method. The layers are from bottom to top: CdZnTe, the layers in the DBR, MCT, CdTe and air. The cylindrical shapes are air holes in a CdTe-layer. The layer seen on top of these cylinders is also air. The point source is inside the MCT-layer, and the observation area is at the top of the air layer. The size of the structure in the y-direction varies depending on the number of layers in the structure, but is always 24 μm in the x- and z-direction.

10^4 cm^{-1} at this wavelength [25], the sources are situated at different depths in the active layer, with the majority of them close to the interface between the active layer and the substrate/DBR. The emitted photons from the radiative recombinations of electrons and holes will have random directions, phases and polarisation, and are therefore treated as incoherent. To represent this, only a single Gaussian time-modulated point source was used per simulation, in order to avoid coherent effects between multiple point sources [45]. At the same time, to simulate the random polarisation, three simulations were performed for the same point source, with polarisation in the x-,y-, and z-direction. The results were then added incoherently for each of the three simulations.

In order to find the emerging light extraction from the structure, the transmitted power is calculated in an observation area above the surface of the structure. The power can then be compared to a the power emitted from a reference structure, which has an unpatterned CdTe-layer of the same thickness, in order to find the enhancement in light emission due to the surface pattern.

As only a single point source was used, the calculated power would depend strongly on the position of this source, both laterally within the unit cell of the surface grating, and vertically inside the active layer. To find the expected light extraction efficiency from each simulated structure, the light extraction from different positions within the unit cell was averaged. Figure 4.3 shows that by calculating the running average for each simulated position, it was necessary to have more than 75 different positions within the unit cell simulated to have a stable average calculated power. The simulation was therefore run individually for 100 different random positions within the unit cell, and the simulated power was then the average power from these positions. As more sources will be present close to the interface between the active layer and the substrate/DBR, the depth of the source was also taken into consideration when performing the averageing. This was done by splitting the active layer into 10 segments, where the absorption coefficient was used to calculate the fraction of light generated in each segment. The resulting power from each segment was then weighted by these fractions.

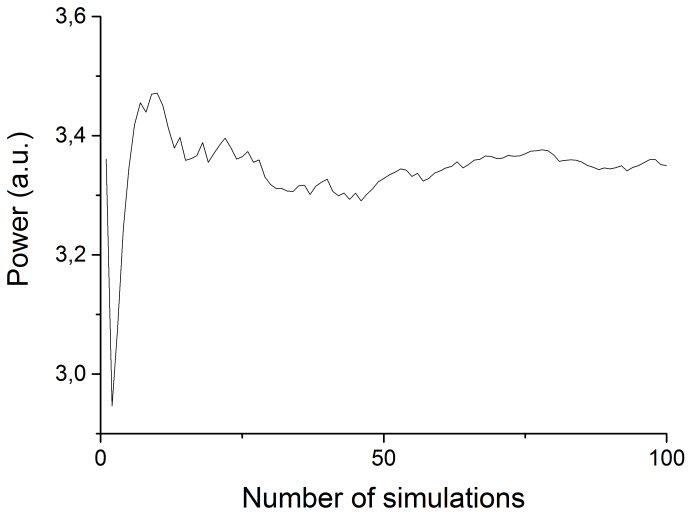

Figure 4.3: Running average calculated power versus the number of simulations. The average value stabilizes after approximately 75 simulations.

By averageing the simulated power from the different positions and polarisations of the point source, a total spectrum from the sample is obtained. The parameters of the Gaussian modulated point source are then designed in a manner trying to cover the same wavelengths as the experimentally ob-

tained spectrum of the sample. The simulated enhancement can then be found by dividing the integrated intensity from the simulated spectrum of the processed area with the integrated intensity from the unprocessed area. By normalising the simulated spectrum of the different areas of the sample to the spectrum of the point source, the LEE for different wavelenghts can also be found for both the processed and unprocessed area. This can be used to see how the LEE depends on the wavelength for both areas of the sample.

Perfectly matched layers (PML) were used as boundary condition for all sides of the simulation domain. The reason for this was to avoid unnecessary reflection of light at the boundaries [40]. If periodic boundary conditions had been used, the point sources would have been placed in a periodic manner, and radiated coherently, which would have introduced physical effects not present in the structure. The thickness of the substrate has also been greatly reduced from its physical size in the simulations, due to the PML boundary conditions. Using these boundary conditions for the substrate is most likely a valid approach, as the emitted photons going into the substrate are seen as lost due to its large thickness.

The rule of thumb for mesh sizes has to be fulfilled. The structures simulated have different thickness of the different layers, and different wavelengths of the emitted light. Constant values for Δx, Δy, Δz, or Δt are therefore not used, but are instead adapted to the central wavelength of the point source and the thicknesses of the layers. The number of time steps also varies depending on the structure. When performing the simulation, the calculated power in the observation are will increase for each time step until a stable level is reached, and the number of time steps is the number necessary to reach this level.

4.2 Transfer matrix method

In order to compare the LEE of the samples in the unprocessed areas for different wavelengths, the transfer matrix formulation for multilayer systems was used, which is described in detail in [20]. The main parts of the theory described there is given in this section; however, some modifications have been made, as the source of radiation in this study is inside the sample, while [20] accounts for incoming radiation from an external source. Similar simulations are done with FDTD, but due to the method's high time and memory consumption, the FDTD-simulations are limited to simulations of

the actual structure and wavelengths, while the transfer-matrix method is used to investigate the response of changing many of the possibe input parameters, such as the refractive indices, thicknesses of layers and wavelength of the source.

Here, the multilayer system is constructed in 1D, where each layer is of uniform thickness, and the interfaces are planar. In the case explained here, the waves are in the xz-plane, so that $k_y = 0$. Layer i has a refractive index n_i, which may be complex, and a thickness d_i. The waves are described by one forward-propagating and one backward-propagating wave in the x-direction, denoted respectively A and B. This is shown in Figure 4.4. As the structure is in 1D, it is sufficient to treat the problem for two orthogonal polarisations, the transverse electric (TE) and the transverse magnetic (TM). The TE-waves will have the electric field parallell to the interfaces, while the TM-waves will have the electric field normal to the interfaces. This will lead to different equations for the reflectivity and the transmittivity for the two polarisations, as can be seen in the next paragraph.

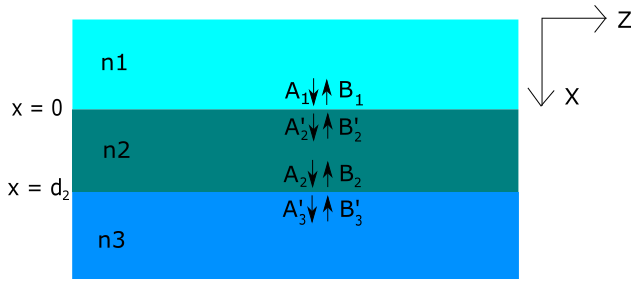

Figure 4.4: The principle of the transfer matrix method. Layer 1 is the layer of the incident wave, and the interface between layer 1 and 2 is denoted as $x = 0$. A and B denote the forward and backward-propagating wave, where the subscript shows the layer number. With no prime, the wave is infinitesimaly above the interface, while the prime shows that is it located infinitesimally below the interface.

To find the relationship between A_i, A'_{i+1},B_i and B'_{i+1}, the Fresnel equations for reflection and transmission for the two different polarisations are used. These are written as:

$$
\begin{aligned}
r_{ij} &= \frac{n_i \cos\theta_i - n_j \cos\theta_j}{n_i \cos\theta_i + n_j \cos\theta_j} \text{ TE-polarisation} \\
t_{ij} &= \frac{2n_i \cos\theta_i}{n_i \cos\theta_i + n_j \cos\theta_j} \text{ TE-polarisation} \\
r_{ij} &= \frac{n_j \cos\theta_i - n_i \cos\theta_j}{n_j \cos\theta_i + n_i \cos\theta_j} \text{ TM-polarisation} \\
t_{ij} &= \frac{2n_i \cos\theta_i}{n_j \cos\theta_i + n_i \cos\theta_j} \text{ TM-polarisation}
\end{aligned}
\tag{4.1}
$$

Here θ_i is the incidence angle of the light in layer i. The r and t-coefficients are the ratios of the reflected or transmitted waves' electric field amplitude to that of the incident wave. By using these equations, the relationship between the four waves can be written as:

$$
\begin{bmatrix} A_i \\ B_i \end{bmatrix} = D_{ij} \begin{bmatrix} A'_j \\ B'_j \end{bmatrix} \tag{4.2}
$$

For $D_{ij} = \frac{1}{t_{ij}} \begin{bmatrix} 1 & r_{ij} \\ r_{ij} & 1 \end{bmatrix}$. Where j in this case is $i+1$. For each interface, a relationship between the different waves on each side of the interface is established. The next part is to include the forward- and backward-propagating waves in layer i:

$$
\begin{bmatrix} A'_i \\ B'_i \end{bmatrix} = P_{ij} \begin{bmatrix} A_i \\ B_i \end{bmatrix} \tag{4.3}
$$

Here $P_i = \begin{bmatrix} e^{j\phi_i} & 0 \\ 0 & e^{-j\phi_i} \end{bmatrix}$, and $\phi_i = k_{x,i} d_i = \frac{2\pi}{\lambda_0} n_i d_i \cos\theta_i$, where λ_0 is the vacuum wavelength.

As (4.2) and (4.3) are combined, the waves at all the different positions in Figure 4.4 can be found. The relationship between waves in layer i and p is then:

$$
\begin{bmatrix} A_i \\ B_i \end{bmatrix} = D_{i,i+1} P_{i+1} D_{i+1,i+2} \cdots P_{p-1} D_{p-1,p} \begin{bmatrix} A'_p \\ B'_p \end{bmatrix} \tag{4.4}
$$

In this study, it is interesting to find the waves propagating out of the structure, given the waves originating at the source. This is illustrated in Figure

4.5, where the amplitude of the wave propagating out of the structure is denoted E_R, the amplitude of the waves originating from the source E, and the amplitude of the wave propagating into the substrate E_L. There are no external sources of radiation, meaning that there are no waves propagating into the structure from the outside.

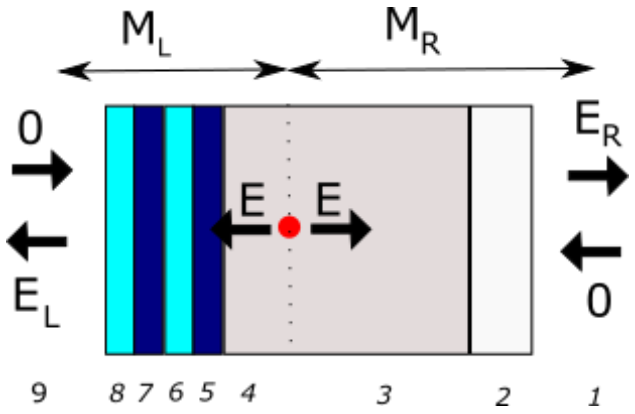

Figure 4.5: Illustration of the transfer matrix method for the samples used in this study, where the source of radiation is situated inside the structure. E_R and E_L are the waves propagating away, respectively to the right and left, and M_L and M_R are the transfer matrices between the source and the outermost layer to the left and right. Layer 1 and 9 are assumed to have infinite extension.

If it is assumed that the source is situated infinitesimaly to the right of the mathematical interface between layer 3 and 4, the source radiates $\begin{bmatrix} 0 \\ E \end{bmatrix}$ to the left and $\begin{bmatrix} E \\ 0 \end{bmatrix}$ to the right, with an incidence angle θ_i. The relationship between the amplitude of the waves propagating to the left from the source, and the waves in the leftmost layer can then be written as:

$$E_i + \begin{bmatrix} 0 \\ E \end{bmatrix} = M^L \begin{bmatrix} 0 \\ E_L \end{bmatrix} \tag{4.5}$$

Here (4.4) is used, and $M^L = D_{34}P_4D_{45}P_5D_{56}P_6D_{67}P_7D_{78}$, while E_i is the induced wave. For the right-hand side of the structure, the relationship becomes:

$$M^R(E_i + \begin{bmatrix} E \\ 0 \end{bmatrix}) = \begin{bmatrix} E_R \\ 0 \end{bmatrix} \tag{4.6}$$

For $M^R = D_{12}P_2D_{23}P_3$. In order to find E_R, (4.5) and (4.6) must be combined. This is done by solving the two equations for E_i:

$$M^R(M^L \begin{bmatrix} 0 \\ E_L \end{bmatrix} - \begin{bmatrix} 0 \\ E \end{bmatrix} + \begin{bmatrix} E \\ 0 \end{bmatrix}) = \begin{bmatrix} E_R \\ 0 \end{bmatrix} \tag{4.7}$$

$$\Downarrow$$

$$M^R M^L \begin{bmatrix} 0 \\ E_L \end{bmatrix} - \begin{bmatrix} E_R \\ 0 \end{bmatrix} = M^R \begin{bmatrix} -E \\ E \end{bmatrix} \tag{4.8}$$

Both M^R, M^L and the matrix multiplication of them will be 2x2 matrices. The next step is therefore to write (4.8) as two equations:

$$\begin{aligned} M_{12}^{RL}E_L - E_R &= E(-M_{11}^R + M_{12}^R) \\ M_{22}^{RL}E_L &= E(-M_{21}^R + M_{22}^R) \end{aligned} \tag{4.9}$$

Here $M^{RL} = M^R \cdot M^L$. The subscripts gives the matrix indices of the given variable.

The relationship between the amplitude of the waves propagating away from the structure and the waves from the source can then easily be found:

$$\begin{aligned} \frac{E_R}{E} &= M_{12}^{RL}\frac{M_{22}^R - M_{21}^R}{M_{22}^{RL}} + (M_{11}^R - M_{12}^R) \\ \frac{E_L}{E} &= \frac{M_{22}^R - M_{21}^R}{M_{22}^{RL}} \end{aligned} \tag{4.10}$$

Simulations of the unprocessed areas of the sample

Although the unprocessed area of the samples was simulated with the FDTD-method to calculate the enhancement in light emission due to the surface pattern, transfer matrix method Matlab [46] simulations where also performed to save time and memory, compared to the FDTD-simulations, for the unprocessed area of the sample. The transfer matrix simulations were therefore performed to see how the LEE of the structure changed when important parameters, such as the refractive index and thickness of the layers, were altered.

As the emitted light from the sample will not be monochromatic, the main use of the transfer matrix simulations was to see how the LEE varies in the

unprocessed area of the sample for the different wavelengths emitted. This was performed for varying refractive indices and range of wavelengths, to see how it fitted to experimental results obtained. Transfer matix simulations was also performed instead of FDTD-simulations when the needed range of wavelengths was larger than included in the results of the FDTD-simulations.

The idea behind the simulations is that the emitted photons will radiate with a random incidence angle to the interfaces of the structure, and the LEE is therefore found for all angles up to the critical angle for total internal reflection between MCT and air. Table 4.2 gives the material properties used in the simulations, and from the refractive indices given there,this angle will be 17.1°. In order to analyse the LEE of the structue, the average of LEE over all the simulated angles are combined.

The simulation domain is shown in Figure 4.5, where layer 1 is air, layer 2 is the passivation layer of CdTe, layer 3 and 4 is the active MCT-layer, layer 5-8 is the DBR, with alternating CdTe and MCT-layers, and layer 9 is the substrate of CdZnTe. As for the FDTD-simulations, it is assumed that the substrate is of infinite extension, meaning that the radiation propagating into the substrate will be lost, and the light reflected at the substrate/air interface is not taken into consideration. The thicknesses of the different layers are the thicknesses found for each individual sample from SEM-pictures of the cross section of the sample.

Table 4.2: The material properties used in the transfer matrix simulations. The properties are given at 140 K. In some of the cases, the reference has not given the value explicitly at 140 K, and no reference was found for the property at this temperature. Interpolation by using the general trend in temperature was then used.

Material	Refractive index ($\lambda \approx 5$ μm)
MCT ($x \approx 0.3$)	$\approx$ 3.4 [42] [2]
MCT ($x \approx 0.6$)	$\approx$ 3 [42]
CdZnTe	$\approx$ 2.65 [44]
CdTe	$\approx$ 2.65 [42] [43]

Although the laser light creating photoluminescence is incident through the substrate and DBR, and into the active layer, it will be absorbed throughout the whole depth of the active layer. The source was therefore situated at different depths into the active layer, and the total LEE at a given wavelength was seen as the weighted average of the calculated LEE at different source depths. The different LEE were weighted by the fraction of light being absorbed at a given depth, as more light will be absorbed, and thereby emitted, close to the interface between the active layer and the DBR.

Chapter 5

Results and discussion

In this chapter the samples will first be presented, before the results of the PL-measurements are given. Then, the enhancement in light emission due to the surface pattern from the different samples are compared, and the important parameters in the sample design are discussed. In addition, other important aspects of this study are also discussed.

5.1 Samples

The structures of the samples were shown in Figure 3.1 and 3.2. Table 5.1 lists the important sample and surface pattern parameters, while Table 5.2 gives the enhancement in light emission for the different samples measured by the means of PL with sample holder A and simulated by FDTD. Unless stated otherwise, all of the results from the PL-measurements in this chapter are obtained with this sample holder. The PL-intensity is in general increasing with decreasing temperatures for MCT samples. However, the opposite trend was seen for many of the samples in this study, and for some samples, the temperature therefore had to be increased to 140 K to perform PL-measurements. The reason behind this will be discussed later. In this section, only the most important aspects about the different samples are presented. Additional data is given in appendix A.

Table 5.1: Overview of the parameters of the surface pattern and the different layers of the samples. The given depth of the holes is at their deepest.

Sample	x	Thickness active MCT-layer [μm]	Thickness CdTe (Passiv.) [nm]	Thickness MCT (Bragg) [nm]	Thickness CdTe (Bragg) [nm]
PCC752-3	0.35	MQW	428	-	-
PCC793-3	0.289	3.00	701	-	-
PCC793-4	0.289	2.96	744	-	-
PCC794-1	0.289	3.18	751	412	453
PCC794-3	0.289	3.18	751	412	453
PCC794-4	0.289	3.18	751	412	453

Sample	Grating period (a) [μm]	Depth holes [nm]	ff	DBR
PCC752-3	4.5	500	0.37	-
PCC793-3	4.5	600	0.40	-
PCC793-4	4.5	750	0.28	-
PCC794-1	4.5	675	0.32	X
PCC794-3	4.5	600	0.06	X
PCC794-4	6.0	800	0.38	X

Table 5.2: Results of the PL-measurements and 3D FDTD-simulations of the different samples. The temperature used for simulation determines the refractive indices and the wavelength of the emitted light.

Sample name	Temperature [K]	$\frac{a}{\lambda}$	Enhancement (PL) [%]	Enhancement (FDTD) [%]
PCC752-3	11	1.61	55	54
PCC793-3	11	0.80	100	-
PCC793-3	140	0.97	48	31
PCC793-4	11	0.80	163	-
PCC793-4	140	0.97	74	41
PCC794-1	140	$\approx$0.97	92	31
PCC794-3	140	$\approx$0.97	52	5
PCC794-4	140	$\approx$0.97	123	46

5.1.1 PCC752-3

PCC752-3 contains multiple quantum wells (MQW). This sample was grown for an earlier study at FFI [2], and its structure is shown in Figure 3.2, where the active part of the structure is the MQW. In the earlier study at FFI [2], a similar sample was used, but the holes were not etched all the way through the passivation layer. Simulations indicated that doing so could increase the LEE. PCC752-3 also has a larger normalised grating period than the other samples, and can therefore be used to test how this influences the enhancement in light emission.

A small, but representative, area from the central region of the surface pattern is shown in Figure 5.1. The etched holes seem quite uniform, and have a radius giving a fill factor of about 0.37. The height profile of the surface, however, shows that the spin ethcing lead to holes not having a completly cylindrical shape.

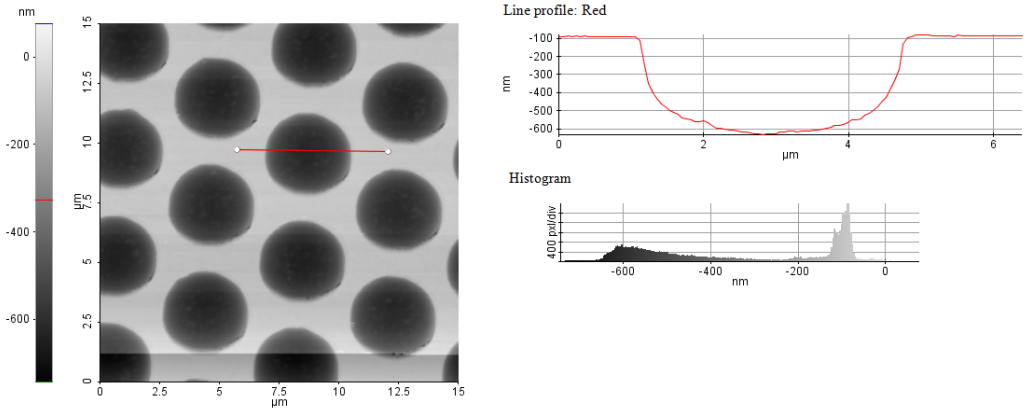

Figure 5.1: Image obtained by an atomic force microscope (AFM) showing a representative area of the surface pattern of PCC752-3, with the height profile of the red line visible. The histogram indicates the number of pixels in the image with a given height. For this and the other AFM-images, the images themselves were obtained by Torgeir Lorentzen.

Figure 5.2 shows spectra from the patterned and the unpatterned areas of the sample. The light emission is enhanced due to the surface pattern, but the enhancement is different for the two peaks. The reason for this not fully understood, but as the peaks are only separated by 150 cm^{-1}, or by less than 0.1 in the unit of $\frac{a}{\lambda}$, it is unlikely that it is due to their different normalised

grating periods, which will be shown in section 5.2.1. It is therefore more likely that the results can be explained by the material itself. Due to small variations in the material, one of the recombination processes might take place more frequently in one area of the sample than the other. To calculate an enhancement in light emission as independent from the material variations as possible, the enhancement for both of the peaks combined will be emphasised, rather than the enhancement for the individual peaks.

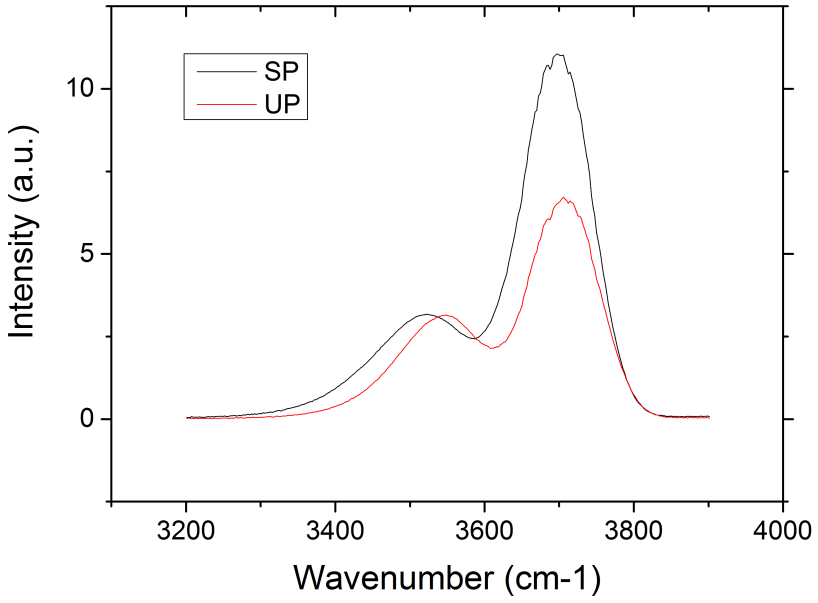

Figure 5.2: Spectrum obtained from the patterned (SP) and unpatterned (UP) area of PCC752-3 measured at 11 K.

3D FDTD-simulations support that the difference in enhancement for the two subpeaks is due to intrinsic material properties. By dividing each of the spectra in Figure 5.2 by their respective FDTD-simulated wavenumber-dependent LEE, the spectra plotted in Figure 5.3 are obtained. These spectra will then predict the PL-spectrum of the source inside the sample. It will be seen later that for the other samples studied, the shape of this spectrum is identical for the patterned and unpatterned area of the sample, indicating identical material properties for the two areas. However, for PCC752-3, the ratio between the amplitude of the low-energy and high-energy peak is different for the two areas, indicating that the enhancement in light emission differs for the two subpeaks due to intrinsic material properties.

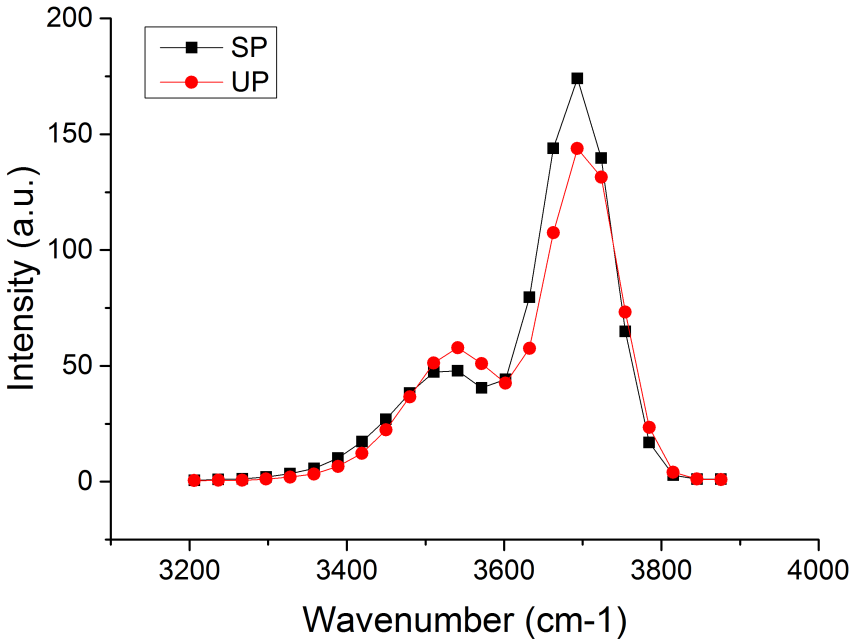

Figure 5.3: The predicted spectrum inside PCC752-3, when dividing the experimentally obtained spectra from the patterned (SP) and unpatterned (UP) area by their respective FDTD-simulated LEE.

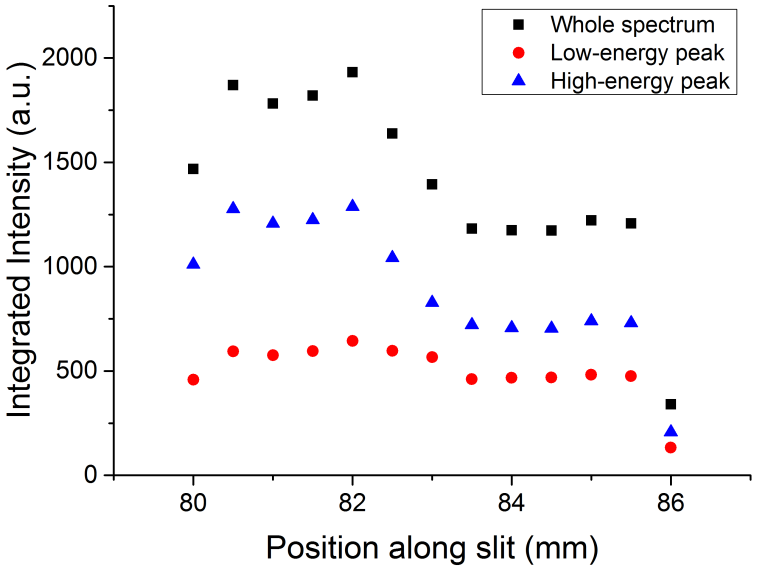

Figure 5.4: The measured integrated intensity from PL-spectra at different positions on the sample.

The integrated intensity from the spectra measured at different points on the sample can be seen in Figure 5.4. Two plateaus are obtained, where the upper one shows the patterned area, and the lower one shows the unpatterned. By taking the average value of the two plateaus, it is found that the enhancement in light emission is about 55 % when taking both peaks into consideration. The individual enhancement for the two peaks is 73 % for the high-energy peak and 27 % for the low energy peak.

5.1.2 PCC793

The two samples PCC793-3 and PCC793-4 come from the same MBE-grown structure. The active layer in both samples is a thin film, and the main differences between the two are the thickness of the passivation layer and the depth of the holes. How these differences affect the LEE and enhancement in light emission will be investigated. PCC793-4 is in addition similar to PCC794-1, except from not having a DBR. This is used to investigate the effect of the DBR.

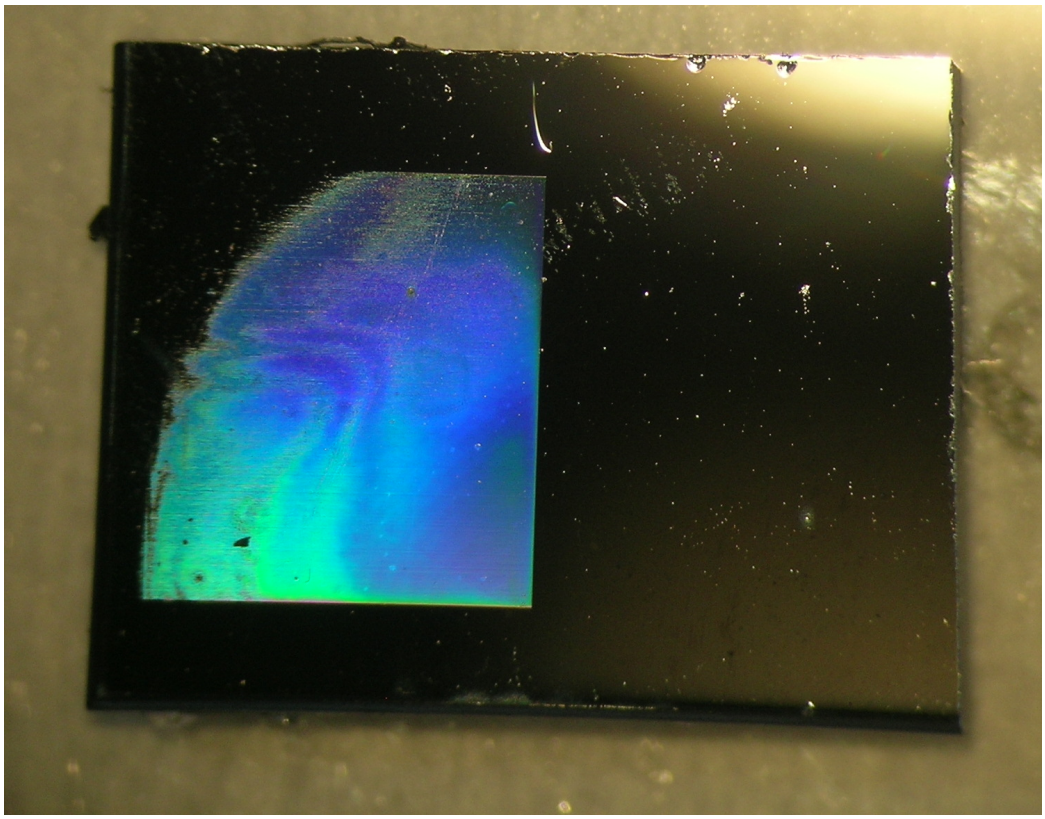

Figure 5.5: Image of PCC793-4, showing the variation in the quality of the surface pattern. The black areas are unpatterned, while the coloured one is the surface pattern.

Figure 5.5 shows that PCC793-4 has a varying quality of the surface pattern across the patterned areas. The areas close to the central region of the sample have a more uniform surface pattern of better quality. This can be seen as the areas with the best quality have a much more uniform interference of the light than the areas with lower quality of the pattern. The holes on both samples showed a similar height profile as the other samples investigated, with a not fully cylindrical shape, represented for PCC793-4 in Figure 5.6.

Figure 5.7 shows spectra from the patterned and unpatterned areas of PCC793-4 at respectively 11 K and 140 K. The shape of the peaks are different at the two temperatures, as the peaks at 140 K have a larger full width at half maximum (FWHM), which is as expected [6]. The spectra of PCC793-3 are qualitatively equal, although they quantitatively differ.

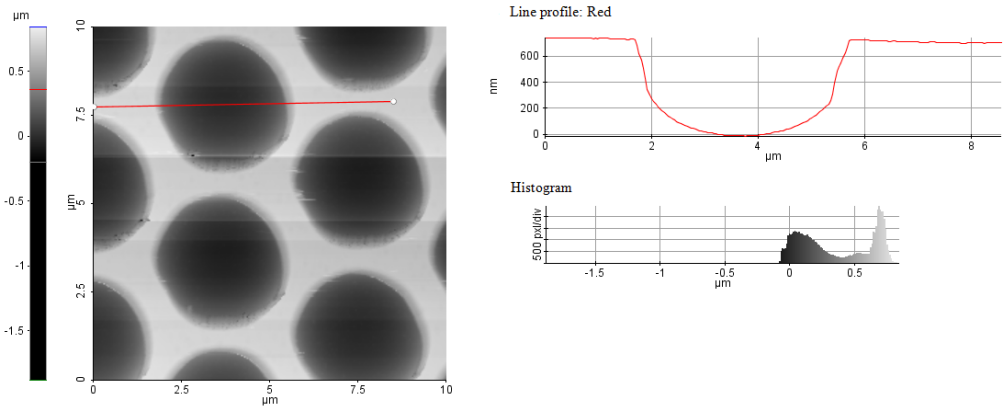

Figure 5.6: AFM-image showing a representative area of the surface pattern from the central region of PCC793-4, with the height profile of the red line indicated. The histogram indicates the number of pixels in the image with a given height.

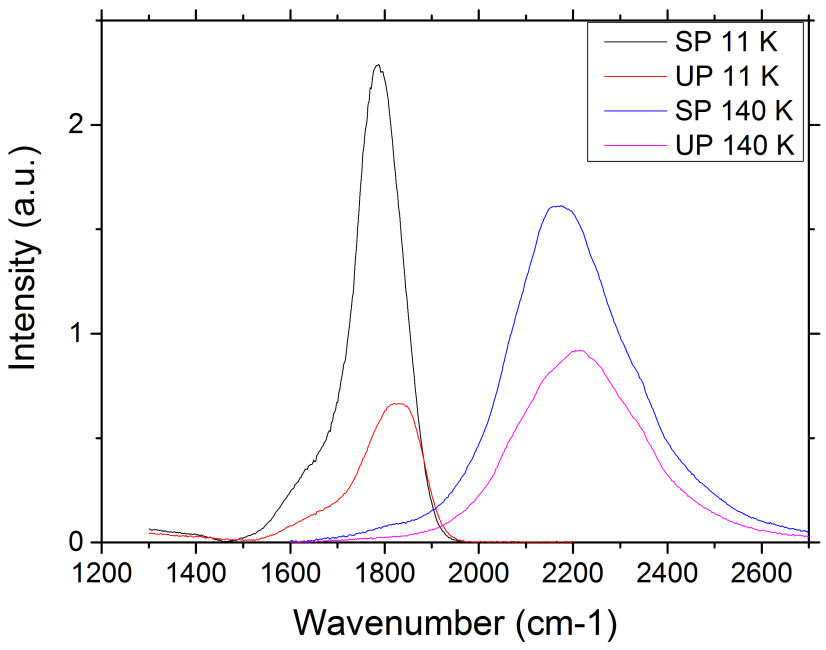

Figure 5.7: Spectra obtained from the patterned (SP) and unpatterned (UP) area of the PCC793-4 at 11 K and 140 K.

3D FDTD-simulations were performed to find the spectrum inside the active MCT-layer of PCC793-4. These simulations are shown in Figure 5.8, and revealed a symmetric spectrum containing only one distinct peak, which most likely is due to band-to-band transitions. These spectra were calculated by dividing the experimentally obtained spectra at 140 K in Figure 5.7 by their respective FDTD-simulated wavenumber-dependent LEE. As the spectra from both the patterned and unpatterned area of the sample have the same shape, and only differ by a multiplication factor, it is very likely that they indicate the experimental spectrum inside the MCT-layer. Additionally, it also shows that the FDTD simulations work very well, apart from a multiplication factor.

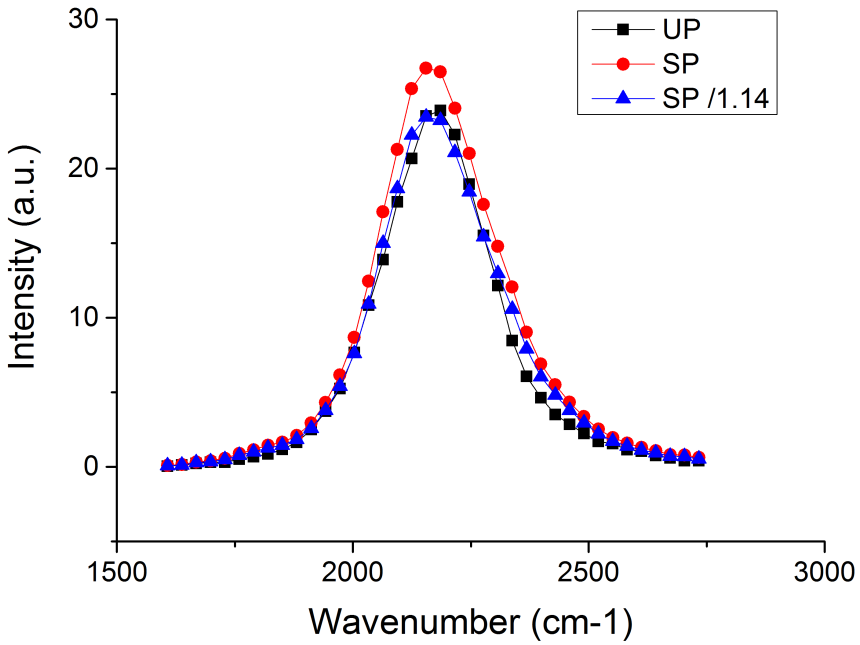

Figure 5.8: The predicted spectrum inside the MCT-layer of PCC793-4, when dividing the experimentally obtained spectra from the patterned (SP) and unpatterned (UP) area by their respective FDTD-simulated LEE.

The integrated intensity from the spectra measured at 11 K at different points on both of the samples can be seen in Figure 5.9. As both samples have a varying quality of the surface pattern, visible in Figure 5.5, A.4 and A.5, the integrated intensity increases when moving across the patterned area towards the center of the sample. The narrow plateau of the patterned area was used

to find the enhancement in light emission due to the surface pattern, which was 100 % for PCC793-3 and 163 % for PCC793-4 at 11 K. At 140 K, the qualitative features are similar as at 11 K for the integrated intensity, but the enhancement is reduced to respectively 48 % and 74 %.

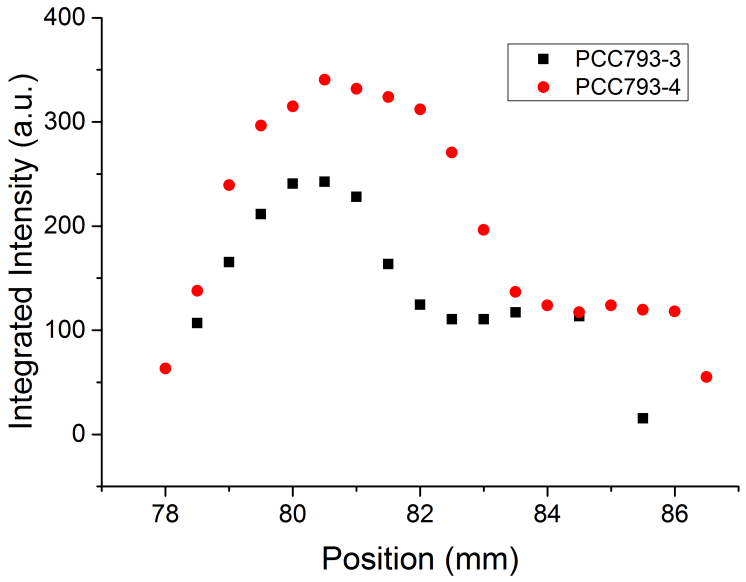

Figure 5.9: Integrated intensity at different positions of PCC793-3 and PCC793-4 measured at 11 K.

The FDTD-simulation of these samples were performed with its material properties at 140 K. The enhancement in light emission was calculated to be 41 % for PCC793-4 and 31 % for PCC793-3, which is lower than the measured values.

5.1.3 PCC794

Three samples, PCC794-1, PCC794-3 and PCC794-4, come from the same MBE-grown structure, where the active layer is a thin film. This structure contains a DBR, consisting of four alternating layers of CdTe and MCT with $x \approx 0.6$. A cross-section of the layers can be seen in Figure 5.10. These samples are designed to make several comparisons on how sample parameters affect the enhancement in light emission: PCC794-1 and PCC794-4 for different grating periods, PCC794-1 and PCC794-3 for different fill factors,

and PCC794-1 and PCC793-4 to see the effect of the DBR.

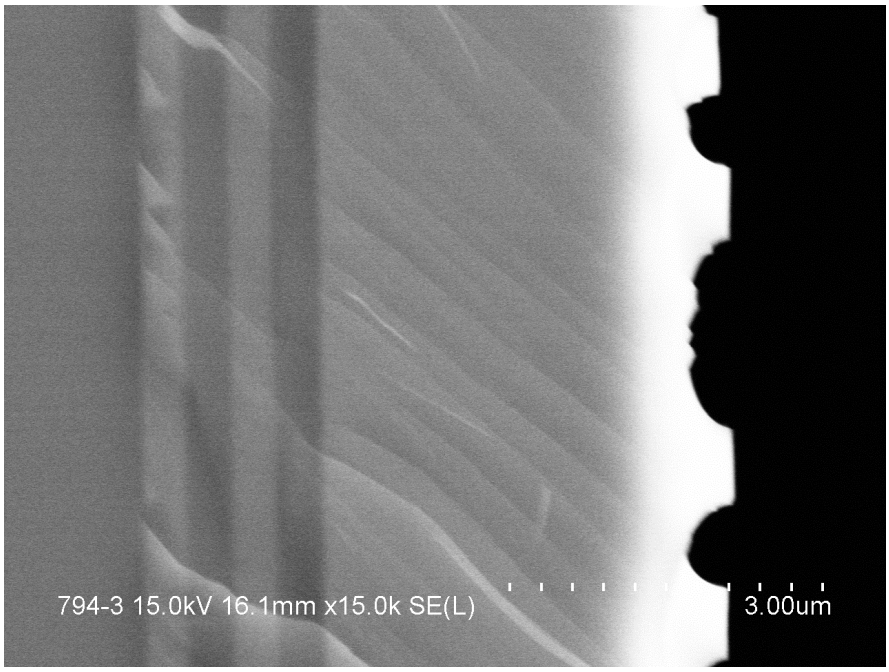

Figure 5.10: Image obtained by a scanning electron microscope (SEM) showing the different layers of the sample. The cross section is not cut through the middle of the holes, and the depth of the holes showed is therefore not the maximum depth.

All of the three samples show uniform surface patterns where both the size and the depth of the holes are not varying to a large extent across the patterned area. In addition, the height profile of the holes are as for the other samples not fully cylindrical. More details about the surface pattern are given in appendix A.4-A.6.

As the PL-intensity from PCC794 was very weak at 11 K, measurements were performed at 140 K, where the intensity had increased to a sufficient level. The spectra at this temperature contained more than one peak, and the sample emitted light over a relatively broad range of wavelengths, covering $\frac{a}{\lambda}$-values of 0.63 to 1.21. It is therefore hard to give a precise value of the normalised grating period, and a value showing the central wavelength of the overlapping peaks in the spectra is therefore used. Figure 5.11 shows spectra from PCC794-1. The other two samples had spectra that were quantitatively similar, as shown in appendix A.5 and A.6.

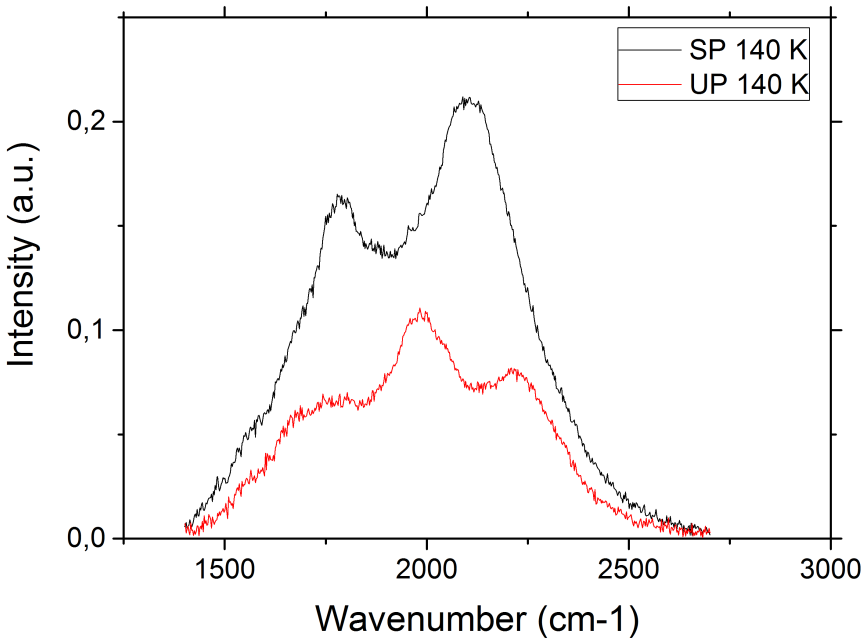

Figure 5.11: Spectra obtained from the patterned (SP) and unpatterned (UP) area of PCC794-1 at 140 K.

Unlike the spectra from the patterned area, having two distinct peaks, the spectra from the unpatterned areas of the three samples have three peaks. If all of these three peaks were originating from the material properties, this would mean that the acceptor levels in the band gap of the active MCT-layer differ in the patterned and unpatterned areas of the sample. As this is highly unlikely, it is of higher probability that the last peak, which can be seen at about 2000 cm^{-1} at both temperatures, is due to an optical effect. This was investigated by doing transfer-matrix method simulations of the unpatterned area, seeing how the LEE of the structure depended on the wavelength. When dividing a spectrum obtained from the unpatterned area of the sample by the simulated wavelength-dependent LEE, the peak at 2000 cm^{-1} disappeared. This is shown in Figure 5.12, and indicates that the this peak most likely is due to an optical effect, and not an intrinsic material property.

The results from the transfer matrix simulations is supported by the 3D FDTD-simulations. By dividing each of the spectra in Figure 5.11 by their

respective FDTD-simulated LEE, the spectra plotted in Figure 5.13 are obtained. These spectra will then predict the PL-spectrum of the source inside the sample. Apart from a multiplication factor of 1.6, these spectra are nearly identical; which is rather convincing evidence that the spectrum originating inside the MCT layer does indeed look like the ones in Figure 5.13. This confirms that the peak at 2000 cm^{-1} from the unpatterned area is an optical effect, and additionally shows that the FDTD simulations work very well, apart from a multiplication factor, as was also shown for PCC793-4.

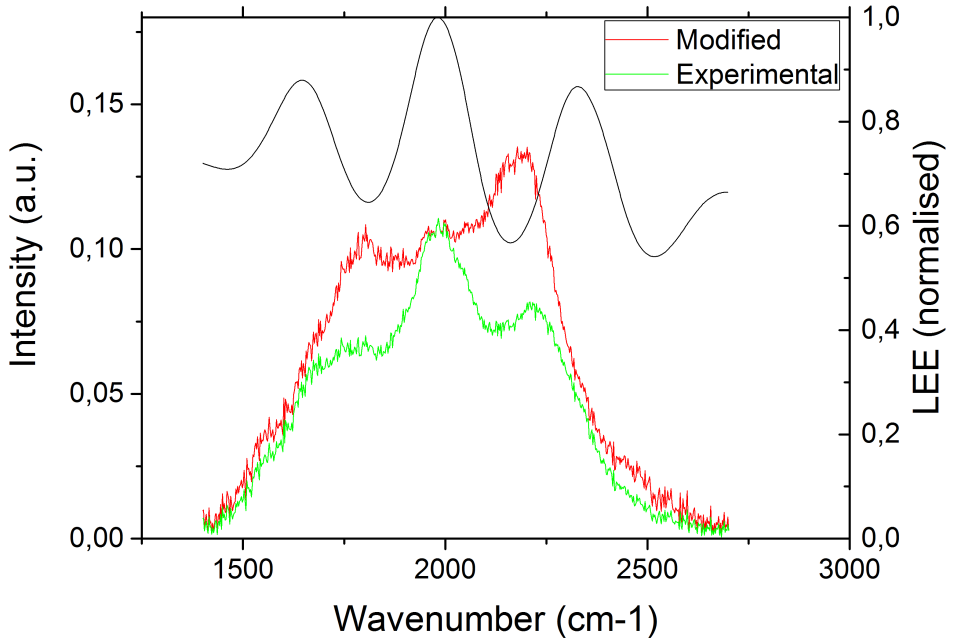

Figure 5.12: Spectra showing the optical effect giving the third peak. The black line is the wavenumber-dependent LEE of the structure simulated by transfer matrices, the green is the measured spectrum, and the red is the measured spectrum divided by the LEE.

The predicted spectrum inside the MCT-layer of PCC794-1, given in Figure 5.13, shows two distinct peaks, separated by about 320 cm^{-1}, or 40 meV. This is most likely due to an impurity or defect in the active MCT layer, which has introduced an acceptor level in the energy band diagram of the material. This will be discussed more in section 5.5. The high-energy peak is the band-to-band transition, while the low-energy peak is due to the introduced acceptor level.

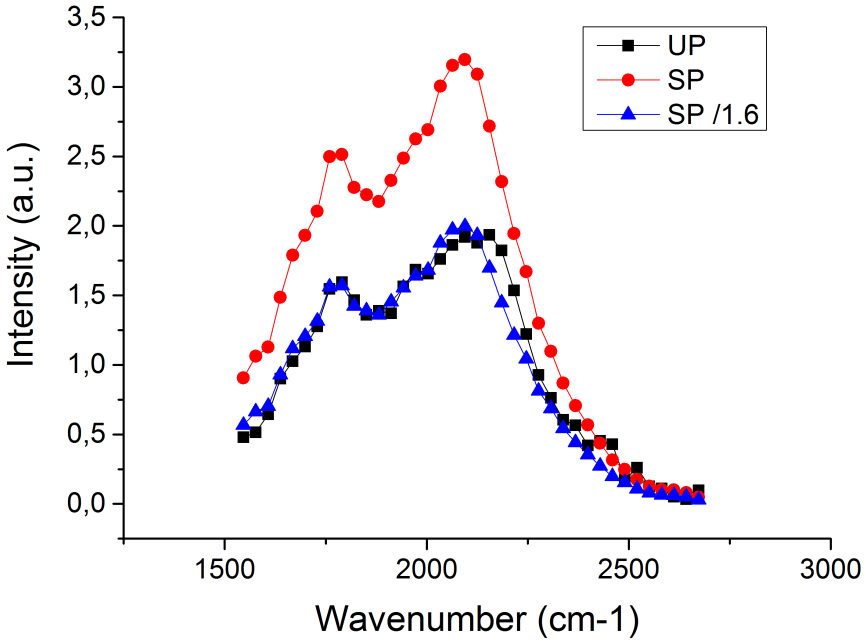

Figure 5.13: The predicted spectrum inside the MCT-layer of PCC794-1, when dividing the experimentally obtained spectra from the patterned (SP) and unpatterned (UP) area by their respective FDTD-simulated LEE.

Figure 5.14 gives the integrated intensity measured at different positions on the samples. By using the two plateaus evident for all samples, the enhancement in light emission is calculated to be 92 % for PCC794-1, 52 % for PCC794-3 and 123 % for PCC794-4. The relatively flat plateaus for the patterned areas are also in correlation with the relatively uniform surface pattern of the samples.

The FDTD-simulations of these samples were performed with their material properties at 140 K. The enhancement in light emission was then calculated to be 31 % for PCC794-1, 5 % for PCC794-3, and 46 % for PCC794-4, which is lower than the measured values. However, it ranks the three samples qualitatively correct.

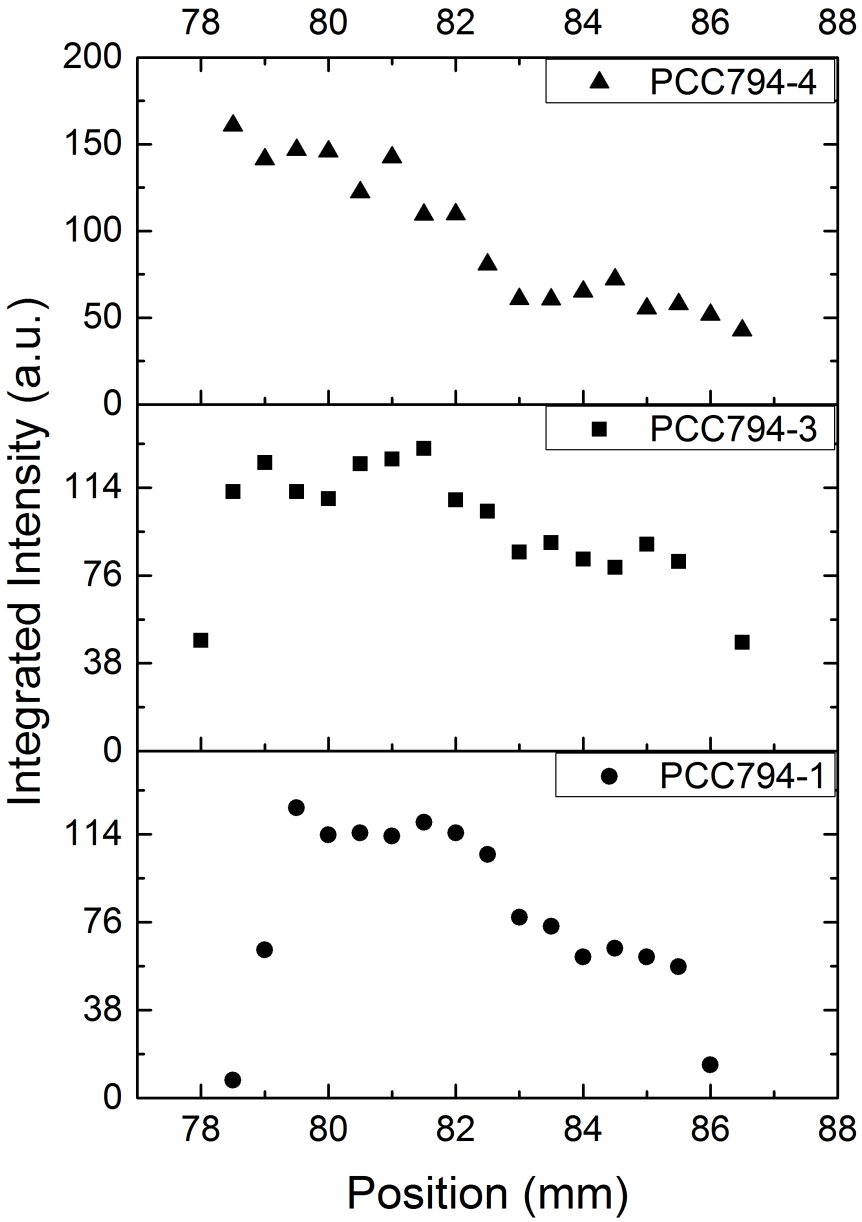

Figure 5.14: Integrated intensity at different positions of PCC794-1, PCC794-3 and PCC794-4.

5.2 Comparison of the samples

5.2.1 Grating period

The normalised grating period, $\frac{a}{\lambda}$, is an important parameter of the surface pattern. This can be illustrated by the fact that when seeing the pattern as a diffraction grating, the normalised grating period gives the incidence angles for the different diffraction orders. This is shown in (2.9), and a change in $\frac{a}{\lambda}$ might then move the incidence angle of a given diffraction order from outside to inside the escape cone. The 2D FDTD-simulations used in my project assignment [1], Figure 5.15, tell that the enhancement increases when increasing $\frac{a}{\lambda}$, until reaching a value of around 0.6, where it starts to decrease. This differs somewhat from the similar simulations by Ichikawa and Baba [10] for an LED with a GaInAsP active layer, where the enhancement began at $\frac{a}{\lambda}$ equal to 0.259, then increased until 0.516, before reaching a relatively stable level, instead of decreasing. However, their experimental results resembled something in between the two, as it reaches a maximum at $\frac{a}{\lambda}$ approximately equal to 1 before decreasing slowly.

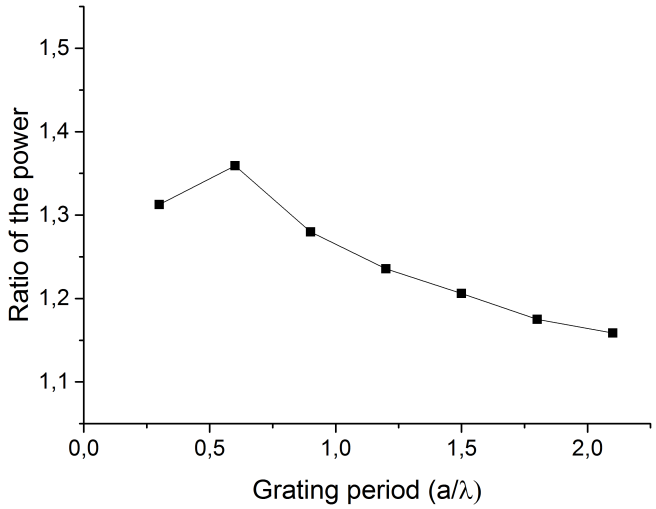

Figure 5.15: The simulated ratio of the power from the processed and unprocessed area of a sample without a DBR. The simulations were performed by the 2D FDTD-method [1]. The wavelength of the emitted radiation was 4.426 μm, and the fill factor 0.5.

Two samples used to compare different grating periods experimentally are PCC752-3 and PCC793-3, where the first one has a normalised grating period of 1.61 and the latter 0.80 at 11 K. The sample with a normalised grating period of 0.80 showed an enhancement of 100 %, while the one with a higher $\frac{a}{\lambda}$ only showed 55 % enhancement, indicating that a normalised grating period of 0.80 gives a higher enhancement than 1.61. This is qualitatively in good agreement with the 2D FDTD-simulations shown in Figure 5.15. Both of these samples were also simulated by 3D FDTD, but at different temperatures. As the simulation of PCC793-3 was performed at 140 K, instead of 11 K, the simulated wavelengths are different, also changing $\frac{a}{\lambda}$. A direct comparison of the simulated enhancement for the two samples can therefore not be performed. However, the 3D FDTD-simulations are used in a different manner in the end of this section to see how the LEE changes with $\frac{a}{\lambda}$, and the comparison between these two samples will be further commented there.

Also PCC794-1 and PCC794-4 can be used to compare different values of $\frac{a}{\lambda}$ experimentally. In this case, $\frac{a}{\lambda}$ is respectively 0.97 and 1.26 at 140 K. The experimental results show that at 140 K, a normalised grating period of 1.26 gave an enhancement of 123 %, compared to 92 % at 0.97. The 3D FDTD-simulations of these two individual samples resulted in a lower enhancement for both samples, being respectively 46 % and 31 %. The low simulated enhancement will be discussed in section 5.4, but they still show PCC794-4 having a higher enhancement than PCC794-1. The simulations also show a simular ratio of the two enhancements, which is $\frac{1.92}{2.23} = 0.86$ experimentally and $\frac{1.31}{1.46} = 0.9$ by simulations. In additon, it should be mentioned that the two samples have a different fill factor. FDTD-simulations were therefore performed for the two samples when having the same fill factor. These simulations showed that the samples then had the same enhancement, indicating that the difference in the measured enhancement in light emission might be due to the fill factor, and that the normalised grating periods themselves give similar enhancements.

In order to investigate how the grating period affected the LEE, the 3D FDTD simulations of all the samples were used. As a Gaussian time-modulated point source was used, the LEE was simulated for several wavelengths at once for each sample. By comparing the observed power in the plane of observation above the surface of the structure with the emitted power from the source itself, the extraction efficiency for every wavelength could be found. This could then be further used to see the dependence of the extraction efficiency on $\frac{a}{\lambda}$. This is plotted in Figure 5.16, and shows that

the dependence on $\frac{a}{\lambda}$ varies for each individual sample. The oscillations visible are most likely due to interference from the thicknesses of the different layers, and it is hard to draw any conclusions for normalised grating periods between 0.8 and 1.4, as there are large variations from sample to sample. However, the enhancement does seem to be quite stable for these normalised grating periods, when smoothening out the oscillations. For normalised grating periods larger than 1.4, however, PCC752-3 indicates a decrease in the enhancement for increasing grating periods. The relatively stable enhancement between 0.8 and 1.4 makes the 3D FDTD simulations differ from the 2D simulations seen in Figure 5.15, and are more resembling to the trend found by Ichikawa and Baba [10], where there is a stable enhancement for a range of normalised grating periods around the maximum, and decreasing outside this range.

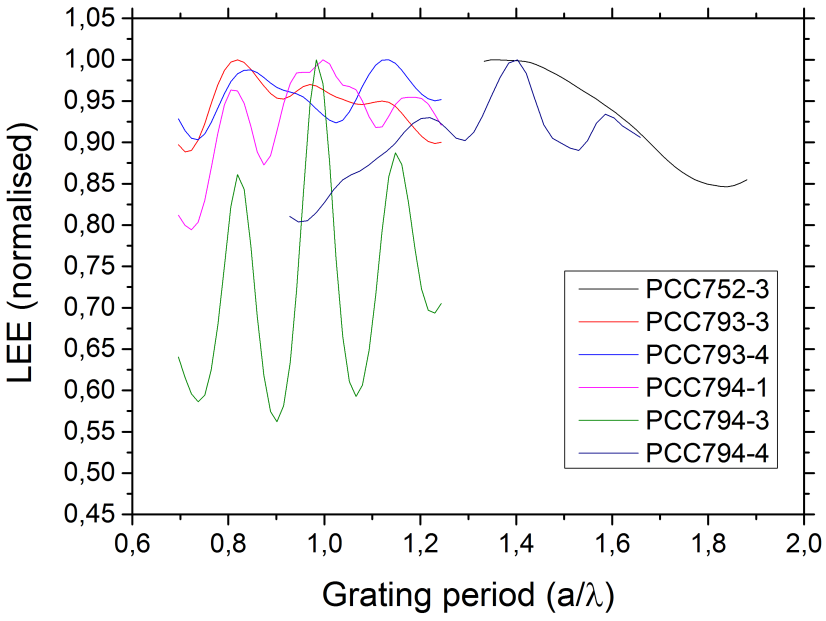

Figure 5.16: The simulated normalised extraction efficiency for each sample. The extraction efficiency is normalised to the maximum extraction efficiency within the plotted interval for each individual sample. The normalised values are used to avoid offsets for the individual samples due to other factors than the grating period, such as the presence of a DBR.

From the experimental and simulation results, it can be concluded that a grating period of 0.8 is better than 1.61, as both the experiments and simu-

lations showed this trend. The experiments showed that a grating period of 1.26 gives a larger enhancement than 0.97, but simulations of the two samples concerned revealed that this difference might be due to the different fill factors of the samples instead of the grating period. Figure 5.16 supports this theory, as it shows that these two normalised grating periods should give a similar LEE.

5.2.2 Thickness of the passivation layer and depth of the holes

The thickness of the passivation layer was shown in [1] to have an effect on the enhancement in light emission, mainly due to the thickness-dependence of the LEE of the unpatterned layer. Changing the thickness could then change the CdTe-layer from an antireflective to a reflective coating. This is shown in Figure 5.17, where a 2D FDTD-simulation has been done to find the calculated power 2 μm above the surface of an unpatterned structure with different thicknesses of the CdTe-layer.

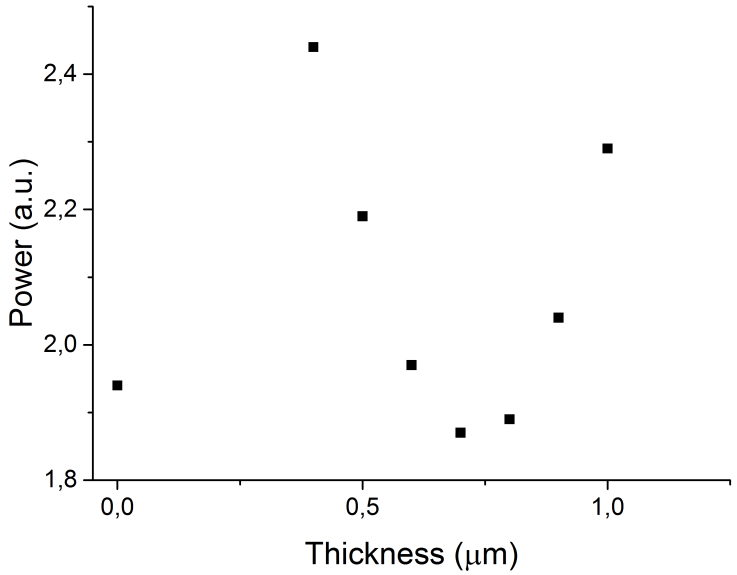

Figure 5.17: 2D FDTD-simulations showing the absolute value of the calculated power for TE polarisation for different thicknesses of an unpatterned CdTe-layer on top of a 4 μm thick active MCT-layer. The wavelength of the emitted light is 5 μm, and the structure does not contain a DBR [1].

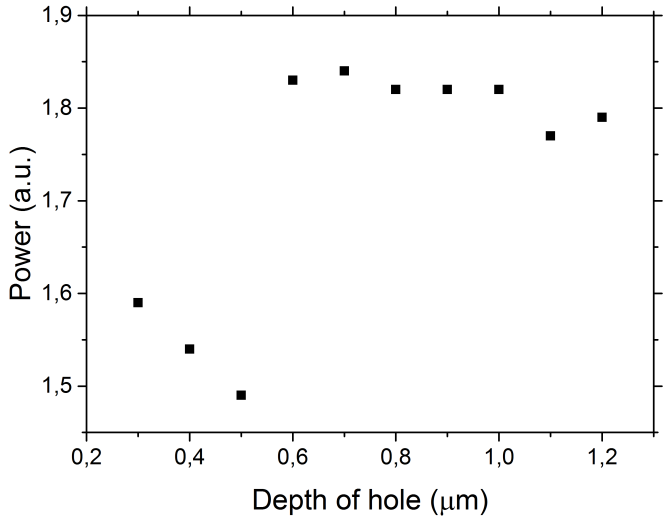

Figure 5.18: Calculated power from the 3D FDTD simulation of a structure without DBR, where the holes are etched all the way through the passivation layer, and the wavelength of the emitted light is 4.6 μm. The thickness of the passivation layer is equal to the depth of the holes.

The thickness of the passivation layer also limits how deep the holes can be etched, as they ideally should be etched down to just above the interface between the CdTe and active MCT. This will affect the enhancement in light emission, as the LEE of the patterned area of the sample will depend on the depth of the holes, both when the holes are etched all the way to the interface, Figure 5.18, and when not etched through the CdTe-layer, Figure 5.19.

Figure 5.19 shows a fast decline in the calculated power when the holes are not etched all the way through the passivation layer. In the study by Tonheim et.al. [2], the holes on one of the samples were only etched about 300 nm deep in a 490 nm thick passivation layer. 3D FDTD-simulations showed that by simply etching all the way through the passivation layer, this could increase the enhancement in light emission by 14 %, from the 35 % obtained in the study to about 54 %. This was tested by PL-measurements of PCC752-3, which showed an enhancement in light emission of 55 %, which is in good agreement with what was simulated.

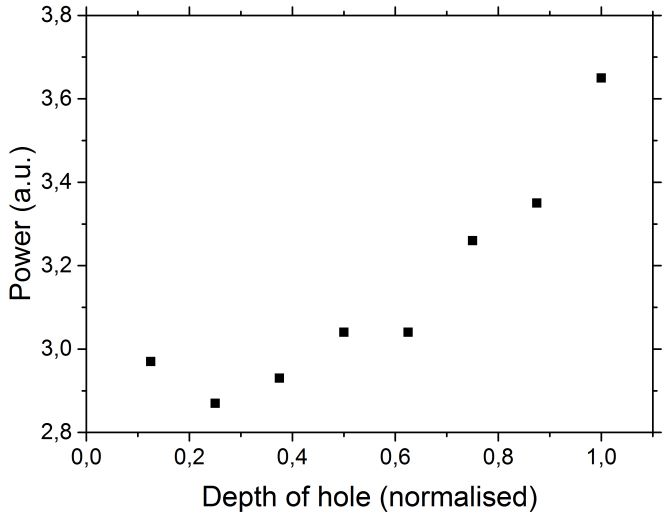

Figure 5.19: Calculated power from the 3D FDTD simulation of a structure with a DBR, where the holes are etched only partly through a 0.8 μm thick passivation layer, and the wavelength of the emitted light is 4.6 μm. The x-axis is normalised to the thickness of the passivation layer.

Two samples used to study both the thickness of the passivation layer, and the depth of the holes, are PCC793-3 and PCC793-4. The latter of the two samples has both a thicker passivation layer and deeper holes, as shown in Table 5.1. In addition, the holes of PCC793-3 are only etched through 85 % of the passivation layer, unlike the ones of PCC793-4, which are etched all the way through. At 11 K, the enhancement in light emission was measured to be 163 % for PCC793-4 and 100 % for PCC793-3, while measurements at 140 K gave enhancements of 74 % and 48 %. This is qualitatively in good agreement with Figure 5.19, as the holes ethched through the passivation layer should give the highest enhancement.

The question is then how much of the increase in the enhancement in light emission is due to the depth of the holes, and how much can be related to the thickness of the passivation layer, affecting the LEE of the unpatterned area? Figure 5.20 shows the relevant spectra at 140 K, indicating that most of the difference in the enhancement is due to the depth of the holes, as the spectra from the unpatterned areas show similar intensity. However, the absolute intensity might, as mentioned in section 3.4, vary due to the sample position during the PL-measurement, and FDTD-simulations should be taken into

consideration before the conclusions are drawn.

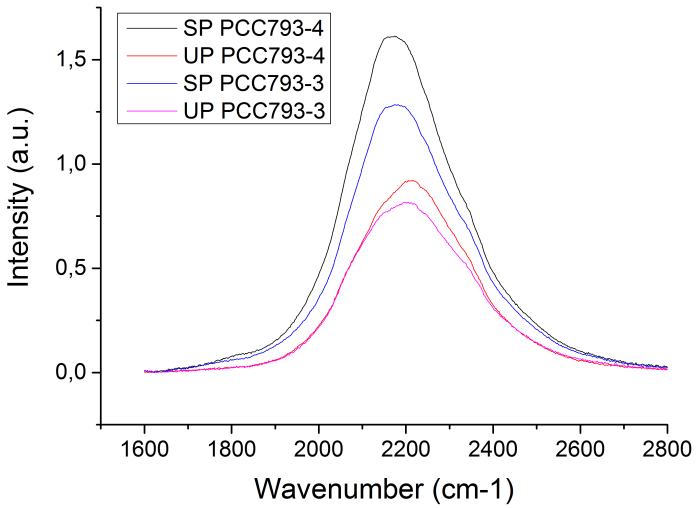

Figure 5.20: Spectra obtained for PCC793-3 and PCC793-4 at 140 K.

In order to find the isolated increase in enhancement due to the holes, Figure 5.19 can be used. It shows that about 11 % more of the generated light will be emitted from the sample with holes etched all the way through the passivation layer, than a sample where only 85 % of the thickness is etched, which is the case for PCC793-3.

3D FDTD-simulations show that the unpatterned area of PCC793-3 has a 2 % higher LEE than the unpatterned area of PCC793-4. This is opposite of what was seen in Figure 5.20, and might indicate that some of the differences seen in absolute intensity in the spectra are not due to the LEE, but small differences in the experimental setup. However, both the experiments and the simulations show that the majority of the difference in the enhancement is due to the depth of the holes.

When it comes to the simulated differences compared to the measured differences in enhancement in light emission, the comparison can be done at 140 K, for which the simulations were performed. By using the experimentally obtained enhancement of PCC793-3, we denote the intensity from the unpatterned area of the sample 1, and the from the patterned area of the sample 1.48, giving the measured enhancement of 48 %. The depth of the

holes should then increase the LEE of the patterned area of PCC793-4 by 11 % compared to PCC793-3, giving it an intensity of 1.643. The decrease in LEE of the unpatterned area reduces the intensity from 1 to 0.98 for the unpatterned area of PCC793-4. The simulations then give an enhancement of 66 % for PCC793-4, which is lower than the 74 % found by the means of PL, but still a fairly reasonable estimate. For better illustration, these calculations are also shown in Table 5.3.

Table 5.3: Calculated enhancement in light emission for PCC793-4 according to the FDTD-simulations when the experimental results from PCC793-3 are used as a starting point.

	140 K	
	PCC793-3	PCC793-4
Surface Pattern	1.643	1.48
Unpatterned	0.98	1
Enhancement	66 %	48 %

Figure 5.17-5.19 show that in general, both the thickness of the passivation layer and the depth of the holes affect the enhancement in light emission. When the emitted wavelengths are about 4.6 μm, the holes should be at least 600 nm deep, and etched all the way through the passivation layer. In the special case of PCC793-3 and PCC793-4, the effect seems to be larger for the depth of the holes than the thickness of the passivation layer. For samples with other differences in the thickness and depth, however, the situation might be different.

5.2.3 Fill factor

2D FDTD-simulations for optimisation of the parameters of the surface pattern [1] showed that the fill factor could alter the enhancement in light emission, although not being as critical as for instance the normalised grating period. Due to challenges during the processing of the surface pattern, the hole size turned out to be tricky to control in a precise manner, and a broad range of fill factors were therefore not processed. The reason behind this is that in order to control the fill factor and obtain a uniform surface pattern, the sample surface should be as flat as possible and the thickness of the photoresist should be uniform across the sample. Due to surface tension, however, the photoresist was thicker at the edges of the surface. Combined with defects on the sample making the surface rough, this made the thickness of the photoresist vary throughout the surface. Because of this, not

all parts of the surface were in contact with the mask when the exposure was done, causing variations in the hole size, and also leaving photoresist in the bottom of the holes in areas with thicker photoresist after development. The consequence of these problems is that the surface pattern could not be made completely uniform, and that especially the fill factor was depending on the location on the sample. Although the fill factor was not processed as precisely as wanted, it is still possible to draw some conclusions about it from the experimental results.

PCC794-1 and PCC794-3 have equal thicknesses of the different layers. The difference between the two is the surface pattern, where the fill factor is 0.32 for PCC794-1, and 0.06 for PCC794-3. The holes of PCC794-1 are in addition also slightly deeper. Table 5.2 shows that the enhancement in light emission is higher for PCC794-1, being 92 % at 140 K, versus 52 % for PCC794-3. This gives an enhancement $\frac{1.92}{1.52} = 26$ % higher for PCC794-1. Although the simulated results from the these two structures show lower enhancement than what was measured, the ratio between the enhancement in light emission for the two samples was simulated to be $\frac{1.31}{1.05} = 25$ %, which is in good agreement with what was seen experimentally.

When discussing the effect of the grating period, it was mentioned that PCC794-4, with a normalised grating period of 1.26 and a fill factor of 0.38, had a higher enhancement in light emission than PCC794-1, having a normalised grating period of 0.97 and fill factor of 0.32. It was then discussed if the entire difference in enhancement could be related to the normalised grating period, or some of the difference could possibly also be explained by the fill factor. An FDTD-simulation, where the normalised grating period of the sample was equal to PCC794-1, and the fill factor equal to the one of PCC794-4 was therefore performed. This showed the same simulated enhancement in light emission as for PCC794-4, and indicates that a major part in the difference in the enhancement in light emission between the two samples is the fill factors, and that a fill factor of 0.38 seems to be better than 0.32 for a sample similar to PCC794-1.

Another sample that could tell something about the enhancement's dependence on the fill factor is PCC793-4. Figure 5.9 showed an increasing enhancement when scanning across the surface pattern towards the center of the sample. This is most likely due to the difference in fill factor, as the AFM-pictures, Figure 5.21, showed a decrease in the fill factor when moving

away from the center of the sample.

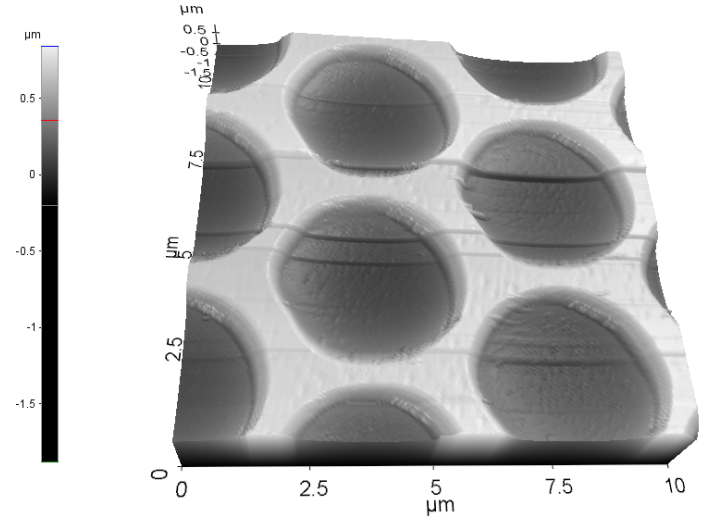

(a)

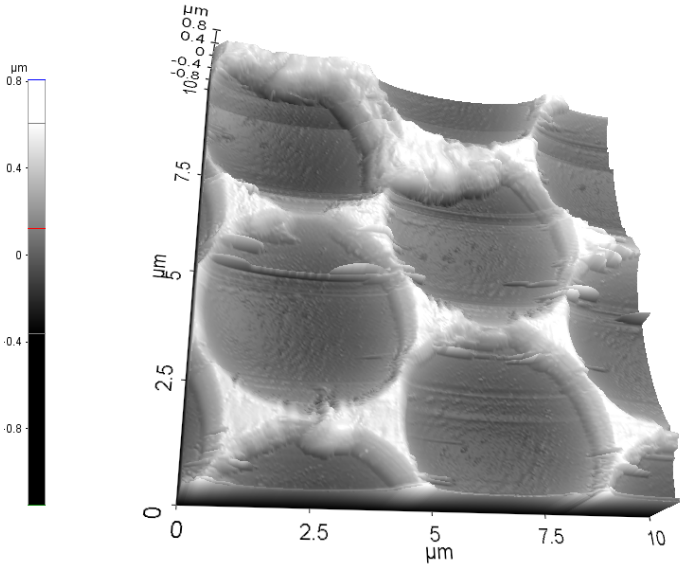

(b)

Figure 5.21: (a) AFM-image showing a representative area of the surface pattern close to the central region of PCC793-4. (b) Representative area of the surface pattern towards the edge of PCC793-4.

5.2.4 Effect of the DBR

The DBR was added to the samples in order to have a reflective backside. The motivation behind this was to increase the LEE of the sample, and simultanously increase the enhancement in light emission. Table 5.2 tells that the highest enhancement was found for a sample without a DBR (PCC793-4) at 11 K, with an enhancement of 163 %. However, at 140 K the enhancement was only 74 % for PCC793-4, and both PCC794-1 and PCC794-4, which are samples with a DBR, showed a higher enhancement. As these two samples were not measured by PL at 11 K due to low absolute intensity, it is therefore uncertain if the enhancement would had been higher than 163 % at 11 K. Section 5.3 shows that the enhancement increases significantly for all samples when the temperature is decreasing, making it plausible that the samples with a DBR could had shown a larger enhancement than the ones without also at 11 K. Further investigations are therefore still necessary in order to conclude if samples with a DBR give the highest enhancement at all temperatures. This study indicates that this might be the case, as the two best samples at a temperature where both samples with and without a DBR were measured, had a DBR. In addition, this indication is supported by PL-measurements performed on a sample with a DBR not included in this study due to low PL-intensity. Measurements were performed at 11 K for this sample, but due to the low PL-intensity, poor statistics were obtained. From these poor statistics, the enhancement in light emission was calculated to be 206 %, which supports the indication that the enhancement for a sample with a DBR might be larger than the ones without also at 11 K.

To compare the PL-measurements between a sample with and without a DBR, PCC793-4 and PCC794-1 are used. Both of these have been measured by PL at 140 K, and have similar thicknesses of the active and passivation layer, together with a similar surface pattern and x-value of the active layer. The PL-spectra from the patterned area of the two samples are shown in Figure 5.22, and show remarkable differences. The most obvious one is the shape, as the spectrum from the sample with a DBR (PCC794-1) shows two peaks. This is on the other hand not present in the structure without a DBR (PCC793-4), and indicates differences in the intrinsic material properties for the two structures. As this additional peak only has been seen for samples with a DBR, it might indicate that the DBR is the cause. This leads to a broad range of wavelengths being emitted from the sample with a DBR, which can be detrimental for certain application, if for instance a narrow-band of emitted wavelengths is needed.

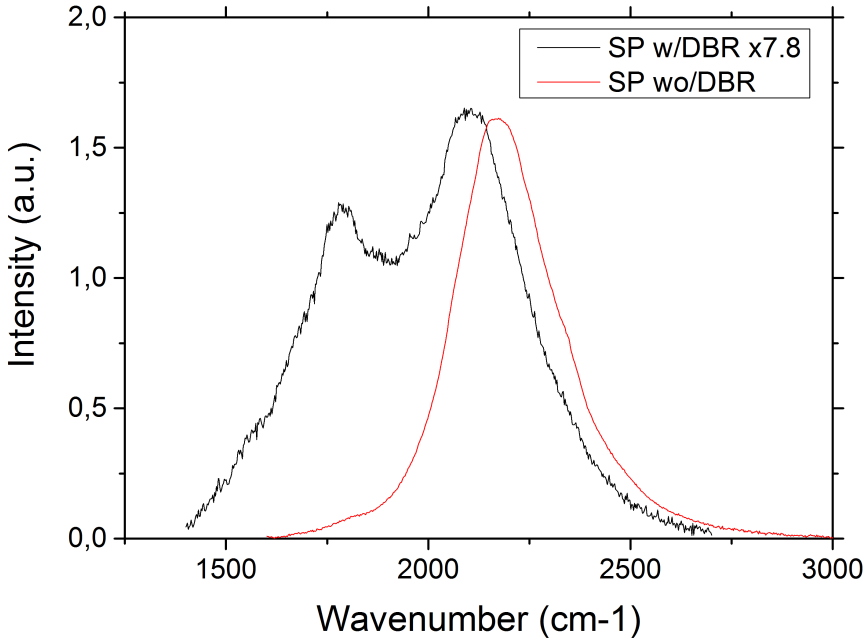

Figure 5.22: Comparison of the spectrum from the patterned (SP) area of a sample with and without a DBR. Due to lower absolute intensity from the sample with a DBR, the intensity has been multiplied by 7.8 to illustrate the differences in the shapes of the spectra. The reason behind the slight difference in the peak position is most likely due to a small variation in the x-value of the samples.

When adding the spectra from the unpatterned area of the samples, another difference in the shape is evident, visible in Figure 5.23. As explained in section 5.1.3, the spectrum from the unpatterned area of the sample with a DBR has an extra peak, not present in the spectrum of the patterned area. This was shown to be due to an optical effect, as the LEE is significantly higher in the wavelength interval where the peak appears, than at the other wavelengths present in the spectrum. For a sample without a DBR, the variations in the LEE for the different wavelengths is not as significant, and extra peaks do not appear, as Figure 5.23 and 5.24 show.

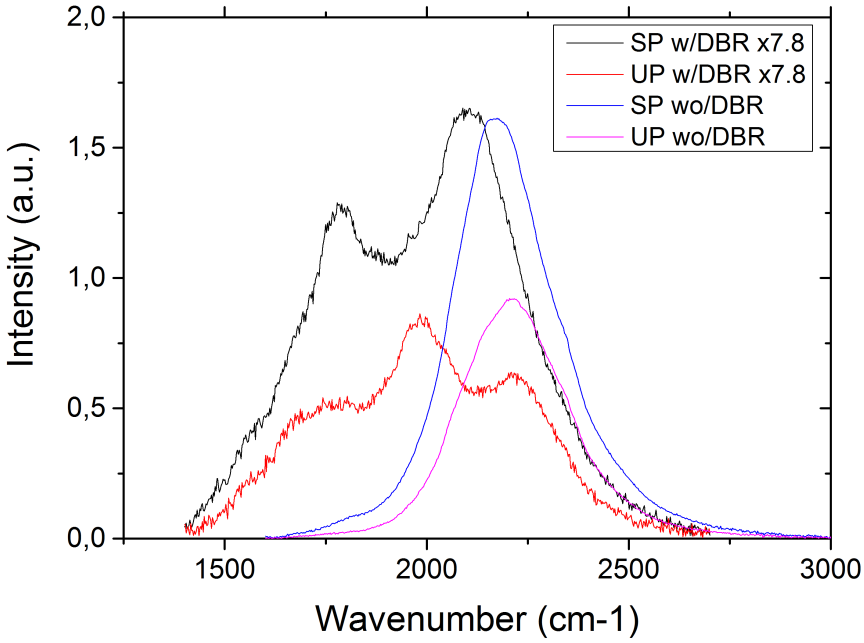

Figure 5.23: Comparison of the spectrum from the patterned (SP) and unpatterned (UP) area of a sample with and without a DBR. Due to lower absolute intensity from the sample with a DBR, the intensity has been multiplied by 7.8 to illustrate the differences in the shapes of the spectra.

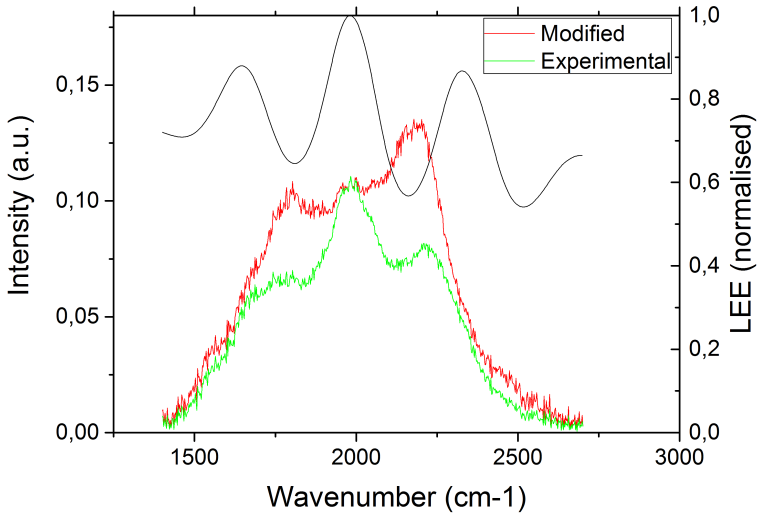

(a) The spectrum from a PL-measurements of the unpatterned area of a sample with a DBR. The black line shows the simulated LEE (normalised). The modified spectrum is the experimental spectrum divided by the LEE.

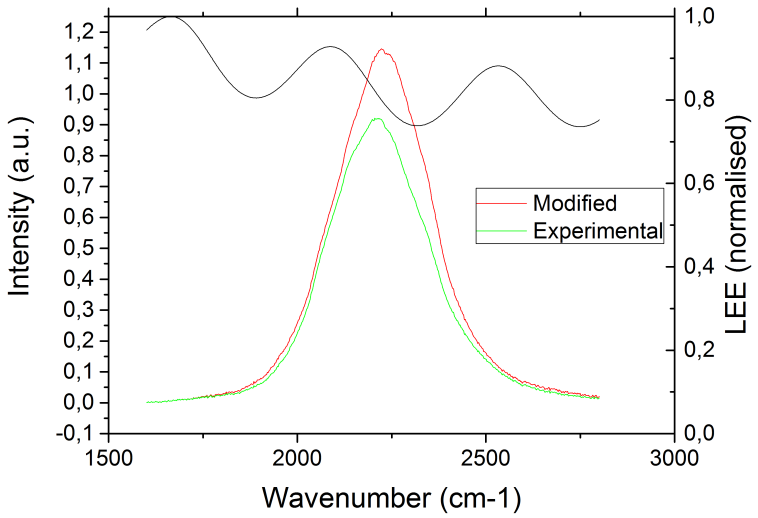

(b) The spectrum from a PL-measurements of the unpatterned area of a sample without a DBR. The black line shows the simulated LEE (normalised). The modified spectrum is the experimental spectrum divided by the LEE.

Figure 5.24: The spectra from the unpatterned area of a sample with and without a DBR, together with the modified spectra, where the experimentally obtained spectra have been divided by the wavelength-dependent LEE.

Although the DBR clearly has an effect on the LEE of the unpatterned area, the relation to the LEE of the patterned area is not as clear. In Figure 5.23, a peak about 2000 cm^{-1} is not seen for the spectrum from the patterned area of a sample with a DBR, as for the unpatterned area. This indicates that the same optical effect is not present in the patterned area due to the surface pattern. The reason for this is most likely that the surface pattern has destroyed the smooth surface, which was necessary to obtain the constructive interference at 2000 cm^{-1} giving the additional peak. Although this peak is not visible in the spectrum of the patterned area, the DBR still most likely has a positive effect on the LEE, as the reflectivity of the backside has been increased, and a larger fraction of the generated light then has the chance to get transmitted out of the structure.

When considering the absolute intensity, Figure 5.22 and 5.23 show that this is higher for the sample without a DBR than the one with. However, in section 5.5, it is shown that low absolute intensity has been seen both for samples with and without a DBR. If the DBR is the cause of the difference in absolute intensity for PCC793-4 and PCC794-1 is therefore uncertain, and further investigations is recommended to find the underlying cause of the low PL-intensity and whether the DBR is to blame.

Although the experiments have not given clear results regarding the effect of the DBR on the absolute intensity emitted from the structre, the simulations have shown that the calculated power from the patterned part of PCC794-1 was 7 % higher than for PCC793-4. This shows that a DBR theoretically can have a positive effect on the absolute intensity from a sample. By using the spectra obtained from the simulations of the samples, and normalising them against the spectra of the sources, the LEE at different wavelengths for both the patterned and unpatterned area can be found. This is shown in Figure 5.25. As expected from Figure 5.24, the oscillations in the LEE are much larger for the unpatterned area of PCC794-1 than PCC793-4. It is also visible that the LEE of the patterned area is much more stable across the wavelength range than the one from the unpatterned. This supports the explanations given in the previous paragraph for why an additional peak was not visible at 2000 cm^{-1} for the patterned area of PCC794-1. The dotted lines indicate the average value over the plotted range. The theoretical effect of the DBR for these wavenumbers is then on average an increase of the LEE for both the patterned and unpatterned area of the sample.

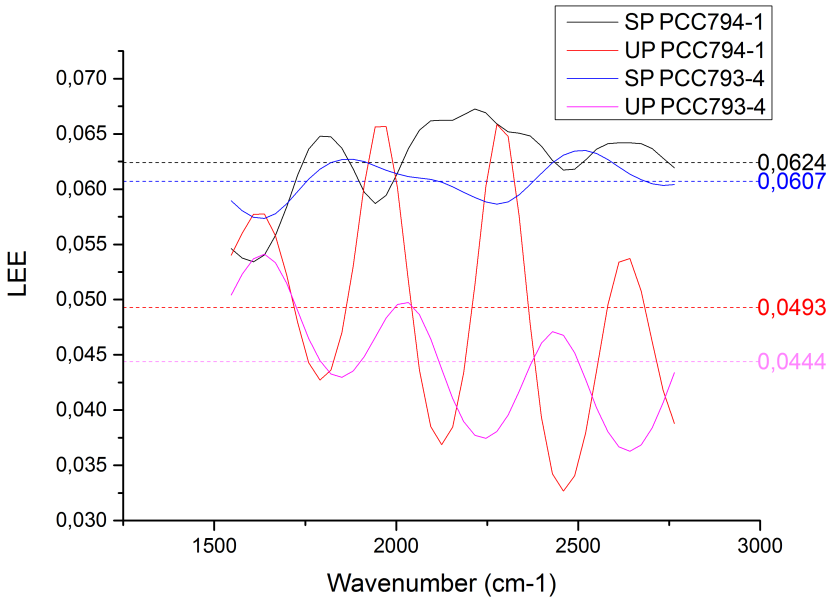

Figure 5.25: The simulated LEE for both the patterned (SP) and unpatterned (UP) area of a sample with (PCC794-1) and without (PCC793-4) a DBR, obtained from 3D FDTD simulations. The dotted lines give the average value of the LEE over the range of wavenumbers simulated.

By using the wavelength-dependent LEE from the unpatterned areas of the sample seen in Figure 5.25, the spectra of the sources in the PL-measurements can also be found. This is shown in Figure 5.26. The sources are obtained by taking the experimentally obtained spectra from the unpatterned area of PCC793-4 and PCC794-1, and divide them by their simulated LEE from the same unpatterned area. Sources with more or less identical shape would had been found if the same procedure was done for the patterned areas of the samples, as shown in Figure 5.8 and 5.13. The sources shown differ in absolute value of the amplitude by about one order of magnitude, which can be explained by the difference in absolute intensity in the measurements. However, it can also be seen that the shape of the spectra is different. For PCC793-4, which does not contain a DBR, the spectrum of the source is symmetric, and only contains one peak. PCC794-1, however, has a source with an unsymmetrical spectrum, that seems to contain two peaks. The simulations then supports what was discussed earlier about the difference in the shape of the spectra from the samples being due to different intrinsic material properties, as the sources of the two samples seem to be different.

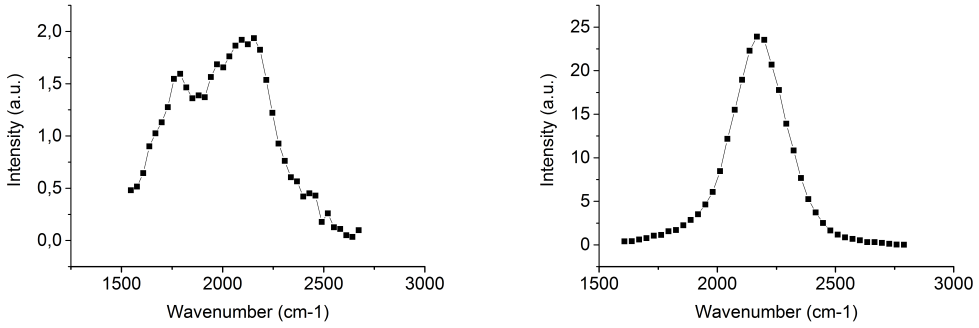

(a) (b)

Figure 5.26: The source of (a) PCC794-1 and (b) PCC793-4. Obtained by dividing the experimentally obtained spectrum from the unpatterned area by the simulated LEE of the unpatterned area.

The obtained experimental and simulated results are ambiguous about the effect of the DBR. At the same measurement temperature, the enhancement in light emission is largest for samples with a DBR, but the absolute intensity is lower. The important part is therefore whether the lower absolute intensity is due to the DBR itself, or some other intrinsic material property, as the simulations showed an increase in LEE for the sample with a DBR. In addition, might the intrinsic material property in the sample with a DBR giving two peaks in the spectra be dentrimental for certain application. When discussing whether or not to have a DBR in a sample, one should also remember that a DBR adds strict restrictions to the MBE-growth, as the layers has to be a precise thickness to obtain the desired effect. FDTD-simulations of a structure where the layers where only 80 % of the correct thickness, showed a decrease in the emitted power of 15 % compared to a similar structure without DBR.

5.2.5 Directional dependence of enhanced light emission

The PL-measurements were performed with two different sample holders, detecting the emitted PL-radiation from the sample with different exit angles to the surface normal. The reason for this is that the experimental setup limits how much of the emitted intensity can be detected. Due to a distance

of a few centimeters between the sample surface and the collection mirror, the collection mirror only covers ±18.6° around the surface normal. Because of this, a large amount of the emitted photons are not detected when PL is performed. It was therefore tested whether the enhancement in light emission would differ when detecting light with different exit angles from the surface. Sample holder A was flat, and thereby covered ±18.6° degree around the surface normal, while sample holder B was tilted 21°.

The three samples PCC752-3, PCC793-4 and PCC794-3 were measured with both of the sample holders. The effect of the exit angle was then tested for both samples with and without a DBR, and for both thin film and MQW samples. The spectra from measurements with both of the sample holders are shown in Figure 5.27-5.29. From these spectra, there seems to be few differences between the PL-measurements performed with the two sample holders, both when it comes to the shape of the spectra, the absolute intensity and the enhancement in light emission for the samples PCC752-3 and PCC793-4. This is supported by the integrated intensity at the different positions on the sample, also seen in Figure 5.27-5.28. From these graphs, it is hard to separate the two sample holders from one another, which indicates that there is no significant change in the results, although the radiation has been detected from different exit angles. For PCC794-3, on the other hand, the answers are not as clear. The shape of the peaks seem to be similar, but the absolute intensity is different. Due to the difference in absolute intensity, it can not be seen directly from Figure 5.29b whether the enhancement in light emission is similar for the two sample holders. As the two other samples showed equal behavior for the measurements with the two different sample holders, it is expected that the result should be similar for PCC794-3, and the difference in absolute intensity is therefore believed to be due to the experimental setup. The integrated intensity for sample holder B is therefore shifted up by 20 units, giving the two measurements the same absolute intensity. This is shown in Figure 5.30, and shows that the enhancement in light emission also for PCC794-3 is similar for both sample holders.

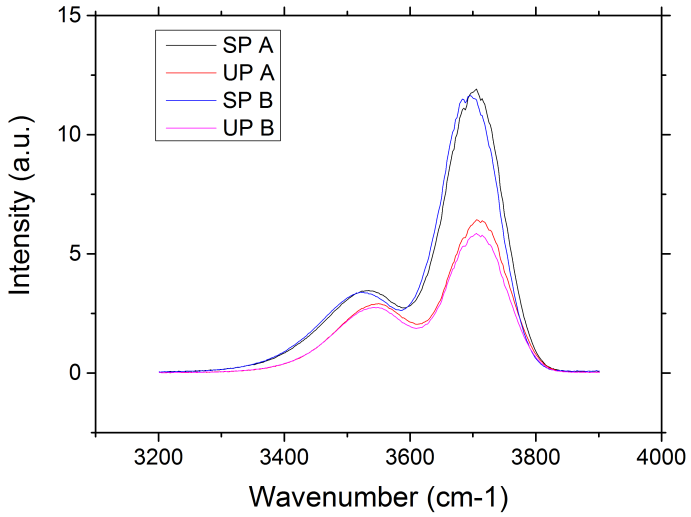

(a) The spectra from PL-measurements of PCC752-3 with the flat (sample holder A) and the tilted (sample holder B) sample holder at 11 K. The patterned area is denoted SP, while the unpatterned is denoted UP.

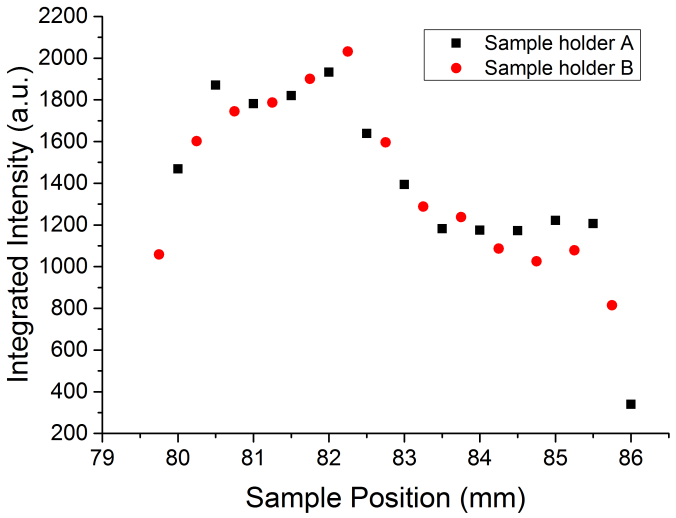

(b) The integrated intensity from different positions on PCC752-3 from PL-measurements done with both sample holders.

Figure 5.27: The spectra and integrated intensity from the PL-measurements performed on PCC752-3 with the two different sample holders.

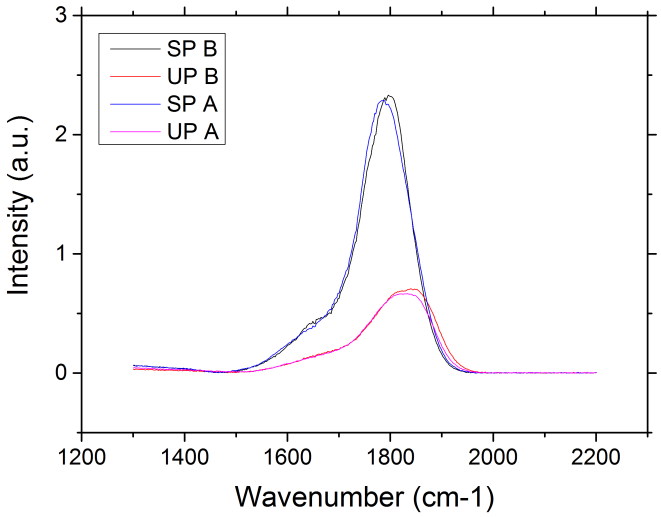

(a) The spectra from PL-measurements of PCC793-4 with the flat (sample holder A) and the tilted (sample holder B) sample holder at 11 K. The patterned area is denoted SP, while the unpatterned is denoted UP.

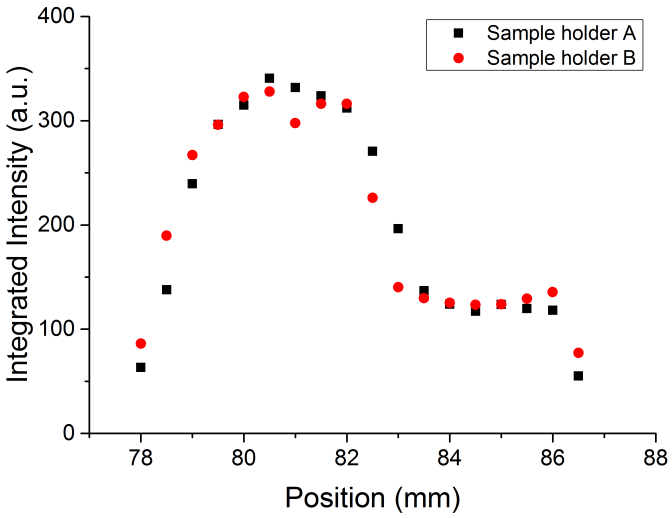

(b) The integrated intensity from different positions on PCC793-4 from PL-measurements done with both sample holders.

Figure 5.28: The spectra and integrated intensity from the PL-measurements performed on PCC793-4 with the two different sample holders.

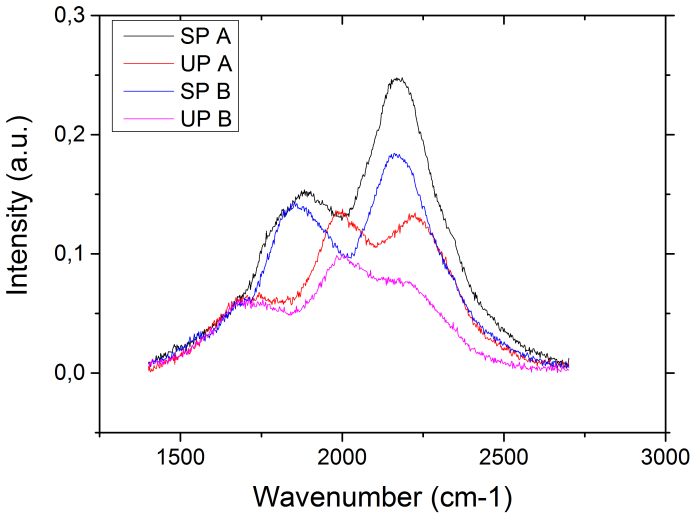

(a) The spectra from PL-measurements of PCC794-3 with the flat (sample holder A) and the tilted (sample holder B) sample holder at 140 K. The patterned area is denoted SP, while the unpatterned is denoted UP.

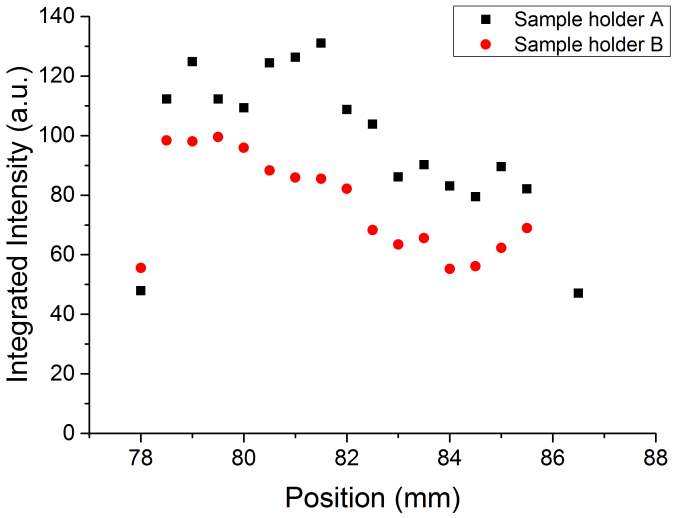

(b) The integrated intensity from different positions on PCC794-3 from PL-measurements done with both sample holders.

Figure 5.29: The spectra and integrated intensity from the PL-measurements performed on PCC794-3 with the two different sample holders.

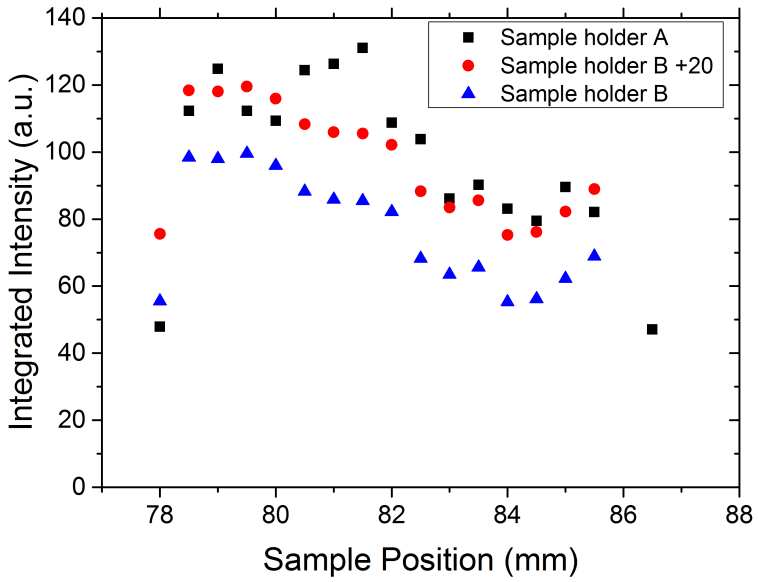

Figure 5.30: The integrated intensity from the PL-measurements of PCC794-3 when the measurement from sample holder B is shifted 20 units upwards.

From these measurements, it can be said that it does not seem to be a large difference in the results obtained with the two different sample holders, and PL-measurements of the direction given by sample holder A is more or less equal to measuring the direction given by sample holder B. This shows that although the collection angle is small in the experimental setup used in this study, the results obtained appear to be similar to what would had been obtained with a larger collection angle. However, as sample holder B only was tilted 21°, a large solid angle has not been investigated, and it can therefore not be concluded that the results obtained will be valid for all other directions.

5.3 Temperature dependence of the enhancement in light emission

In this study, PL-measurements were performed at 11 K, 140 K, and 220 K. Until now, only measurements at the two lowest temperatures have been reported, and details about the spectra of the different samples from measurements at 220 K can be found in appendix A. For all of the samples

in this study, the enhancement decreased when the PL-measurements were performed at a higher temperature, which is shown in Figure 5.31. This is not to be confused with the increase or decrease in absolute intensity for changing temperatures, which will be explained in section 5.5 and has to do with intrinsic material properties of the active MCT layer. Figure 5.31 also shows that the decrease in the enhancement differs for the different samples. When changing the temperature from 140 K to 220 K, PCC793-4 shows for instance a decrease in enhancement from 74 % to 42 %, while PCC794-1 shows a larger decrease from 92 % to 42 %, which makes the enhancement equal for the two samples at 220 K.

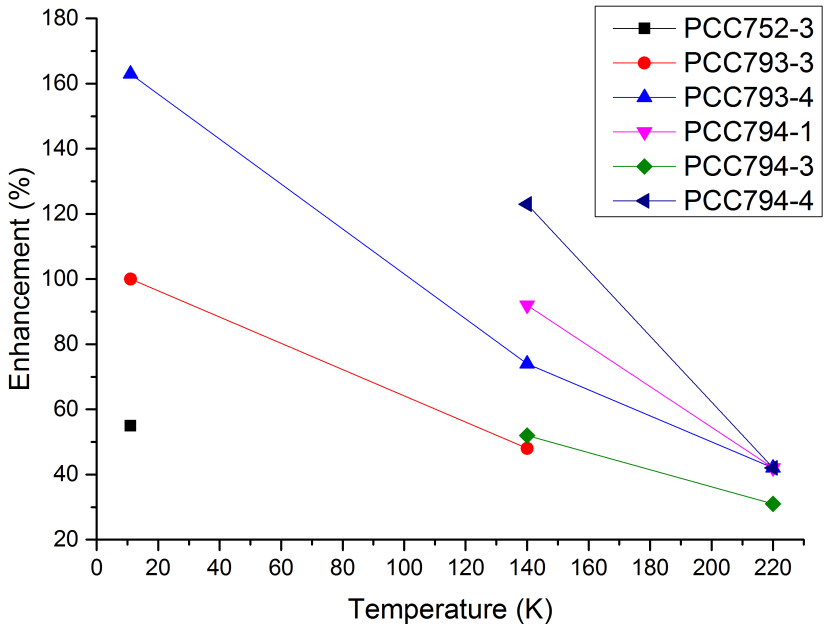

Figure 5.31: The enhancement in light emission for the different samples at 11 K, 140 K and 220 K.

The change in enhancement might be due to the change in the refractive indices and the emitted wavelength. This will change the incidence angle of the diffraction orders, as shown in (2.9), and thereby change when the light is scattered from outside to inside the escape cone. Liu et. al. [47] showed that the refractive index of MCT with an x-value of 0.33 decreased with 0.1 from about 3.46 to 3.36 when changing the temperature from 4.2 K to 300 K. The change was nearly linear, and a change in temperature from 11 K to

220 K then decreases the refractive index of MCT with about 0.07. These changes are in good agreement with the temperature-dependence of the refractive index for $x = 0.289$ seen in Figure 2.8, where only small changes are visible for the same temperature increase. For CdTe [42,43] and CdZnTe [44], the changes in the refractive index will be even smaller. FDTD-simulations were performed with these changes, but showed only small alterations in the enhancement in light emission. The relatively small changes in the refractive indices are therefore most likely not the main reason behind the large change in the enhancement.

Due to the wavelength-dependence of the LEE, as shown in section 5.2.1 and 5.2.4, the change in wavelength will affect the LEE of both the patterned and unpatterned area of the sample, causing a change in the enhancement in light emission. Figure 5.32 and 5.33 show the normalised wavelength-dependent LEE of the unpatterned part of the samples, obtained from transfer-matrix-method simulations, for PCC793-4 and PCC794-1. The spectra at the different temperatures are shown together with the LEE-curve, and show that the variation in the LEE of the structure does not account for the large variations in the enhancement in light emission, as the LEE is quite stable across the wavelength-interval where the spectra are situated for both PCC793 and PCC794. In addition, it can also be seen that none of the spectra only span wavelengths close to a local maximum or minimum of the oscillating LEE, as all of the spectra are wide enough to span both local maxima and minima of the LEE-curve. The change in the emitted intensity from the unpatterned area can therefore most likely not explain the large difference in the enhancement at the different temperatures.

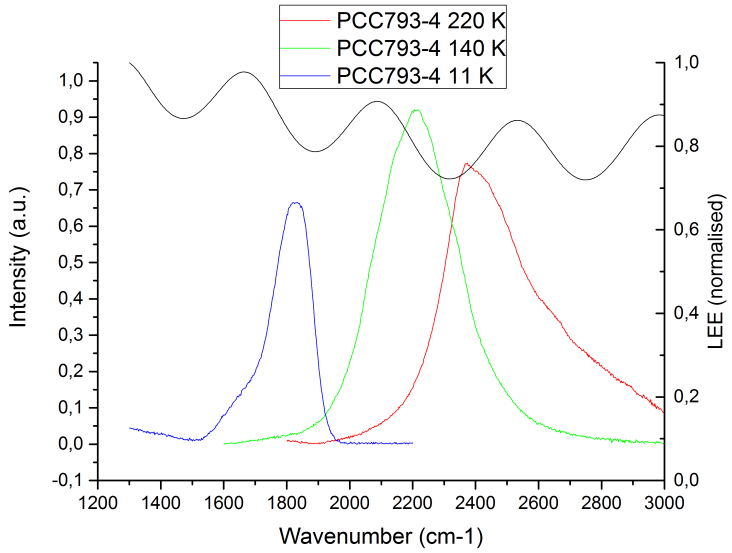

Figure 5.32: The spectra from the unpatterned part of PCC793-4 at 11 K, 140 K and 220 K. The black curve shows the simulated normalised LEE from the unpatterned area of the structure.

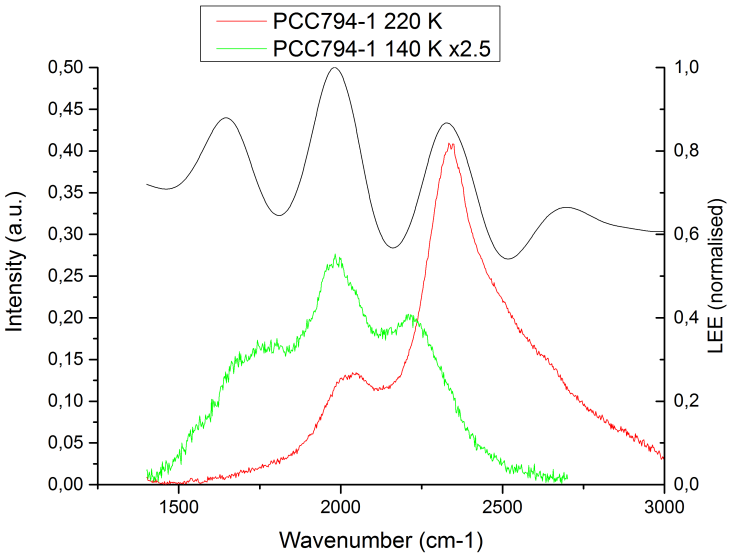

Figure 5.33: The spectra from the unpatterned part of PCC794-1 at 140 K and 220 K. The black curve shows the simulated normalised LEE from the unpatterned area of the structure.

With increasing temperatures, the normalised grating period also increases, due to the decrease of the emitted wavelengths. However, section 5.2.1 showed that only a normalised grating period larger than 1.4 had a clear tendency of decrease in enhancement in light emission for increasing $\frac{a}{\lambda}$. For normalised grating periods around 1, the results showed a dependence on the individual sample, and a relatively stable value. As $\frac{a}{\lambda}$ for PCC793 and PCC794 are between 0.8 and 1.4 at temperatures between 11 K and 220 K, the change in LEE from the patterned area is also not sufficient to explain why the raise in temperature decreases the enhancement to a large extent.

As neither the change in refractive index, nor the change in wavelength could fully explain the decreasing enhancement with increasing temperature, further investigations have to be performed in order to find the underlying cause.

5.4 Validity of the FDTD-simulations

The simulation results presented in Table 5.2 showed that the simulated enhancement in light emission was lower for all samples, except from PCC752-3, than what was measured experimentally. On the other hand, the simulations show the qualitative results in a good way, when similar structures were compared. This can for instance be seen by the fact that for the three samples with a DBR (PCC794), the samples with the highest measured enhancement by PL also showed the highest simulated enhancement. The same can be said about the two samples PCC793-3 and PCC793-4. However, when all of the samples are ranked by their experimentally measured enhancement, the order of the samples is different than when ranked by their simulated enhancement. The question is therefore why the simulated enhancement is lower than the measured enhancement for the majority of the samples, and why the simulations are not in agreement with the experimental results when comparing samples with different structures, such as PCC793 and PCC794?

The answer of the question about the quantitative results might be found by studying some of the simulations that gave fairly accurate quantitative results. When discussing the thickness of the passivation layer and the depth of the holes (section 5.2.2), the simulated differences between PCC793-3 and PCC793-4 were close to the measured values. In this case, the simulations of the unpatterned areas were compared to each other, and the simulations of the patterned areas were compared to each other, but no comparison between

a patterned and unpatterned structure was done. Other simulation results that gave good quantitative results are the ratio of the enhancements of the PCC794-samples, which is shown in Table 5.4. It can be seen that although the simulated enhancements are lower than the measured ones, the ratio between them is similar for both the simulated and measured results. These two examples then indicates that the FDTD-simulations also show quantitatively good results when only patterned structures or unpatterned structures are compared, or when the ratio between the different enhancement are compared. However, this only accounts for samples with a similar structure, and the reason for this will be discussed in the end of this section.

Table 5.4: Comparison of the measured and simulated ratio of the enhancement in light emission. PCC794-1 / PCC794-4 denotes the enhancement in light emission for PCC794-1 divided by the enhancement in light emission for PCC794-4.

Samples	Measured ratio	Simulated ratio
PCC794-1 / PCC794-4	0.86	0.9
PCC794-1 / PCC794-3	1.26	1.25
PCC794-4 / PCC794-4	0.68	0.72

Due to the fact that the FDTD-simulations performed for each individual sample give a lower enhancement than what has been seen experimentally, the problem might be that the full effect of the surface pattern is not seen in the simulations. This could had been the case if the number of periods in the surface pattern was not sufficient, giving finite size effects. The size of the simulations domain was chosen in order to maximise the number of periods without having a simulation that was too time- and memory consuming, and the number of periods was therefore chosen to be 6 and 8 along the two lattice vectors in the 2D hexagonal unit cell. To check the importance of the size of the simulation domain, simulations with a larger domain, doubling the amount of periods in both directions, were performed for PCC793-3 at 140 K. These simulations showed that the enhancement in light emission in this case increased from 31 % to 40 %, indicating that the size of the simulation domain might explain why the simulated enhancement is lower than what is measured experimentally. As the latter simulation was too time-extensive, requiring almost 6 days, compared to 24-30 hours for the smaller domain, all of the simulations could not be performed with the larger domain.

Additionally, the only sample giving an approximately correct enhancement in light emission in the simulations was PCC752-3. This sample was simu-

lated with the same simulation domain, but with a shorter wavelength (2.8 μm instead of 4.6 μm). When normalising the size of the simulation domain against the wavelength, this makes the simulation domain of PCC752-3 much larger, and supports that the error in the simulations of the surface pattern might be due to the size of the simulation domain.

Due to the emitted wavelengths of PCC752-3 being shorter than for the other samples, this sample was simulated with smaller grids. To investigate if this could explain why the simulated enhancement of PCC752-3 was the only one being quantitatively in agreement with the experimental results, PCC794-1 was also simulated with the same grid size. However, this did not change the simulated enhancement of the sample significantly, and can therefore be ruled out as the main reason behind the low simulated enhancement.

Not only the size, but other factors might also affect the simulation results. While the holes in the FDTD-simulations are cylindrical, the holes in the surface pattern of the physical samples showed conical features in the shape in addition to the cylindrical ones, as was shown in section 5.1. Both Trieu et.al [48] and Chavoor et.al. [34] have performed FDTD-simulations comparing cylindrical holes with conical holes, showing that the conical holes in general gives a higher enhancement in light emission. Although the holes processed in this study are not purely conical, the difference in the shape of the holes in the experiment and simulation might also contribute to the different quantitative results obtained.

Table 5.1 also shows that the deepest parts of the holes for some samples are etched all the way through the CdTe-layer, and some tens of nanometers into the active layer. This was not added to the simulations, and might therefore also contribute to a difference in the experimental and simulation results. To test this, a modified simulation of PCC794-4 was performed, where the cylindrical holes were etched 50 nm into the active layer. This 3D FDTD-simulation gave an enhancement of about the same as the regular simulation of PCC794-4, and this source of error can therefore most likely be ruled out.

That the 3D FDTD-simulations performed are able to give good qualitative results, but not as good quantitative results is shown in Figure 5.34. PCC794-1 is used as an illustration, and both simulated and measured results are shown. In section 5.2.4, the experimentally obtained spectrum from the unpatterned area of the sample was used to find what was believed to be the experimental source inside the sample. This was done by dividing the

experimentally obtained spectrum by the simulated wavelength-dependent LEE of the unpatterned area of the sample. The same thing is done here, and gives the source shown earlier in Figure 5.26a. The next thing done was to multiply this source with the simulated wavelength-dependent LEE of the patterned area of the sample to obtain a spectrum from this area. As Figure 5.34 shows, is the shape of the this spectrum very similar to the experimentally obtained spectrum also shown. By multiplying the spectrum obtained with 1.6, it is actually shown that the spectrum is more or less equal to the experimentally obtained one. This simple exercise reveal several features with the FDTD-simulations performed. Firstly, as it was possible to use the simulations to go from the shape of the spectrum from the unpatterned area to the patterned area, the wavelength-dependent LEEs seem to be qualitatively in good agreement with the experimental wavelength-dependent LEEs. Secondly, it also shows that if having the correct source, the simulations will be able to reveal the correct shape of the PL-spectra. And last, as the spectrum obtained for the patterned area has to be multiplied by 1.6, it confirms that the full effect of the surface pattern when it comes to enhancing the light emission is not included.

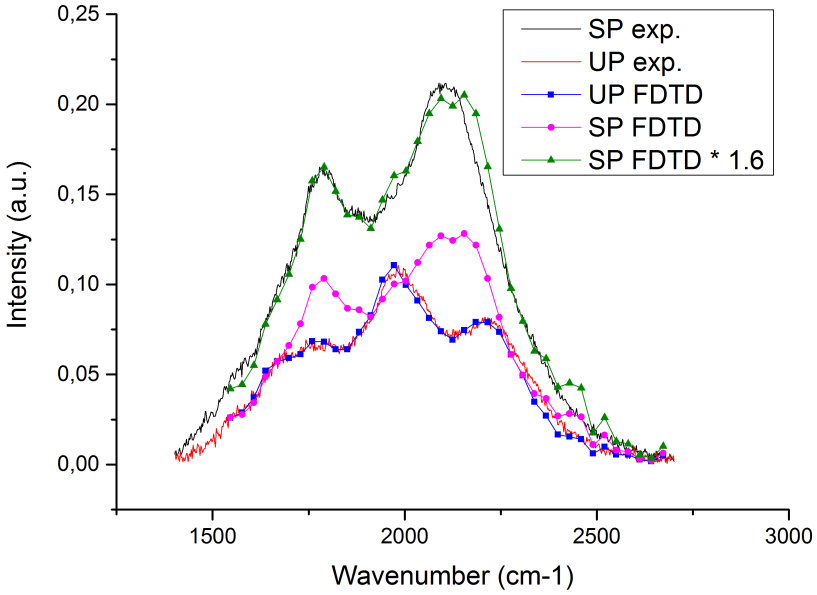

Figure 5.34: The experimentally obtained spectra from the patterned (SP) and unpatterned (UP) area of PCC794-1, together with spectra obtained by combining the experimentally obtained spectra with the wavelength-dependent LEE of the areas of the sample found by FDTD-simulations. "Exp." denoted experimentally obtained, while "FDTD" denoted spectra obtained by using the source of light in PCC794-1 found in section 5.2.4 and the simulated wavelength-dependent LEE of the area.

The exercise performed on PCC794-1 leading to Figure 5.34 was also done for PCC793-4, to verify that it also worked on a sample with a different structure. The source used is then the one shown in Figure 5.26b, and the result can be seen in Figure 5.35. The conclusions drawn from this exercise is the same as for PCC794-1. However, it can be noted that the multiplication factor necessary to align the two spectra from the surface pattern of the sample is only 1.14 for PCC793-4, compared to 1.6 for PCC794-1.

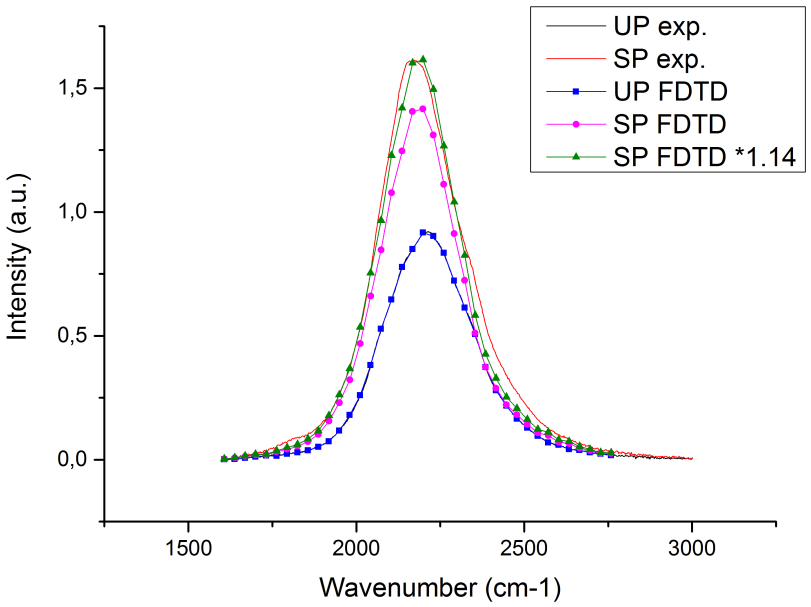

Figure 5.35: The experimentally obtained spectra from the patterned (SP) and unpatterned (UP) area of PCC793-4, together with spectra obtained by combining the experimentally obtained spectra with the wavelength-dependent LEE of the areas of the sample found by FDTD-simulations. "Exp." denoted experimentally obtained, while "FDTD" denoted spectra obtained by using the source of light in PCC793-4 found in section 5.2.4 and the simulated wavelength-dependent LEE of the area.

Figure 5.34 and 5.35 and the exercise performed to obtain them revealed that the method used to find the sources in Figure 5.26 seem to be a valid approach. This then confirms that the spectra from the light source in PCC793 and PCC794 were different. As the FDTD-simulations of these samples were performed with the same Gaussian time-modulated source, this might explain why the simulated results do not seem to be correct both qualitatively and quantitatively when comparing PCC793 and PCC794.

5.5 Reason behind the low PL-intensity

As the results have shown, the PL-intensity is low for many of the samples, causing measurements at 11 K to be impossible for some of them, and several spectra to contain poor statistics, such as in Figure 5.36. Although the design of the sample is made such that the enhancement in light emission still can be measured even though the absolute intensity is low, it is still of importance to know the origin of the low absolute intensity. Both in order to solve the issue itself, and also in order to find out if the problem is due to the sample design used to increase the LEE (such as the DBR), as there would be no use in having a sample design increasing the enhancement, but simultaneously decreasing the absolute intensity.

Because many mechanisms can reduce the PL-intensity, several possible explanations have been investigated. As PCC752-3 gives a decent absolute PL-intensity, the experimental setup can quickly be ruled out. Another possible source is the DBR. As this consist of several layers of different composition, it is a possibility that this has introduced stresses in the material during the MBE growth, giving rise to defects, such as dislocations, in the material. These defects might work as recombination centers for non-radiative recombinations, making the EHPs recombine non-radiatively, and giving a low PL-intensity. To test if the DBRs were mainly responsible for the low PL-intensity, the calibration samples used to calibrate the growth rate in the MBE were used in PL-measurement. These samples were grown within the same time-frame as the samples with low PL-intensity, but without a DBR and only a 17 Å passivation layer. The PL-measurements for these samples also showed a low intensity, which indicates that the DBRs do not seem to be the major problem.

As the problem with low PL-intensity also was present for samples without a DBR, the intrinsic material properties of the active MCT-layer were investigated. The first samples with a DBR studied, which are not included in this study due to the low intensity, show as PCC794 a broad PL spectrum, with more than one significant peak at a lower energy than the calculated band gap energy, indicating the presence of an acceptor level in the material's energy band diagram. For MCT, this acceptor level might be due to Hg-vacancies [49], or structural defects [50]. In both cases, and as mentioned earlier in this section, the vacancies or defects can create recombination centers for non-radiative recombinations, making the EHPs recombine non-radiatively, and giving a low PL-intensity. A possible way to obtain a

high PL-intensity would then be to remove these vacancies or defects, which can be done by annealing [51,52]. In order the remove the Hg-vacancies, the annealing is usually performed in a Hg-atmosphere at a temperature above 200°C in order to fill the vacancies, but due to the passivation layer on top of the samples used in this study, a Hg-atmosphere could not be used, as the Hg-atoms would had becomed incorporated into the passivation layer. In order to keep abrupt interfaces in the DBR, the temperature also had to be kept low. The annealing procedure was therefore performed at 150°C under vacuum conditions. By using the diffusion coefficient found by Jones et.al. [53], an annealing time of 48 hours was used.

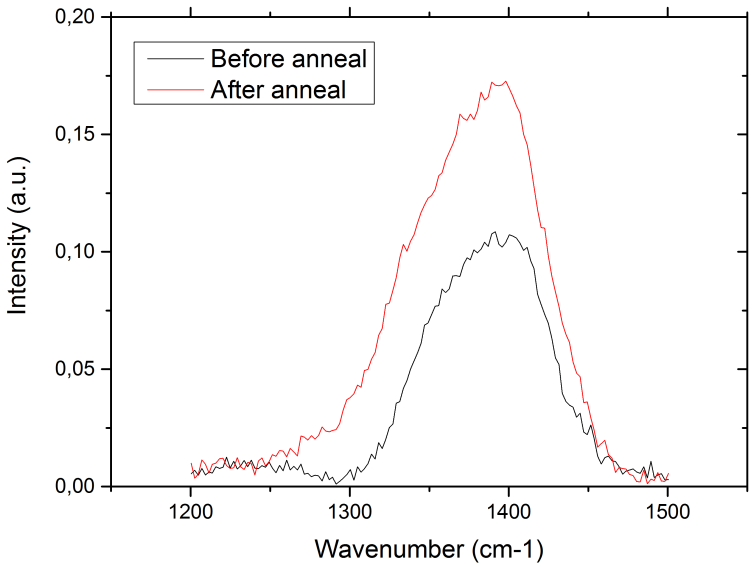

Figure 5.36: Spectra obtained from the calibration sample CMT789 at 11 K before and after anneal.

The effect of this anneal can be seen in Figure 5.36, where the spectrum from the calibration sample CMT789 is seen before and after the anneal. The increase in PL-intensity is small, and the noise due to bad statistics is still apparent in the spectrum.

Another noticeable effect is that the integrated intensity from the PL-spectra is increasing with an increasing temperature for some of the samples studied, illustrated by the fact that they could not be used at 11 K, but had to

be heated to 140 K in order to emit enough PL to perform measurements. Although this was only the case for the samples with a DBR reported in this study, it was also seen for one of the calibration sample for MBE growth without a DBR, and therefore not believed to be due to these layers. This temperature dependence of the PL-intensity is the opposite of what was found by both Zhang et.al, Andersen and Breivik [6, 25, 54], where the PL-intensity decreased with an increasing temperature. The reason for this might be the doping concentration in the samples studied, compared to the ones used in the other studies. As shown by Schacham and Finkman [55], the lifetime of the radiative, Shockley-Read-Hall, and Auger recombinations depend on among others the doping concentration (for instance Hg-vacancies) in MCT. Breivik [25] calculated that the lifetime for radiative recombination will be the shortest, and thereby dominate, only at low temperatures when the doping concentration is around 10^{16}-10^{17} cm^{-3}. For doping concentrations around 10^{14} cm^{-3}, SRH recombinations will dominate at lower temperatures, before radiative recombinations will dominate when the temperature increases. The difference in doping concentrations can therefore explain the opposite temperature effect seen in this study, and might be the reason behind the low PL-intensity. In order to find the doping concentrations, and thereby test this explanation, Hall measurements were performed on PCC793. These measurements showed a net concentration of positive minority charge carriers (holes most likely due to Hg-vacancies) of about 10^{15} cm^{-1}. This supports the explanation for the low PL-intensity suggested here, but as the lifetime calculations by Breivik [25] was for somehow different parameters of the MCT-layer, new calculations for the parameters of the MCT-layer of the samples in this study should be performed.

The reason behind the low PL-intensity has not been fully revealed, but the investigations indicate that it is due to an intrinsic material property in the MCT layer. It is believed that the DBRs are not the main reason for the problem, as both samples with and without a DBR in this study have low PL-intensity.

Chapter 6

Conclusions and further work

6.1 Conclusions

MCT thin film samples have been grown by MBE, and a triangular pattern of holes has been etched into the passivation layer by means of photolithography.

PL-measurements and simulations by both transfer matrices and FDTD have been used to investigate the enhancement in light emission from the MCT samples due to their surface pattern, which have been measured to be between 31 % and 163 %. Both samples with and without a DBR have been measured, and the results were in both cases a higher enhancement than the 26-35 % obtained in a previous study at FFI [2].

The effect of the grating period has been investigated, where both the experimental results and the simulations show that a normalised grating period around 1 $\frac{a}{\lambda}$ is optimal. Close to this value, the enhancement in light emission was stable, and the optimal normalised grating period seemed to be depending on the individual sample. For normalised grating periods larger than about 1.4, the enhancement in light emission was decreasing for increasing grating periods.

Varying the thickness of the passivation layer also had an effect on the enhancement in light emission, as the experimental setup demands that the

measured intensity from the area of the sample with a surface pattern is compared to an area of the sample without. As the intensity from the area without a pattern depends on the thickness of the passivation layer, this will affect the measured enhancement. In addition, it was also shown that the depth of the holes was of importance, and for a wavelength around 4.6 μm, the holes should be at least 600 nm deep, and etched all the way to the bottom of the passivation layer.

Due to a low collection angle of the collection mirrors, two different sample holders were used, to see how the enhancement changed when the light with different exit angles from the surface was detected. The measurements performed showed that the different sample holders gave similar results.

How the enhancement depends on the fill factor of the surface pattern was also partly tested. Here, problems with controlling the size of the holes lead to limited testing, but it was shown that the enhancement in light emission was significantly decreasing when the holes started to overlap.

From all of the measurements and simulations, the total effect of the DBR has been discussed. Although the highest enhancement was measured for a sample without a DBR, this measurement was performed at 11 K where the absolute intensity from the samples with a DBR was too low to give good statistics. At a temperature where both the samples with and without a DBR could be measured, the samples with a DBR showed the highest enhancement. This, together with simulations showing an increase in absolute intensity when a DBR is present, shows that the DBR has a positive effect. However, on the downside, the samples with a DBR emitted light with a broad range of wavelengths. If further investigations also show that the low PL-intensity at 11 K for samples with a DBR is due to the DBR itself, a sample without is recommended.

Although the absolute intensity of the thin-film samples with a DBR decreased with temperature below 140 K, giving a very weak signal at 11 K, the MQW-sample had its highest intensity at this temperature. The sample also showed an absolute intensity at least an order of magnitude higher than the maximum absolute intensity from the other samples. To maximize the light output, it is therefore recommended to use a MQW-sample with a surface pattern having $\frac{a}{\lambda} \approx 1$, holes etched all the way through a passivation layer of at least 600 nm, and probably with a DBR. The limited investiga-

tions of the fill factor indicates that this should be at least 0.38.

The FDTD-simulations seem to predict very well the spectra of the emitted light and the difference in enhancement due to varying one sample characteristic at a time, but they do not always predict the correct value of the enhancement. However, it is plausible that using a larger simulation domain will improve the absolute values of the simulated enhancements.

Finally, it should also be mentioned that a decrease in enhancement for increasing temperatures was observed. The cause of this was however not completely understood, as neither the change in refractive indices, nor the change in emitted wavelengths could fully explain the measured results.

6.2 Further work

The samples measured in this study showed a large improvement in enhanement in light emission compared to the earlier study at FFI. However, it is still room for even further improvements and new investigations, as some of the results still have not got a full explanation, and the control of the parameters during the processing of the samples has been proved challenging.

In order to use the structures in an LED, they have to increase the absolute intensity compared to what was shown in this study. The reason behind the low intensity should therefore be investigated further, where it was suggested to perform lifetime calculations for the different recombination mechanisms with the sample parameters found by PL and the Hall measurement. When this issue has been solved, it will also be possible to compare all samples at the temperature that is thought as the operating temperature of the LEDs.

More work should also be put into controlling the processing of the samples. With the equipment available at the Epitek-laboratory at FFI today, the surface pattern and especially the size of the holes were in the borderline of what could be processed in a controlled manner with the given equipment and techniques. This made it hard to control the fill factor of the surface pattern and the depth of the holes. In order to investigate the fill factor of the surface pattern, and its effect on the enhancement in light emission, a better control of the processing parameters is necessary.

With the given processing technique, we were not able to process a surface pattern with a grating period smaller than 4.5 μm. 2D FDTD-simulations in my project assignment [1] showed that even smaller normalised grating periods than what was studied could give a larger enhancement in light emission. Processing techniques making it possible to process a smaller pattern should therefore be explored. Alternatively, a smaller x-value of the active layer can also be used, as the emitted wavelengths then are longer.

In addition, the effect causing the enhancement to decrease with increasing temperature was never fully understood. More investigations into this might reveal factors important in order to maximize the enhancement in light emission, and should therefore also be performed.

When being able to do all this, new samples with and without a DBR with the optimised parameters should be grown and processed, and then compared at the thought operating temperature of the LED, to give a clearer answer on the effect of the DBR than what was found from this study.

The absolute intensity of the MQW sample was significantly higher than from the thin film samples. This is in agreement with what has been found in earlier studies at FFI [2], and new samples should therefore be MQW samples.

Eventually, complete LEDs with an optimised surface pattern should be fabricated.

Appendix A

Additional sample information

A.1 PCC752-3

A.1.1 AFM-images

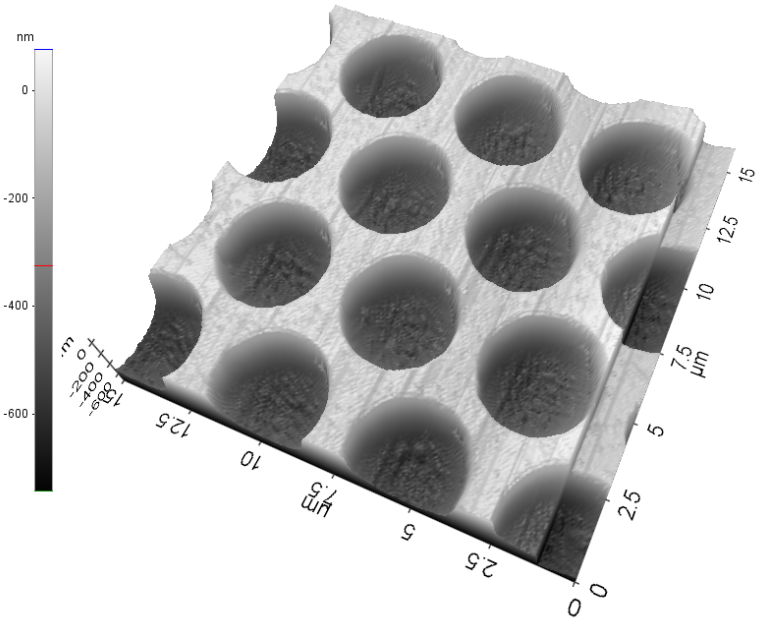

Figure A.1: AFM-image showing a representative area of the surface pattern of PCC752-3..

A.1.2 Characterisation of the PL-spectrum

Figure A.2 shows the PL-peaks origin from the patterned area of the sample. Two peaks can be seen, separated by about 150 cm^{-1}. As the emitted light from the absorption layer is blocked by a filter, both of these two peaks are from the MQWs. However, earlier studies at FFI with QWs have only revealed one peak when performing PL-measurements [24]. The reason why two peaks are seen instead of one is unclear, but it is believed that it is due to two different radiative recombinations taking place, where one includes electrons and light holes, while the other process contains electrons and heavy holes [56]. The calculated separation between the two peaks are then 200-250 cm^{-1}, however, it can not be excluded from these calculations that the two peaks origin from recombinations with light and heavy holes, as the square well model, which is used for the calculations, is only an approximation.

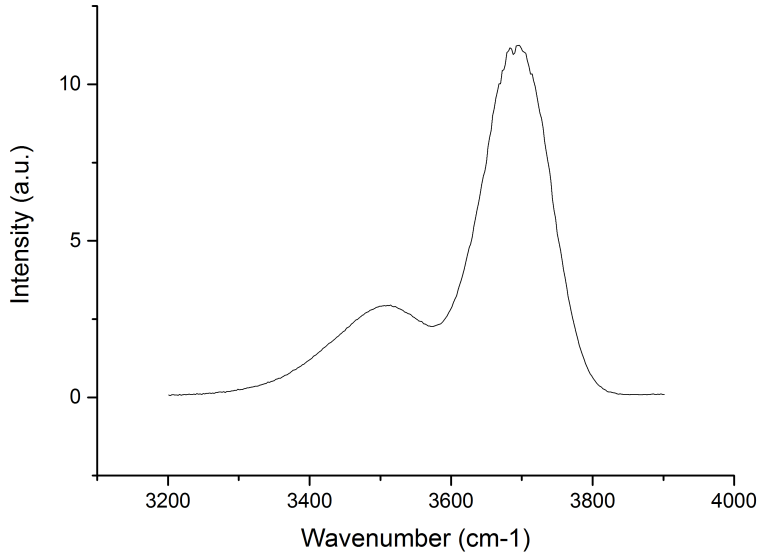

Figure A.2: Spectrum obtained from the patterned area of PCC752-3 at 11 K.

A.1.3 Absolute value of the intensity

It should also be noticed that the absolute measured intensity from this sample is of an order of magnitude larger than what was seen for the other sam-

ples. Although the absolute measured intensity has somehow arbitrary units, a measurement orders of magnitude larger than the other measurements still gives a good indication that the absolute intensity is higher. This is most likely due to the fact the the light origin from the MQW, and not a thin film, as the Auger recombinations has a lifetime about a factor 100 larger in MQWs than in thin films [57]. This gives less non-radiative recombinations, and thereby increases the PL-intensity.

A.2 PCC793-3

A.2.1 Images

Due to complications during the processing of the surface pattern, the patterned area of the sample is small. This can be seen in Figure A.3. It is also evident that the quality of the surface pattern is increasing, meaning deeper and more uniform holes, when moving towards the central parts of the sample. This can be seen in Figure A.4 and A.5, where the holes in the areas away from the central region of the sample have a small "island" inside the hole which has not been etched, and do not have a completely circular symmetry. For the region close to the center of the sample, these "islands" are removed, and the holes are deeper, however, the holes still do not retain good circular symmetry and the depth is also varying depending on the distance from the center of the hole, giving more conical-like holes.

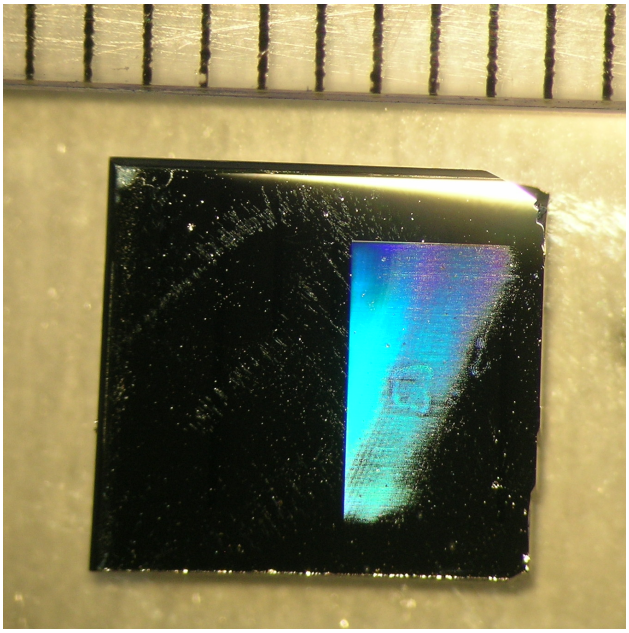

Figure A.3: Image of PCC793-3, showing the relatively area of the surface pattern. The black areas are unprocessed, while the coloured one is processed. A ruler is shown in the top edge of the picture, showing a millimeter scale.

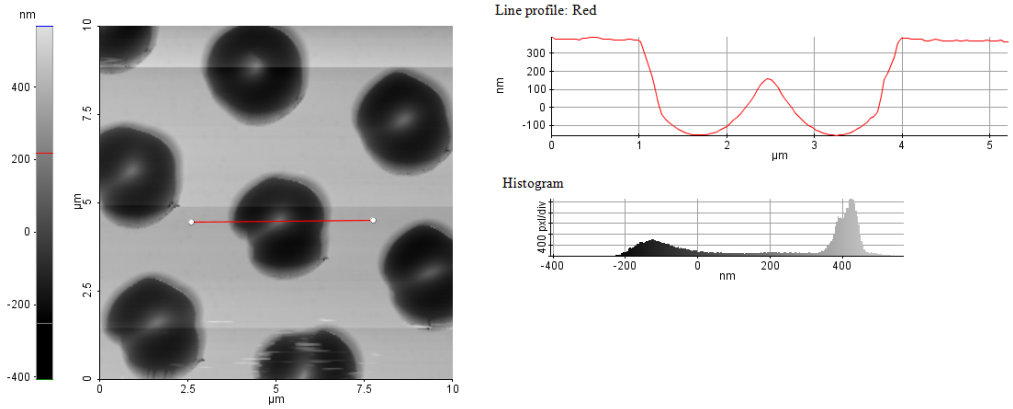

Figure A.4: AFM-image showing a representative area of the surface pattern away from the central region of PCC793-3, with the height profile of a hole included. The histogram indicates the number of pixels in the image with a given height.

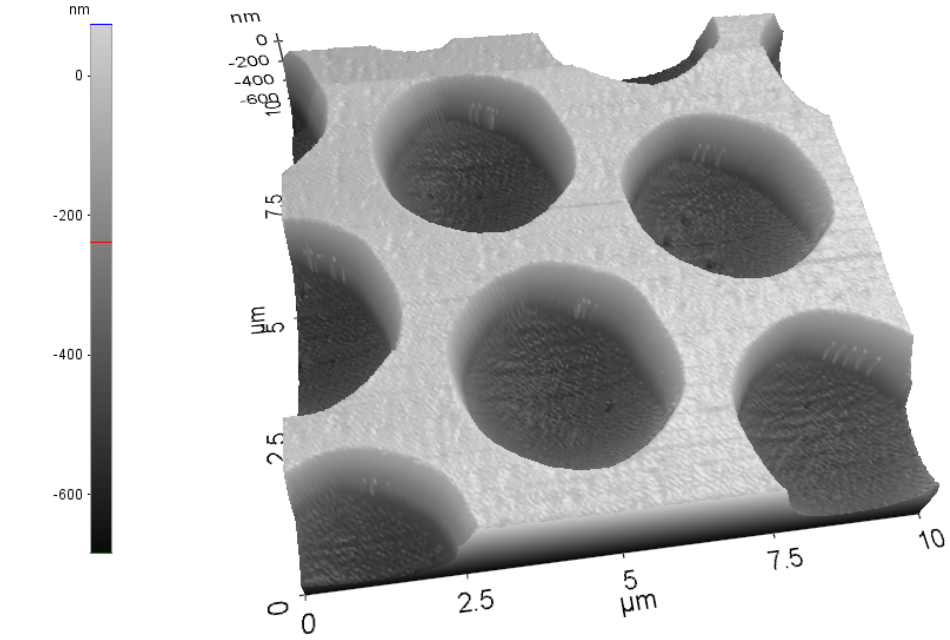

(a)

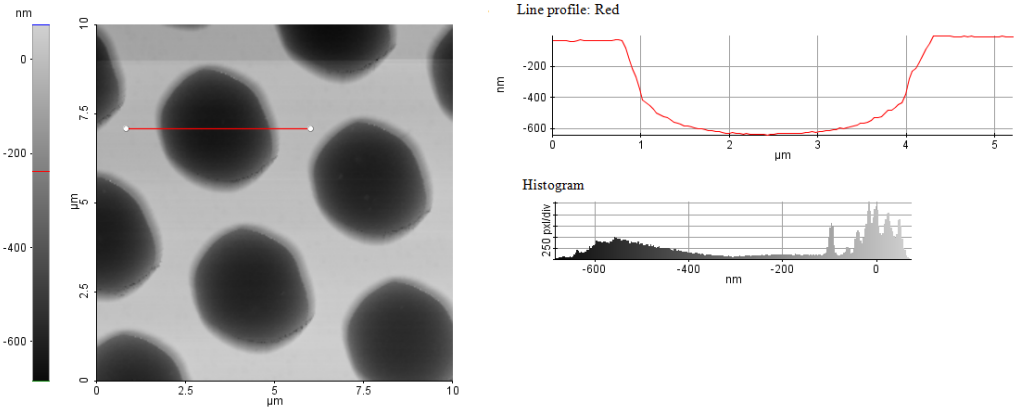

(b)

Figure A.5: (a) AFM-image showing a representative area of the surface pattern from the central region of PCC793-3. (b) The same area seen from above, with the height profile of the line indicated. The histogram indicates the number of pixels in the image with a given height.

A.2.2 PL-measurement at 11 K and 140 K

The PL-measurements for PCC793-3 were done with sample holder A, and the spectra of the PL-measurement at both 11 K and 140 K are shown in Figure A.6. Although the enhancement in light emission differs from the one of PCC793-4, the features of the spectra are still the same as the ones presented in Figure 5.7, where the spectra of PCC793-4 were shown. For a discussion regarding these spectra, it is referred to section 5.1.2.

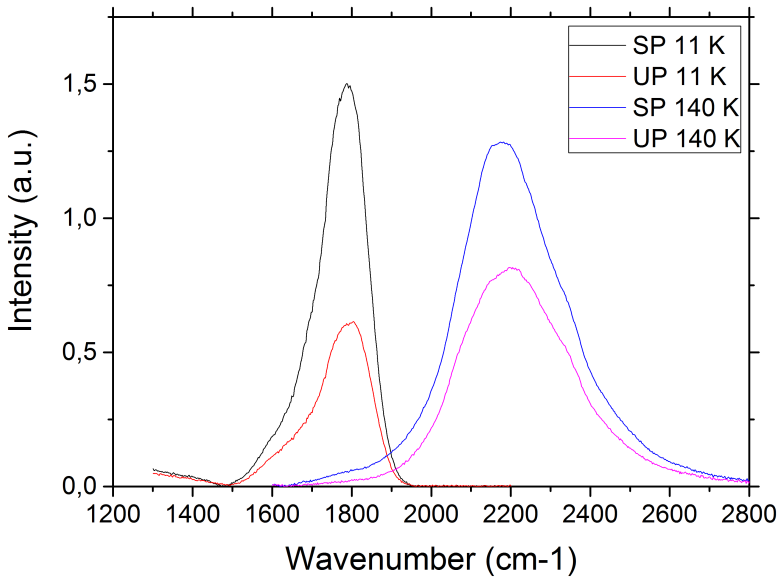

Figure A.6: Spectra at from the patterned (SP) and unpatterned area (UP) of PCC793-3 at 11 K and 140 K.

A.3 PCC793-4

A.3.1 PL-measurement at 220 K

The PL-measurements performed at 11 K and 140 K are described in section 5.1.2. The shape of the spectra at 220 K can be seen in Figure A.7, and is somehow different from different from the spectra at lower temperature. This can be explained by the fact that at 220 K, the thermal energy is higher, making the spectrum look more similar to a PL spectrum from a

room temperatured semiconductor [6], where there is a tail towards higher wavenumbers.

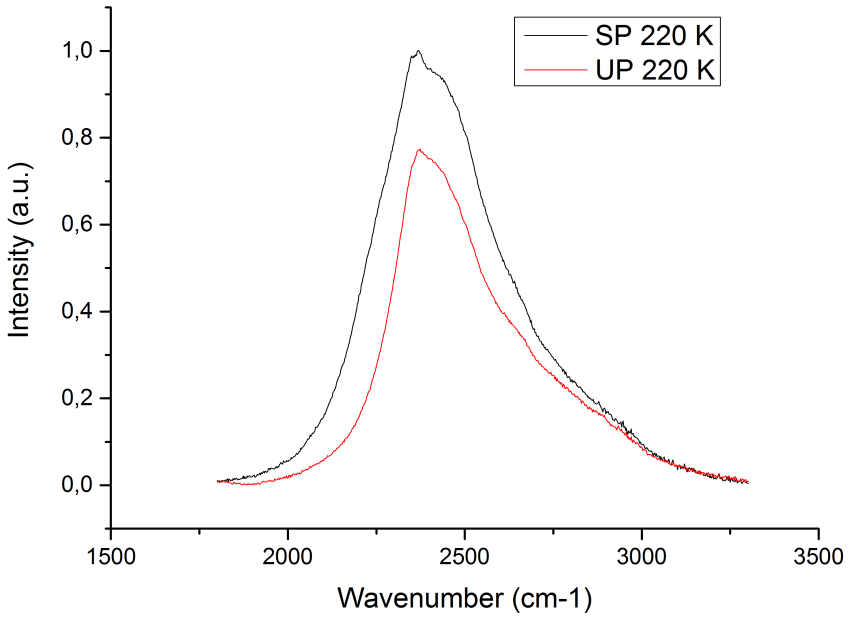

Figure A.7: Spectra at from the patterned (SP) and unpatterned area (UP) of PCC793-4 at 220 K with sample holder A.

The integrated intensity at 220 K is shown in Figure A.8. As for the measurements at lower temperatures, the integrated intensity is increasing when moving across the surface pattern towards the center of the sample, due to the variation in the quality of the pattern. The enhancement is calculated from the two plateaus to be 42 %.

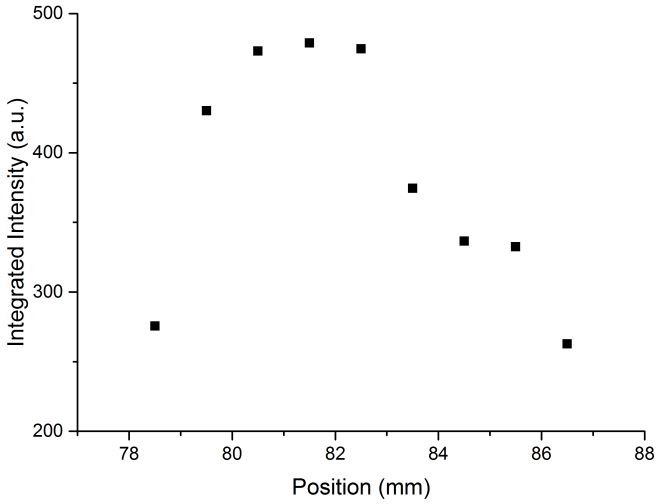

Figure A.8: Integrated intensity at different positions of the PCC793-4 measured with sample holder A at 220 K.

A.4 PCC794-1

A.4.1 AFM-image

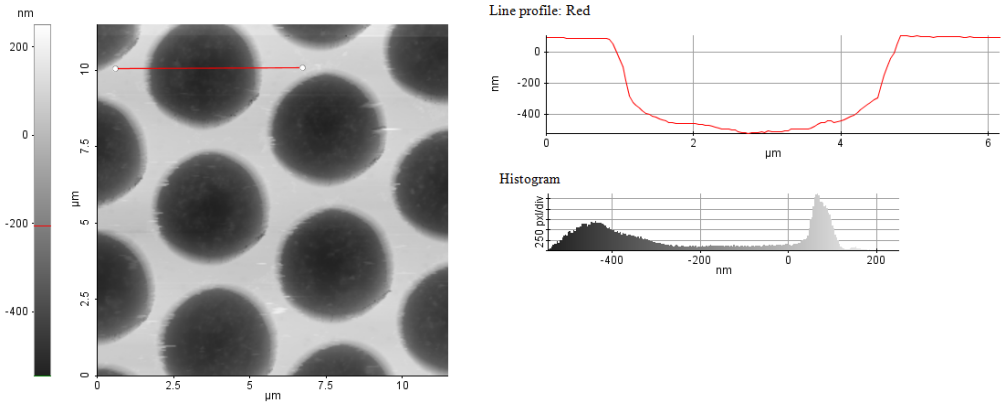

Figure A.9: AFM-image showing a representative area of the surface pattern of PCC794-1, with the height profile of a hole included. The histogram indicates the number of pixels in the image with a given height.

A.4.2 PL-measurement at 220 K

The spectra and integrated intensity from the PL-measurements at 140 K were described in section 5.1.3. At 220 K, the obtained spectra are shown in Figure A.10. These spectra differ in the shape from the ones at 140 K. The reason for this is most likely due to the wavelength-dependent LEE of the unpatterned area, as Figure shown by Figure 5.33, and that the intensity from the low-energy peak decreases with increasing temperature, which would be in agreement with the findings of Andersen [6].

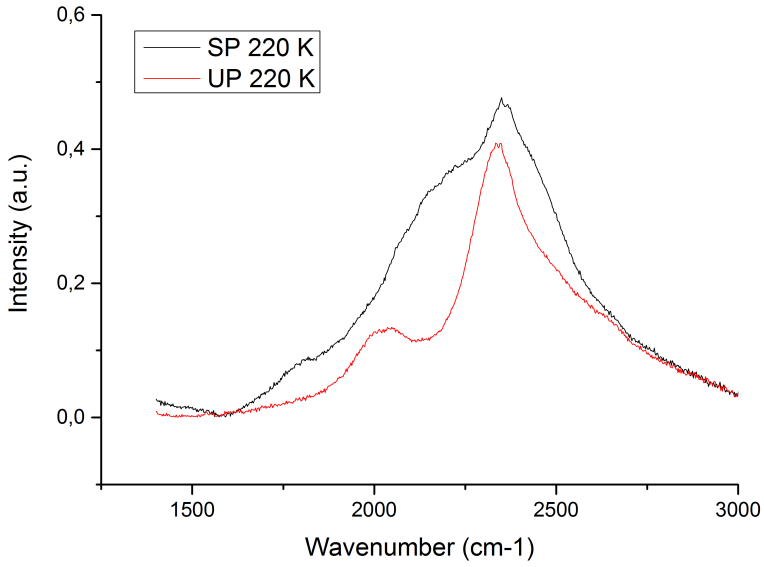

Figure A.10: Spectra obtained from the patterned (SP) and unpatterned (UP) area of PCC794-1 at 220 K with sample holder A.

The integrated intensity at 220 K is shown in Figure A.11, and the enhancement is calculated from the two plateaus to be 42 %.

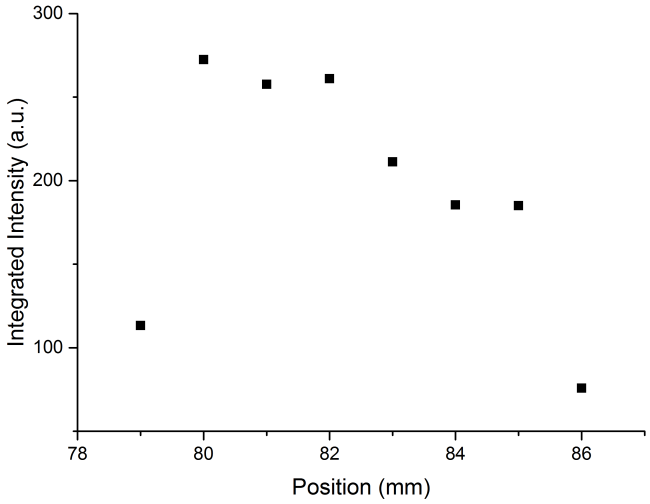

Figure A.11: Integrated intensity at different positions of the PCC794-1 measured with sample holder A at 220 K.

A.5 PCC794-3

A.5.1 AFM-images

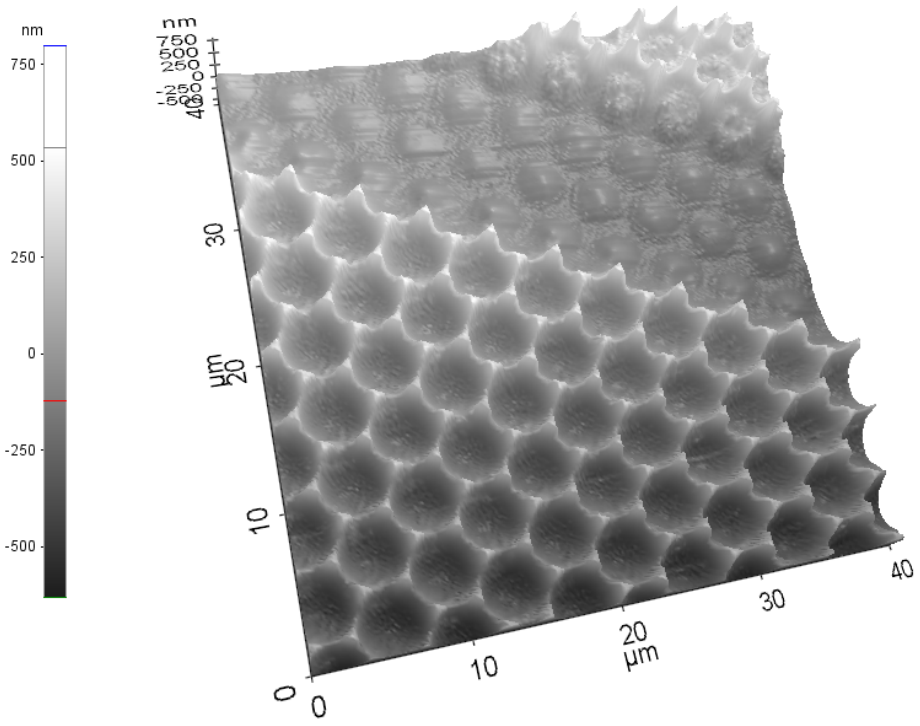

Figure A.12: AFM-image of PCC794-3 showing a stripe defect in the surface pattern present from the processing. Several of these defects were present across the whole pattern.

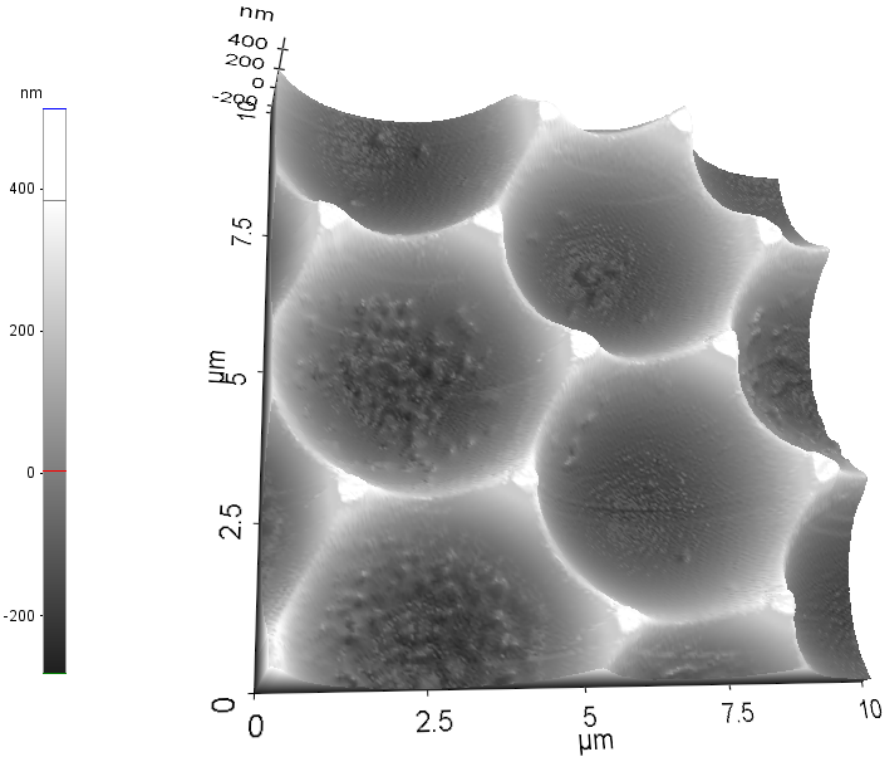

Figure A.13: AFM-image of PCC794-3 showing an area of the surface pattern of PCC794-3.

A.5.2 PL-measurement at 220 K

The spectra and integrated intensity from the PL-measurements at 140 K were described in respectively section 5.2.5 and 5.1.3. At 220 K, the obtained spectra are shown in Figure A.14. These spectra differ in the shape from the ones at 140 K. The reason for this is as described for PCC794-3 in the previous section.

The integrated intensity at 220 K is shown in Figure A.15, and the enhancement is calculated from the two plateaus to be 31 %.

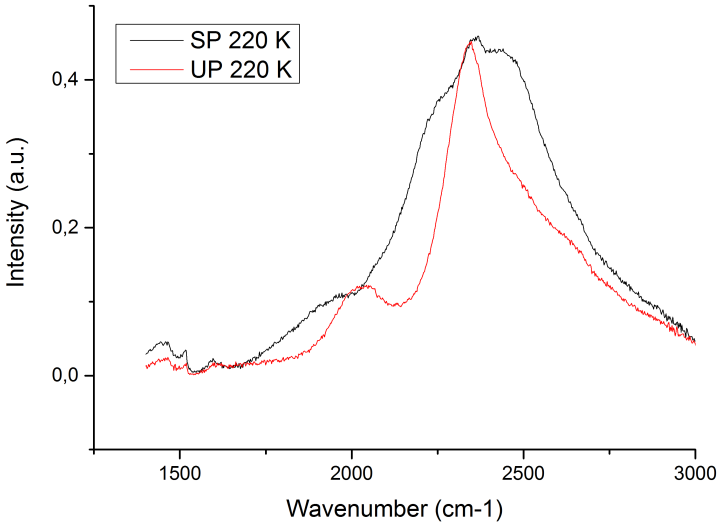

Figure A.14: Spectra obtained from the patterned (SP) and unpatterned (UP) area of PCC794-3 at 220 K with sample holder A.

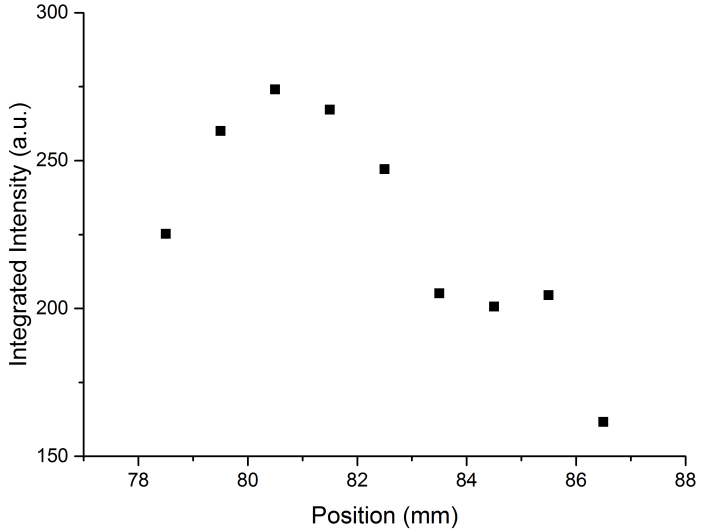

Figure A.15: Integrated intensity at different positions of the PCC794-3 measured with sample holder A at 220 K.

A.6 PCC794-4

A.6.1 AFM-image

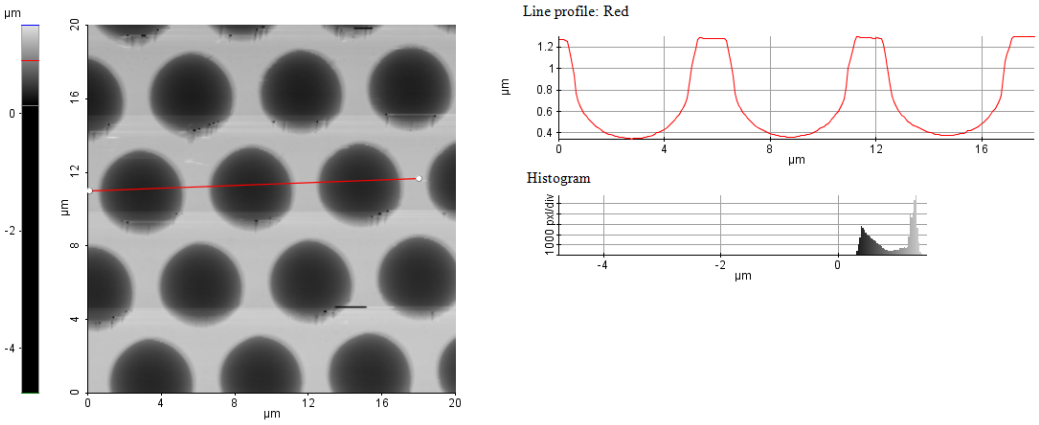

Figure A.16: AFM-image showing a representative area of the surface pattern of PCC794-4, with the height profile of a hole included. The horisontal stripes are noise in the image acquisition. The histogram indicates the number of pixels in the image with a given height.

A.6.2 PL-measurement at 140 K and 220 K

The spectra obtained from PCC794-4 are as Figure A.17 show, similar to the ones obtained from PCC794-1 and PCC794-3 when it comes to both shape and absolute intensity, and the discussion about this is therefore referred to section 5.1.3 and A.4.

The integrated intensity from the measurement at 140 K is shown and discussed in section 5.1.3. The integrated intensity at 220 K, on the other hand, is shown in Figure A.18, and the enhancement is calculated from the two plateaus to be 42 %.

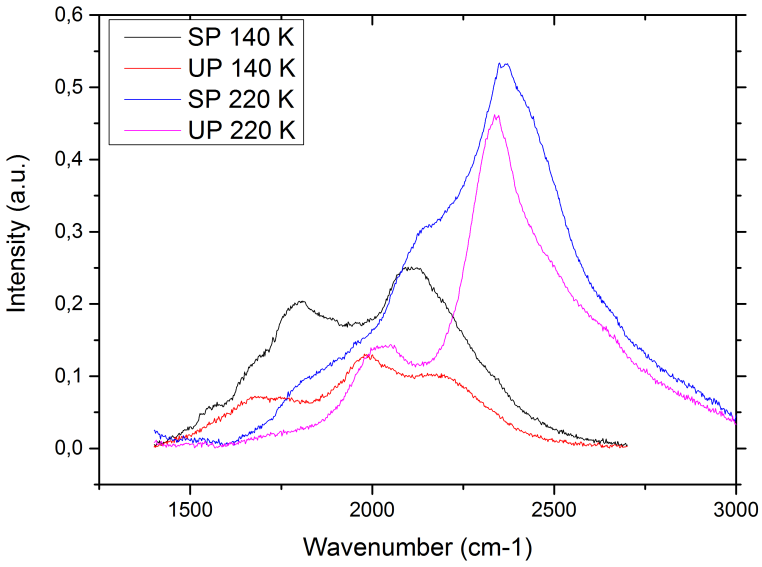

Figure A.17: Spectra obtained from PL by measuring at the patterned (SP) and unpatterned (UP) area of the sample at 140 K and 220 K with sample holder A.

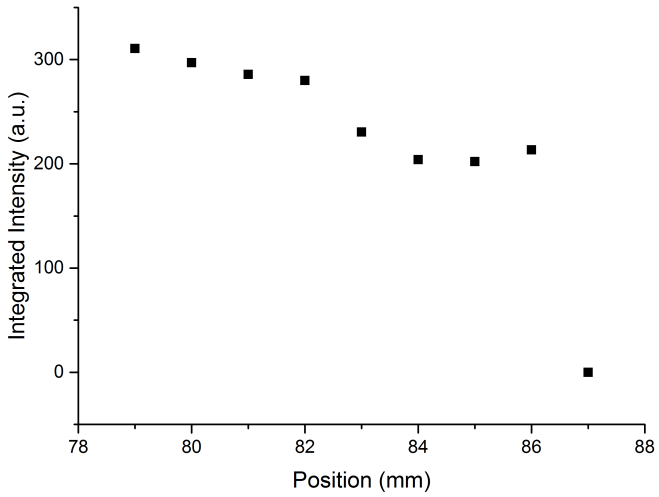

Figure A.18: Integrated intensity at different positions of the PCC794-4 measured with sample holder A at 220 K.

Bibliography

[1] Espen T. Haugan. Enhanced light emission from HgCdTe thin films with a surface pattern. Project assignment, Norwegian University of Science and Technology, 2014.

[2] Celin R. Tonheim, Aasmund S. Sudbø, Espen Selvig, and Randi Haakenaasen. Enhancement in light emission from Hg-Cd-Te due to surface patterning. *IEEE Photon. Technol. Lett.*, 23(1):36–38, 2011.

[3] R.M. Biefeld, A.A. Allermann, and S.R.Kurtz. Recent advances in mid-infrared (3-6 μm) emitters. *Mater. Sci. Eng., B*, 51:1–8, 1998.

[4] N.C. Das, K. Olver, and F. Towner. High emissive power MWIR LED array. *Solid-State Electron.*, 49:1422–1427, 2005.

[5] A. Godard. Infrared (2-12 μm) solid-state laser sources: a review. *Comptes Rendus Physique*, 8:1100–1128, 2007.

[6] Jonathan Borenstein Andersen. Photoluminescence characterization of molecular beam epitaxy grown $Cd_xHg_{1-x}Te$ thin films doped with Ag, In and Hg-vacancies. Diploma thesis, Norwegian University of Science and Technology, 2008.

[7] W. N. Carr and G. E. Pittmann. One-watt GaAs p-n junction infrared source. *Appl. Phys. Lett.*, 3:173–175, 1963.

[8] I. Schnitzer, E. Yablonovitch, C. Caneau, T. J. Gmitter, and A. Scherer. 30-percent external quantum efficiency from surface textured, thin-film light-emitting diodes. *Appl. Phys. Lett.*, 63:2174–2176, 1993.

[9] T. Fujii et. al. Increase in extraction efficiency of GaN-based light-emitting diode with a two-dimensional surface grating photonic crystal. *Appl. Phys. Lett.*, 84:855–857, 2004.

[10] Hiroyuki Ichikawa and Toshihiko Baba. Efficiency enhancement in a light-emitting diode with a two-dimensional surface grating photonic crystal. *Appl. Phys. Lett.*, 84(4):457–459, 2004.

[11] M. Boroditsky, R. Vrijen, T.F. Krauss, R. Coccioli, R. Bhat, and E. Yablonovitch. Spontaneous emission extraction and purchell enhancement from thin-film 2-D photonic crystals. *J. Lightwave Technol.*, 17(11):2096–2112, 1999.

[12] T. Kim, P.O. Leisher, A.J. Danner, R. Wirth, K. Streubel, and K. D. Choquette. Photonic crystal structure effect on the enhancement in the external quantum efficiency of a red LED. *IEEE Photon. Technol. Lett.*, 18(17):1876–1878, 2006.

[13] K.-J. Byeon et. al. Enhancement of the photon extraction of green and blue LEDs by patterning the indium tin oxide top layer. *Semicond. Sci. Technol.*, 24:105004, 2009.

[14] Dusan Pudis, Lubos Suslik, Jaroslava Skriniarova, Jaroslav Kovac, Jaroslav Kovac Jr., and Ivana Kubicova et.al. Effect of 2D photonic structures patterned in the LED surface on emission properties. *Appl. Surf. Sci.*, 269:161–165, 2013.

[15] John D. Joannopoulos, Steven G. Johnson, Joshua N. Winn, and Robert D. Meade. *Photonic Crystals; Molding the Flow of Light*. Princeton University Press, Princeton, New Jersey, 2008.

[16] Aasmund S. Sudbø. Periodic multilayer film, 2013. http://persons.unik.no/aas/unik4380/problems/multilayerfilm.pdf.

[17] Steven G. Johnson, Shanhui Fan, Pierre R. Villeneuve, J. D. Joannopoulos, and L.A. Kolodziejski. Guided modes in photonic crystal slabs. *Phys. Rev. B*, 60(8):5751–5758, 1999.

[18] Shanhui Fan, Pierre R. Villeneuve, J. D. Joannopoulos, and E. F. Schubert. High extraction efficiency of spontaneous emission from slabs of photonic crystals. *Phys. Rev. Lett.*, 78(17):3294–3297, 1997.

[19] A.M. Adawi, R. Kullock, J.L. Turner, C. Vasilev, D.G Lidzey, and A. Tahraoui et.al. Improving the light extraction efficiency of polymer light emitting diodes using two-dimensional photonic crystals. *Org. Electron.*, 7:222–228, 2006.

[20] Roel Baets. Chapter thin films. Technical report, Ghent University, 10 2010.

[21] R. Paschotta. Bragg mirrors. In *Encyclopedia of Laser Physics and Technology*. Wiley-VCH, 1 edition, 10 2008.

[22] J.C. Brice. *Properties of Mercury Cadmium Telluride*, pages 103–107. Inspec, New York, 1987.

[23] F. Yue, J. Shao, X. Lu, W. Huang, and H. Chu. Anomalous temperature dependence of absorption edge in narrow-gap HgCdTe semiconductors. *Appl. Phys. Lett.*, 89, 2006.

[24] Celin Russøy Tonheim. Growth and characterization of $Cd_xHg_{1-x}Te$ multiple quantum wells. Diploma thesis, Norwegian University of Science and Technology, 2006.

[25] Magnus Breivik. Fourier transform photoluminescence spectroscopy of $Cd_xHg_{1-x}Te$. Diploma thesis, Norwegian University of Science and Technology, 2007.

[26] E. Selvig, S. Hadzialic, R. Haakenaasen, T. Skauli, H. Steen, A. van Rheenen, L. Trosdahl-Iversen, G. Myrvågnes, and B.O. Fimland. Growth of $Cd_xHg_{1-x}Te$ nanowires. In *Poster presented at Nanomat 2004 conference, Oslo*, 2004.

[27] E. Selvig, C.R. Tonheim, K.O. Kongshaug, H. Hemmen, T. Lorentzen, and R. Haakenaasen. Defects in CdHgTe grown by molecular beam epitaxy on (211)B-oriented CdZnTe substrates. *J. Vac. Sci. Technol., B*, 26:525–533, 2008.

[28] Michael Quirk and Julian Serda. *Semiconductor Manufacturing Technology*. Prentice Hall, 2000.

[29] S. Perkowitz. *Optical Characterization of Semiconductors*. Academic Press Ltd., 1993.

[30] D.B. Tanner and R.P. McCall. Source of a problem with Fourier transform spectroscopy. *Appl. Opt.*, 23(14), 1984.

[31] L.S. Rothman et.al. The HITRAN 2008 molecular spectroscopic database. *J. Quant. Spectrosc. Radiat. Transfer*, 100:533–572, 2009.

[32] http://www.sigmaplot.com/products/peakfit/peakfit.php.

[33] Kane Yee. Numerical solution of initial boundary value problems involving Maxwell's equations in isotropic media. *IEEE Trans. Antennas Propag*, 14(3):302–307, 1966.

[34] Greg Chavoor, Xiaomin Jin, Ashton Ellaboudy, Xing-Xing Fu, Xiang-Ning Kang, and Bei Zhang et.al. Light extraction improvement of GaN LED using nano-scale top transmission gratings. In Matthew H. Kane, Christian Wetzel, and Jian-Jang Huang, editors, *Eleventh International Conference on Solid State Lighting*, 2011.

[35] Jui-Wen Pan, Pei-Jung Tsai, Kao-Der Chang, and Yung-Yuan Chang. Light extraction efficiency analysis of GaN-based light-emitting dioded

with nanopatterned sapphire substrates. *Appl. Opt.*, 52(7):1358–1367, 2013.

[36] http://ab-initio.mit.edu/wiki/index.php/Meep.

[37] http://optiwave.com/category/optifdtd-manuals/.

[38] Hao Cui and Si-Hyun Park. Numerical simulations of light-extraction efficiencies of light-emitting diodes on micro and nanopatterned sapphire substrates. *Micro. Nano. Lett.*, 9:841–844, 2014.

[39] Q. Zhang, K. H. Li, and H.W. Choi. InGaN lightemitting diodes with indiumtinoxide submicron lenses patterned by nanosphere lithography. *Appl. Phys. Lett.*, 100, 2012.

[40] Peifen Zhu, Guangyu Liu, Jing Zhang, and Nelson Tansui. FDTD analysis on extraction efficiency of GaN light-emitting diodes with microsphere arrays. *J. Disp. Technol.*, 9(5):317–322, 2013.

[41] ByeongChan Park, Heeso Noh, Young Moon Yu, and Jae-Won Jang. Finite-difference time-domain analysis on light extraction in a GaN light-emitting diode by empirically capable dielectric nano-features. *J. Appl. Phys.*, 116, 2014.

[42] Edward D. Palik. *Handbook of Optical Constants of Solids.* Academic Press, San Diego, 1998.

[43] P. Hldek, J. Bok, J.Franc, and R.Grill. Refractive index of CdTe: Spectral and temperature dependence. *J. Appl. Phys.*, 90(3):1672–1674, 2001.

[44] Manuel A. Quijada and Ross Henry. Temperature evolution of excitonic absorptions in $Cd_{1-x}Zn_xTe$ materials. Nasa Goddard Space Flight Center, 2007. http://ntrs.nasa.gov/archive/nasa/casi.ntrs.nasa.gov/20070036805.pdf.

[45] Ho-Seok Ee, Sun-Kyung Kim, Soon-Hong Kwon, and Hong-Gyu Park. Design of polarization-selective light emitters using one-dimensional metal grating mirror. *Opt. Express*, 19(2), 2011.

[46] www.mathworks.com/products/matlab/.

[47] K. Liu, J.H. Chu, and D.Y. Tang. Composition and temperature dependence of the refractive index in $Hg_{1-x}Cd_xTe$. *J. Appl. Phys.*, 75:4176–4179, 1994.

[48] Simeon Trieu, Xiaomin Jin, Bei Zhang, Tao Dai, Kui Bao, and Xiang-Ning Kang et.al. Light extraction improvement of GaN-based light emitting diodes using patterned undoped GaN bottom reflection gratings. In

Hadis Morkoc, Cole W. Litton, and Jen-Inn Chyi, editors, *Gallium Nitride Materials and Devices IV*, 2009.

[49] F. Gemain, I.C. Robin, S. Brochen, M. De Vita, O. Gravrand, and A. Lusson. Optical and electrical studies of the double acceptor levels of the mercury vacancies in HgCdTe. *J. Electron. Mater.*, 41(10), 2012.

[50] K.D. Mynbaev, A.V. Shilyaev, N.L. Bazhenov, A.I. Izhnin, I.I. Izhnin, A.V. Voitsekhovskii, N.N. Mikhailov, V.S. Varavin, and S.A. Dvoretsky. Light emission from CdHgTe-based nanostructures. *Materials Physics and Mechanics*, 21:112–118, 2014.

[51] S.R. Kurtz, J. Bajaj, D.D. Edwall, and S.J.C. Irvine. Infrared photoluminescence characterization of long-wavelength HgCdTe detector materials. *Semicond. Sci. Technol.*, 8:941–945, 1993.

[52] I.I. Izhnin, A.I. Izhnin, K.D. Mynbaev, N.L. Bazhenov, A.V. Shilyaev, N.N. Mikhailov, V.S. Varavin, S.A. Dvoretsky, O.J. Fitsych, and A.V. Voitsekhovsky. Photoluminescence of HgCdTe nanostructures grown by molecular beam epitaxy on GaAs. *Opto-Electron. Rev.*, 21(4):390–394, 2013.

[53] C.L. Jones, M.J.T. Quelch, P. Capper, and J.J. Gosney. Effects of annealing on the electrical properties of Cd x Hg 1-x Te. *J. Appl. Phys.*, 53:980–992, 1982.

[54] Xiaohua Zhang, Jun Shao, Lu Chen, Xiang Lü, Shaoling Guo, Li He, and Junhao Cho. Infrared photoluminescence of arsenic-doped HgCdTe in a wide temperature range up to 290 k. *J. Appl. Phys.*, 110, 2011.

[55] S.E. Schacham and E. Finkman. Recombination mechanisms in p-type HgCdTe. *J. Appl. Phys.*, 57:2001–2009, 1985.

[56] Celin R. Tonheim. Fotonisk krystallprøver grodd i perioden 27.09.07-11.09.08. Unpublished notes regarding samples studied at FFI, including PCC752-3.

[57] Y. Jiang, M.C. Teich, and W.I. Wang. Carrier lifetimes and threshold currents in HgCdTe double heterostructure and multiquantum-well lasers. *J. Appl. Phys.*, 69:6869–6875, 1991.